

H I Galaxy Signatures in the SARA0 MeerKAT Galactic Plane Survey – III. Unveiling the obscured part of the Vela Supercluster

Sambatriniaina H. A. Rajohnson¹, ^{*} Renée C. Kraan-Korteweg¹, Hao Chen^{1,2}, Bradley S. Frank^{3,4,5,1}, Nadia Steyn^{1,6}, Sushma Kurapati¹, D. J. Pisano¹, Lister Staveley-Smith⁶, Paolo Serra⁷, Sharmila Goedhart^{3,8}, Fernando Camilo³

¹Department of Astronomy, University of Cape Town, Private Bag X3, Rondebosch 7701, South Africa

²Research Center for Intelligent Computing Platforms, Zhejiang Laboratory, Hangzhou 311100, China

³South African Radio Astronomy Observatory (SARA0), 2 Fir Street, Observatory, 7925, South Africa

⁴UK Astronomy Technology Centre, Royal Observatory Edinburgh, Blackford Hill, Edinburgh EH9 3HJ, UK

⁵The Inter-University Institute for Data Intensive Astronomy (IDIA), and University of Cape Town, Private Bag X3, Rondebosch, 7701, South Africa

⁶International Centre for Radio Astronomy Research (ICRAR), University of Western Australia, Crawley, WA 6009, Australia

⁷INAF – Osservatorio Astronomico di Cagliari, Via della Scienza 5, 09047, Selargius (CA), Italy

⁸SKAO, 2 Fir Street, Black River Park, Second Floor, Block A, Cape Town, 7925

Accepted 2024 May 24. Received 2024 May 22; in original form 2024 February 2

ABSTRACT

We conducted a search for H I emission of the gas-rich galaxies in the Vela region ($260^\circ \leq \ell \leq 290^\circ$, $-2^\circ \leq b \leq 1^\circ$) to explore the Vela Supercluster (VSCL) at $V_{\text{hel}} \sim 18000 \text{ km s}^{-1}$, largely obscured by Galactic dust. Within the mostly RFI-free band ($250 < V_{\text{hel}} < 25000 \text{ km s}^{-1}$) of MeerKAT, the analysis focuses on 157 hexagonally distributed pointings extracted from the SARA0 MeerKAT Galactic Plane Survey located in the Vela region (Vela–SMGPS). These were combined into 10 contiguous mosaics, covering a $\sim 90 \text{ deg}^2$ area. Among the 843 H I detected sources, 39 were previously discovered in the Parkes HIZOA survey ($V_{\text{hel}} < 12000 \text{ km s}^{-1}$; rms $\sim 6 \text{ mJy beam}^{-1}$). With the improved rms level of the Vela–SMGPS, i.e., $0.29 - 0.56 \text{ mJy beam}^{-1}$, our study unveils nearly 12 times more detections (471 candidates) in that same velocity range. We furthermore could identify 187 galaxy candidates with an H I mass limit reaching $\log(M_{\text{HI}}/M_\odot) = 9.44$ in the VSCL velocity range $V_{\text{hel}} \sim 19500 \pm 3500 \text{ km s}^{-1}$. We find indications of two wall-like overdensities that confirm the original suspicion that these walls intersect at low latitudes around longitudes of $\ell \sim 272^\circ - 278^\circ$. We also find a strong signature most likely associated with the Hydra/Antlia extension and evidence of a previously unknown narrow filament at $V_{\text{hel}} \sim 12000 \text{ km s}^{-1}$. This paper demonstrates the efficiency of systematic H I surveys with the SKA precursor MeerKAT, even in the most obscured part of the Zone of Avoidance (ZOA).

Key words: catalogs – surveys – galaxies: distances and redshifts – galaxies: general – radio lines: galaxies – cosmology: large-scale structure of Universe.

1 INTRODUCTION

On large scales, galaxies are arranged in a web-like pattern comprising groups, filamentary structures with high-density clusters at their nodes, surrounding low-density voids – known as the ‘cosmic web’ (Bond et al. 1996). Due to the gravitational instability exerted by these mass variations on their surrounding medium, these overdense – and underdense – regions induce a peculiar velocity or cosmic flow field that deviates from a pure Hubble expansion (e.g., Peebles 1976; Lauer & Postman 1994; Strauss & Willick 1995). The Cosmic Microwave Background (CMB) dipole, for example, is explained by the peculiar motion of the Local Group (LG) with respect to the CMB with a velocity of around $620 \pm 15 \text{ km s}^{-1}$ and an apex at

$(\ell, b) = 271.9^\circ \pm 2.0^\circ, 29.6^\circ \pm 1.4^\circ$ (Planck Collaboration et al. 2020).

Numerous efforts have been made to delineate large-scale structures (LSS) and study cosmic flow fields in the nearby Universe thanks to research using data from (i) all-sky systematic redshift (e.g., CfA/CfA2, Huchra et al. 1983; Falco et al. 1999; SRS2, da Costa et al. 1998; 2dFGRS, Colless et al. 2001, 2003; 6dFGRS Jones et al. 2009; 2MRS, Huchra et al. 2012; Macri et al. 2019; SDSS, Tempel et al. 2014; Ahumada et al. 2020) and (ii) peculiar velocity surveys (e.g., SFI++, Masters et al. 2006; Springob et al. 2007; 2MTF, Masters et al. 2007; Springob et al. 2016; Hong et al. 2019; 6dFGSv, Springob et al. 2014; Scrimgeour et al. 2016; Cosmicflows-3 or CF3, Tully et al. 2016; SDSS PV, Howlett et al. 2022; and Cosmicflows-4 or CF4 Kourkchi et al. 2020; Tully et al. 2023).

* E-mail: aychasam@gmail.com

In spite of these advancements, neither the local bulk flow direction nor the volume as determined independently from these large data sets are fully coherent with the CMB dipole measurements (e.g., [Erdođdu et al. 2006a,b](#); [Lavaux et al. 2010](#); [Hoffman et al. 2017](#); [Howlett et al. 2022](#)). Discrepancies persist in the literature (see e.g., Table 5 in [Scrimgeour et al. 2016](#)). On scales less than $150 h^{-1}$ Mpc, some studies show unusually large bulk flow amplitudes with respect to Λ CDM predictions ([Hudson et al. 2004](#); [Erdođdu et al. 2006a,b](#); [Watkins et al. 2009](#); [Feldman et al. 2010](#); [Lavaux et al. 2010](#); [Howlett et al. 2022](#)), while others present lower or consistent values ([Colin et al. 2011](#); [Branchini et al. 2012](#); [Turnbull et al. 2012](#); [Hoffman et al. 2015](#); [Scrimgeour et al. 2016](#); [Qin et al. 2018, 2019](#); [Qin 2021](#)).

The so-called ‘‘Zone of Avoidance’’ (ZOA; [Proctor 1878](#); [Shapley 1961](#); [Kraan-Korteweg & Lahav 2000](#)), is considered to be a major contributor to these controversies ([Loeb & Narayan 2008](#)) due to the incomplete mapping of the sky at low Galactic latitudes. Deep optical surveys in the ZOA (mostly photometric, see [Kraan-Korteweg & Lahav 2000](#); [Kraan-Korteweg 2005](#) for reviews) have significantly reduced its extent by covering lower latitudes (out to $|b| \leq 5^\circ$) and higher levels of extinction ($A_B \leq 3^{m0}$). These surveys unveiled nearby dynamically significant structures such as the Norma cluster ([Woudt 1998](#)) the Puppis cluster ([Lahav et al. 1993](#)), and the Ophiuchus cluster ([Hasegawa et al. 2000](#); [Wakamatsu et al. 2005](#)) out to $V_{\text{hel}} < 9000 \text{ km s}^{-1}$. Despite these efforts, the ZOA gap persists, affecting about 20% of the sky in optical wavelengths.

This degree of obstruction diminishes, but not entirely, as we move towards longer wavelengths, e.g., Infrared (IR) wavelengths are less affected by extinction. For instance, the 2MASS Redshift Survey (2MRS), provided systematic follow-up redshifts across the entire sky for all the brightest galaxies from the near-IR (NIR) 2MASS Extended Source Catalog (2MASS XSC; [Jarrett et al. 2000](#)). This survey NIR redshift is 97.4% complete down to $K_S \leq 11.75$ mag and $|b| \geq 5^\circ$, i.e., leaving 10% of the sky uncharted in a systematic way. Obtaining redshifts for these partly obscured red galaxies is very hard, if not impossible. It was only recently that [Macri et al. \(2019\)](#) have added 1041 new redshift measurements to the 2MRS NIR catalog to complete it, reducing the previous lack of redshift information for galaxies located near the ZOA.

A new avenue now exists with data from the Wide-field Infrared Survey Explorer catalog (WISE, [Wright et al. 2010](#); [Cutri et al. 2021](#)) in the mid-IR band. The most recent efforts in addressing the ZOA gap have been undertaken by [Daza-Perilla et al. \(2023\)](#), who introduced an automated classification system to distinguish galaxies from non-galaxies in low Galactic latitude regions using data from the VVV NIR Galaxy Catalogue ([Baravalle et al. 2021](#)).

In addition to the incomplete mapping of galaxies behind the ZOA, bulk flow measurements conducted so far face constraints due to the volumes they have surveyed. Bulk flows derived from the IRAS Point Source catalog redshift survey (PSCz; [Hudson et al. 2004](#)), the 6dF Galaxy Survey (6dFGS; [Springob et al. 2014](#)), and the 2MASS Tully-Fisher survey (2MTF; [Hong et al. 2014, 2019](#)) have only considered structures below 10000, 12000, and 16000 km s^{-1} , respectively. The more recent surveys hint at a ‘residual bulk flow’ originating from a hidden mass overdensity behind the ZOA (cf. [Hudson et al. 2004](#); [Loeb & Narayan 2008](#); [Boruah et al. 2020](#)). For example, the 6dFGS and 2MTF surveys implied a residual bulk flow of $\sim 273 \text{ km s}^{-1}$ towards the constellation of Vela ($\ell \sim 270^\circ - 330^\circ$) in the ZOA and induced beyond $V_{\text{hel}} > 16000 \text{ km s}^{-1}$ ([Springob et al. 2014, 2016](#); [Scrimgeour et al. 2016](#)).

Based on multi-object spectroscopic observations, [Kraan-Korteweg et al. \(2017\)](#), hereafter [KK2017](#), recently uncovered the Vela Supercluster (VSCL). VSCL, centered at $\ell = 272.5^\circ \pm 20^\circ$ and

$b = 0^\circ \pm 10^\circ$, hence in close proximity to the volume range and the direction over which this residual bulk flow motion is expected to arise. Using data from the Southern African Large Telescope (SALT), followed by data from AAOmega+2dF, [KK2017](#) have uncovered a massive concentration of galaxies at a redshift of $V_{\text{hel}} \sim 18000 \text{ km s}^{-1}$. This concentration extends over $115 \times 90 h_{70}$ Mpc at this distance, with an estimated overdensity of $\delta \sim 0.50 - 0.77$. The inspection of VSCL’s distribution in redshift space revealed a multi-branching morphology consisting of two wall-like structures. A main wall that is visible on both sides of the Galactic Plane (GP) at 18000 km s^{-1} , and a second smaller one below the GP at 22000 km s^{-1} . They seem to cross in the inner ZOA, which is unfortunately obscured. Although VSCL’s inner part could not be traced because of the high extinction and high stellar crowding in the optical and NIR at the lowest latitudes ($|b| \leq 5^\circ$), a contribution to the motion of the LG based on a complete set of 2MASS galaxies on either side of the GP between $6^\circ \leq |b| \leq 10^\circ$ is estimated to be $V_{\text{LG}} \approx 50 \text{ km s}^{-1}$ ([KK2017](#)). VSCL could therefore play a crucial role in explaining the residual bulk flow and refining our understanding of the Universe’s dynamics. Further kinematic evidence based on reconstructed density and velocity field data reinforces the presence of VSCL with the two merging walls hiding a dense core (see [Sorce et al. 2017](#); [Courtois et al. 2019](#)).

As a result, it is essential to trace VSCL across the ZOA, including areas of high obscuration, to gain a better understanding of its extent and mass overdensity. The most effective method to overcome this challenge is systematic HI surveys, given that the 21-cm HI emission passes unhindered through the ZOA. Previous single-dish surveys such as the Dwingeloo Obscured Galaxy Survey (DOGS, [Rivers et al. 1999](#)), the HI Parkes Zone of Avoidance survey (HI-ZOA, [Staveley-Smith et al. 2016](#)), the deep Arecibo L-band Feed Array Zone of Avoidance survey (ALFAZOA, [McIntyre et al. 2015](#)), or interferometric surveys such as the Westerbork Radio Synthesis Telescope survey of the Perseus-Pisces filament (WSRT PP, [Ramatsoku et al. 2016](#)) have demonstrated their capabilities in mapping structures bisected by the ZOA. Yet, none of these surveys had the required sensitivity, velocity coverage, and field of view to effectively map the VSCL. This makes MeerKAT ideal for observing the VSCL. A pilot project using MeerKAT16 data has already successfully mapped the galaxy cluster VC04 ($\ell \sim 272.25^\circ$, $b \sim -9^\circ$, $V_{\text{hel}} \sim 18000 \text{ km s}^{-1}$) embedded in the main VSCL wall ([Steyn 2023](#)). With a mean rms noise of $1.2 \text{ mJy beam}^{-1}$, the 6 pointings have led to the detection of 119 galaxies.

In this paper, we use *interferometric* HI data obtained as part of the SRAO MeerKAT Galactic Plane survey (referred to as SMGPS) to investigate the HI emission from the gas-rich galaxy population within the densest layer of the Milky Way plane and focus on learning more about the crossing of the VSCL walls. Firstly, the better spatial resolution and sensitivity compared to the previously undertaken surveys in the ZOA, the L-band frequency coverage, and the field of view of SMGPS will enable us to extend the depth of our study to 25000 km s^{-1} . Secondly, the SMGPS footprint encompasses the VSCL region. This paper presents the first result of an extensive exploration with a particular emphasis on mapping the uncharted inner core of the VSCL and uncovering possible intersections between its two walls through systematic HI surveys with MeerKAT. A dedicated survey, linking this finding to known structures beyond the ZOA will be detailed in an upcoming publication ([Rajohnson et al. in prep.](#)). By detecting a significant portion of the star-forming, gas-rich population within the VSCL, we aim to derive a qualitative estimation of the supercluster’s mass overdensity and gain insights into its contribution to the local bulk flow.

This paper is structured as follows: in Section 2, we describe the observation details, data reduction processes, and mosaicking strategies of Vela–SMGPS. We explain the methods used to detect sources and verify the measured fluxes in Section 3. Section 4 presents an overview of the source finding results of the highly-obscured galaxies and includes a completeness estimation. This is followed by a comparison of the HI properties with predictions based on simulations in Section 5, and a detailed discussion of the newly discovered LSS crossing the ZOA in Section 6. Finally, we summarize and conclude our findings in Section 7.

Throughout this paper, we use the heliocentric velocity in optical convention V_{hel} , $H_0 = 70 \text{ km s}^{-1} \text{ Mpc}^{-1}$, $\Omega_m = 0.3$ and $\Omega_\Lambda = 0.7$ (Hinshaw et al. 2013).

2 MEERKAT OBSERVATIONS AND DATA PROCESSING

2.1 The SARAO MeerKAT Galactic Plane Survey

SMGPS is an L-band (856–1712 MHz) continuum survey centered at 1.3 GHz, covering the longitude range $251^\circ \leq \ell \leq 61^\circ$ within a narrow strip with a width of $\Delta b = 3^\circ$ centered along the GP. With approximately 900 pointings, the latitude range was slightly adjusted to approximate the warp in the Milky Way disc. Within the longitude range $298^\circ \leq \ell \leq 61^\circ$, the corresponding latitude range covered is $-1.5^\circ \leq b \leq 1.5^\circ$. In contrast, within the longitude range of $251^\circ \leq \ell \leq 298^\circ$, the survey encompasses the latitude range $-2^\circ \leq b \leq 1^\circ$.

The primary objective of SMGPS is to study the continuum emission of the Galactic populations, e.g., Supernovae remnants, Planetary Nebulae, H II regions, etc. (for more details, see Goedhart et al. 2023). However, its technical capabilities also enable the exploration of the hidden extragalactic LSS located behind the innermost Milky Way, such as the Great Attractor ($302^\circ \leq \ell \leq 332^\circ$, GA–SMGPS, Steyn et al. 2024), and the Local Void ($328^\circ \leq \ell \leq 55^\circ$, LV–SMGPS, Kurapati et al. 2024), using its HI data. Our region of interest in this work is centered on the proposed crossing of the VSCL at $\ell \sim 275^\circ$, Vela–SMGPS. It spans 30° in longitude, extending from $260^\circ \leq \ell \leq 290^\circ$, with $-2^\circ \leq b \leq 1^\circ$, covering a $30^\circ \times 3^\circ$ (90 deg²) area.

2.2 Observations and data reduction

The deep observations (~ 1 hr per pointing) were performed between July 2018 and March 2020, using the full MeerKAT array, in full polarization. Each observing block of Vela–SMGPS, i.e., the set of data collected during one observation session, comprises 9 MKT pointings arranged in a hexagonal pattern. The pointing centers were offset by 0.494° to reach uniform sensitivity. Table 1 provides details of the analyzed region. It contains 157 individual fields observed during 19 blocks of observations, with a minimum of 58 antennas up to a maximum of 63 per observation. Due to scheduling constraints, two of these blocks were identical but split over multiple nights of observations. The observations were obtained with the 4K correlator mode and 8-second integration (Goedhart et al. 2023). With approximately 1 hour of on-source time per pointing, a session could last from 8.54 to 12.25 hours of on-track time. Typically, the complex phase calibrator (secondary calibrator) was visited for 65 seconds every 30 minutes after a cycle between the targets (~ 3 min per field), and the bandpass and flux calibrators (primary calibrators) were scanned for 5 minutes every 3 hours.

We transferred each relevant block (see Table 1) from the SARAO archive¹ into Ilifu², consisting of approximately 211 hours of total observing time. Throughout this process, autocorrelation data were excluded, and flags generated by the monitoring system of the Telescope were automatically applied. Using orthogonal polarization components (HH/VV) only, we processed the frequency range 1308 to 1430 MHz ($-2000 \leq V_{\text{hel}} \leq 26000 \text{ km s}^{-1}$), which is mostly free from Radio Frequency Interference (RFI), and omitted the frequency range associated with Milky Way HI emission, spanning from 1419.4 to 1421.4 MHz. This approach allows us to explore our volume of interest which is just at the border above which RFI becomes prominent. It covers the LSS out to $V_{\text{hel}} < 25000 \text{ km s}^{-1}$, encompassing the entire redshift range for the study of gas-rich spirals at the supercluster distance (approximately $V_{\text{hel}} \sim 16000 \text{ km s}^{-1}$ to about 23000 km s^{-1}), and constitutes a scientifically relevant volume for bulk flow studies (e.g., Scrimgeour et al. 2016).

We used the CARACal pipeline (Józsa et al. 2020) which is specifically designed for continuum and spectral line radio interferometry data reduction. CARACal operates a collection of STIMELA³ scripts (Makhathini 2018) – a framework based on Python and container technologies – which allows various radio interferometry software to make the calibration and imaging workflow running sequentially. RFI flagging was performed through Tricolour⁴ for the primary calibrator flagging and Tfcrop (a CASA⁵ task) for secondary calibrators flagging. Basic cross-calibration procedures such as delay, bandpass and gain calibrations were undertaken with CASA. Before self-calibration, we flagged target fields for RFI using AOflogger (Offringa 2010) with a strategy to only inspect the Stokes-Q amplitudes of the visibilities. The solution intervals obtained from calibration were then used to perform two iterations of self-calibration with Cubical (Kenyon et al. 2018).

2.3 HI imaging

To obtain emission-only visibilities, we initially subtracted the continuum sky model generated after self-calibration. We then applied a third-order polynomial subtraction to the visibilities using mstransform. Additionally, each data cube has been Doppler-corrected to the barycentric reference frame and regridded with a channel resolution of 210 kHz (corresponding to a velocity resolution of 44.3 km s^{-1} at $z = 0$) and the same start frequency of 1309 MHz to ensure they have the same number of channels, enabling their combination into mosaics (see Section 2.4).

We produced 157 dirty HI cubes of 570 channels each ($-1696 < V_{\text{hel}} < 25515 \text{ km s}^{-1}$) with a Briggs robust weighting parameter of $r = 0$, a pixel size of $3''$, and a taper of $15''$ using WSCLEAN (Offringa et al. 2014). We introduced a taper of $15''$ to reduce the non-Gaussian pattern of the dirty Point Spread Function (PSF), i.e., smoothing the wings visible by the black solid lines in Fig. 1, and improving the filling factor of extended low HI-column densities sources to increase the image fidelity (e.g., see Fig. 2). The tapered dirty beams are on average $30'' \times 27''$ with a variation of about $\pm 2''$ over the whole SMGPS survey, and approximately $29.7'' \times 26.3''$ ($\pm 1''$) in the 157 HI cubes' beam sizes throughout Vela–SMGPS.

¹ <https://archive.sarao.ac.za/>

² www.ilifu.ac.za

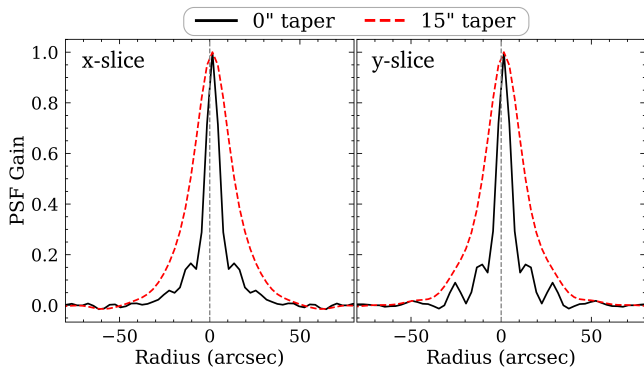
³ <https://github.com/SpheMakh/Stimela>

⁴ <https://github.com/ratt-ru/tricolour>

⁵ <http://casa.nrao.edu>

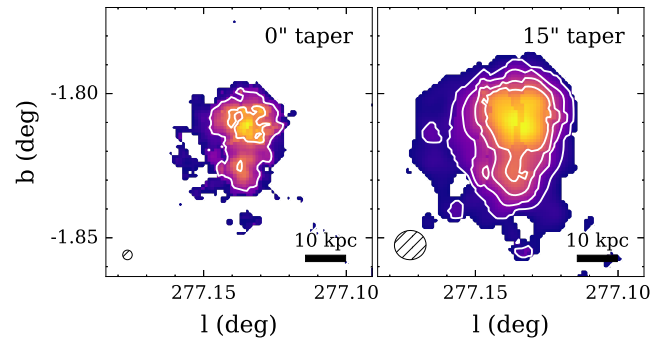
Table 1. Overview of Vela–SMGPS observational parameters

Date (UT start)	Block ID	Block centre (ℓ , b)	Track (h)	N_{ant}	Primary calibrator	Secondary calibrators
2018-12-30	1546207810	(291.8, 0.0)	12.02	62	1215-457	J1331+3030, J1939-6342
2018-12-31	1546293818	(291.3, -1.5)	12.25	62	1215-457	J1331+3030, J1939-6342
2019-01-01	1546380746	(288.4, -0.5)	11.99	62	1215-457	J1331+3030, J1939-6342
2019-01-04	1546641291	(285.4, 0.5)	10.51	61	J0906-6829	J0408-6545, J1331+3030, J1939-6342
2019-01-05	1546727810	(285.9, -1.0)	10.39	60	J0906-6829	J0408-6545, J1331+3030, J1939-6342
2019-01-06	1546811642	(282.9, 0.0)	10.00	60	J0906-6829	J0408-6545, J1331+3030, J1939-6342
2019-01-07	1546900349	(282.4, -1.5)	8.54	62	J0906-6829	J0408-6545, J1331+3030, J1939-6342
2019-01-08	1546984998	(279.5, -0.5)	9.97	62	1215-457	J1331+3030, J1939-6342
2019-01-09	1547071945	(276.5, 0.5)	9.32	62	1215-457	J1331+3030, J1939-6342
2019-01-12	1547330621	(277.0, -1.0)	9.31	62	J0825-5010	J0408-6545, J1331+3030, J1939-6342
2019-01-13	1547413577	(274.0, 0.0)	9.31	62	J0825-5010	J0408-6545, J1331+3030, J1939-6342
2019-01-14	1547499081	(273.6, -1.5)	9.72	62	J0825-5010	J0408-6545, J1331+3030, J1939-6342
2019-01-15	1547585175	(270.6, -0.5)	9.75	63	J0825-5010	J0408-6545, J1331+3030, J1939-6342
2019-01-17	1547758692	(267.6, 0.5)	9.31	58	J0825-5010	J0408-6545, J1331+3030, J1939-6342
2019-01-18	1547839876	(268.1, -1.0)	10.01	63	J0825-5010	J0408-6545, J1331+3030, J1939-6342
2019-11-16	1573939357	(265.2, 0.0)	12.03	61	J0825-5010	J0408-6545, J0521+1638, J1331+3030, J1939-6342
2019-11-15	1573852860	(264.7, -1.5)	12.02	61	J0825-5010	J0408-6545, J0521+1638, J1331+3030, J1939-6342
2019-11-22	1574456164	(261.7, -0.5)	11.67	60	J0825-5010	J0408-6545, J0521+1638, J1331+3030, J1939-6342
2019-11-23	1574542866	(259.7, 0.5)	10.89	60	J0825-5010	J0408-6545, J0521+1638, J1331+3030
2019-11-26	1574801265	(259.2, -1.0)	9.63	63	J0825-5010	J0408-6545, J0521+1638, J1331+3030
2019-11-28	1574911560	(259.2, -1.0)	2.39	61	J0825-5010	J0408-6545, J1331+3030

**Figure 1.** A 2D slice of the dirty PSF along the x and y axes in a Vela–SMGPS field. The black solid line shows the PSF without taper, the red dashed line indicates the PSF after a 15'' taper has been applied.

We can therefore spatially resolve galaxies with HI sizes larger than $\sim 37 \times 33$ (± 1.25) kpc or HI masses of $\log(M_{\text{HI}}/M_{\odot}) \geq 9.57 \pm 0.03$ at the VSCL distance, based on the HI size-mass relation (Rajohnson et al. 2022).

Figure 3 provides a visual representation of the pointing configuration for the 157 MeerKAT pointings in Vela–SMGPS. In the bottom panel, the color gradient, from yellow to dark red, illustrates the measured global rms noise values at the central region of each individual pointing. These values range from 0.28 to 1.09 mJy beam $^{-1}$. The fields with high rms noise (bottom panel) are closely related to the regions of extended continuum sources, e.g., $\ell \sim 283^{\circ} - 289^{\circ}$ and 267.5° (see top panel). Fortunately, only a few fields are affected by these large and bright continuum sources. Non-contaminated areas, on average, exhibit an rms noise value of 0.42 mJy beam $^{-1}$. The necessary data quality for our science goals can be achieved by mosaicking the MeerKAT pointings in hexagonal patterns, as detailed in the next section.

**Figure 2.** An example of the HI distribution without a taper (left) and a 15'' taper (right). PSFs with respective sizes of $12'' \times 11''$ and $30'' \times 27''$ are shown in the lower left corner of each image, while a 10 kpc scalebar is illustrated in the lower right corner.

2.4 Mosaicking strategy

We utilize the MONTAGE⁶ software within CARACal with the mosaic⁷ worker parameter set to spectral type for the generation of the mosaics. To perform the assembling and re-gridding, we input the dirty cubes along with their “Mauchian” Primary Beam (PB) models (i.e., a cosine-squared power illumination as seen in Mauch et al. 2020) in a common folder. Fields of 0.8° radius, corresponding to a normalized PB gain of 0.2, are used for mosaicking the PB-corrected dirty beams. This enhances the sensitivity and uniformity of the survey area.

The restoring beams mentioned in Section 2.3 vary from cube to cube and channel to channel. Therefore, the mosaic PSF is determined as the median value from the PSFs of each input cube in CARACal. We divide the Vela–SMGPS survey into 10 overlapping mosaics, named T24 to T33, each containing 22 fields. This results in each mosaic having its unique beam size. For example, mosaic

⁶ <http://montage.ipac.caltech.edu/>

⁷ <https://github.com/caracal-pipeline/MosaicQueen>

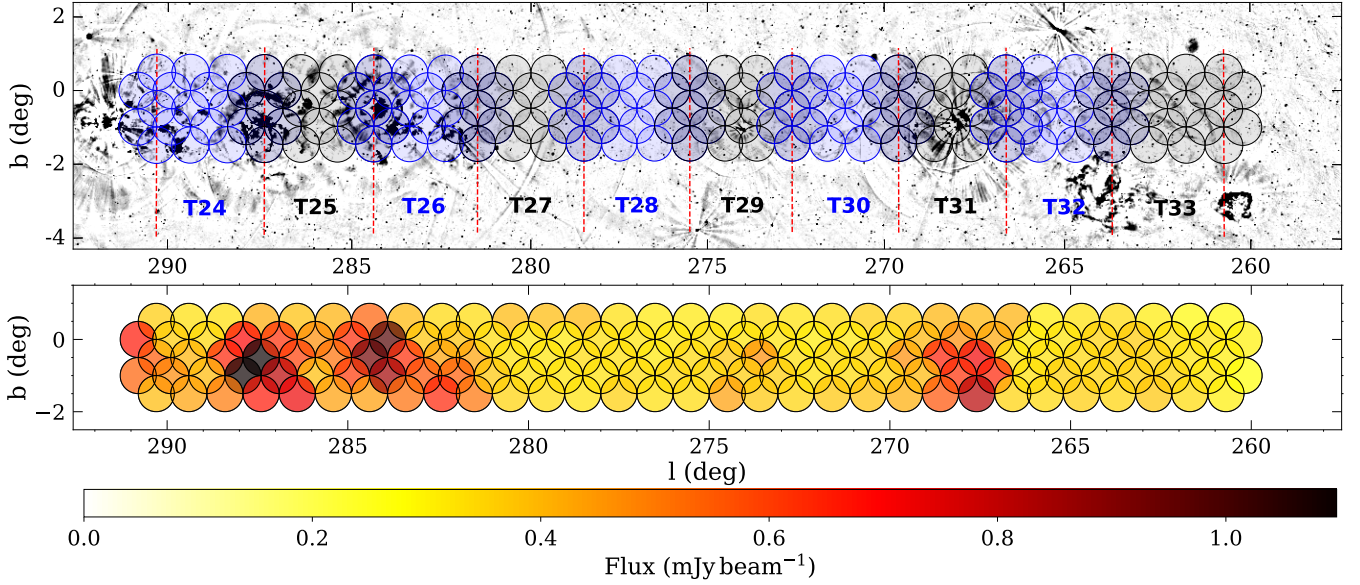


Figure 3. Pointing configuration of Vela–SMGPS ($260^\circ \leq \ell \leq 290^\circ$). *Top panel:* distribution of the 10 mosaics (T24–T33) of 22 fields each in the VSCL region, overlaid on the SUMSS continuum map (grayscale). *Bottom panel:* the corresponding rms levels of each field.

T24 has a PSF of $28.9'' \times 25.0''$ and T33 has $30.5'' \times 26.3''$. These beam sizes are used to estimate the flux for the detections they contain. The varying beam areas per channel and per cube in the mosaics exhibit a scatter ranging between 3% to 6% compared to the median mosaic beam area. This scatter, however, is negligible when compared to the statistical uncertainty of the fluxes (see Section 3.4.2).

One mosaic covers an area of the sky slightly over $5 \times 3.5 \text{ deg}^2$, producing a nearly uniform data cube of approximately $3.5 \times 3 \text{ deg}^2$. Each mosaic centre is offset by $\Delta\ell = 3^\circ$. This configuration ensures that we do not miss possible extended sources at the edges of the mosaic. It allows an independent data quality assessment of the source finding algorithm and their derived HI parameters from the overlapping area of $\Delta\ell \sim 1^\circ$ (see Section 3.4).

The CARACal run outputs three types of mosaics: the main mosaic containing the data and its corresponding weight and noise mosaics, all in fits format and projected in equatorial coordinates. To facilitate the analysis along the GP, we transformed the coordinates in Galactic coordinates using the CASA task `imregrid`, applied to the three mosaic files. The 10 final HI mosaics are indicated in the top panel of Fig. 3 (red dashed lines), superimposed on the Sydney University Molonglo Sky Survey (SUMSS) Galactic continuum map (Bock et al. 1999) in the top panel. The alternating blue and black MeerKAT pointings indicate the 22 pointings that conform one individual mosaic.

Due to the hexagonal configuration of the MeerKAT pointings, the rms after mosaicking is consistently lower. The 10 HI mosaics have rms values ranging from 0.29 to $0.56 \text{ mJy beam}^{-1}$, with a mean rms noise of $0.39 \text{ mJy beam}^{-1}$. Assuming a 200 km s^{-1} linewidth galaxy and a mean global rms of $0.39 \text{ mJy beam}^{-1}$, we can achieve a 5σ HI mass detection limit of $2.75 \times 10^9 M_\odot$ at the VSCL distance ($V_{\text{hel}} \sim 18000 \text{ km s}^{-1}$, $D \sim 257 \text{ Mpc}$). Table 2 lists the properties of the 10 Vela–SMGPS mosaics.

Table 2. Mosaicking parameters of Vela–SMGPS.

Mosaicking property	Value
Number of fields per mosaic	22
Number of mosaics	10 (T24 to T33)
Galactic longitude	$260^\circ \leq \ell \leq 290^\circ$
Galactic latitude	$-2^\circ \leq b \leq 1^\circ$
Total sky coverage	90 deg^2
Sky coverage per mosaic	$\sim 5 \times 3.5 \text{ deg}^2$
– with uniform sensitivity	$3.5 \times 3 \text{ deg}^2$
Velocity resolution	44.3 km s^{-1} at $z = 0$
Mosaic velocity range	$-1696 < cz < 25515 \text{ km s}^{-1}$
HI cube weighting	Briggs <i>robust</i> = 0
Pixel size	$3'' \times 3''$
HI cube size	2200×2200 pixels
Beam size (15'' tapering)	$29.7'' \times 26.3'' (\pm 1'')$
Mean global rms noise per channel	$0.39 \text{ mJy beam}^{-1}$
Mosaics rms range	$0.29 - 0.56 \text{ mJy beam}^{-1}$

3 SOURCE FINDING AND VERIFICATION

The following section details the algorithms used to arrive at a reliable list of HI detections. As a first step, we apply the automated source finder SoFiA-2 (Westmeier et al. 2021) for source identification after optimizing its parameters, as discussed in Section 3.1. We discuss a visual verification and classification method in Section 3.2 to differentiate between solid detections and possible ones. In Section 3.4, a search for duplicates in the overlapping regions of the mosaics is performed to check for internal consistency, and a comparison with HIZOA is conducted to assess the quality of the measured fluxes.

3.1 HI source finding

It is not realistic to perform source finding by eye for such large surveys. Hence, we used the HI Source Finding Application SoFiA-2⁸ (Westmeier et al. 2021), an automated source finding

⁸ <https://github.com/SoFiA-Admin/SoFiA-2>

and parameterization algorithm to identify galaxy candidates based on their HI emission. Due to continuum residuals, the rms noise level from pointing to pointing is not uniform (see bottom panel of Fig. 3). It is therefore crucial to optimize the parameter settings for SoFiA that performs reliably on all mosaics in finding the galaxy candidates, without resulting in a high number of false detections.

Our final source finding strategy is summarized below:

- (i) We first defined the search window for the input mosaic cube. Our three-dimensional search window was set to the central area of $3.5 \times 3 \text{ deg}^2$ ($\sim 4200 \times 3600 \times 517$ pixels) where the rms is mostly uniform. Figure 4 displays a sample mosaic, illustrating that the spatial noise variation remains small within the search area outlined by the black box. The source finding velocity range was from channel 9 to 525, i.e., $250 \leq V_{\text{hel}} \leq 25000 \text{ km s}^{-1}$.
- (ii) We normalized the noise level across the mosaic by adding the noise mosaic as an additional input to the pipeline. We used the ‘local’ scaling noise mode of SoFiA to correct for local noise variations within both the spectral and spatial domains of the data. This approach differs slightly from the one employed by Steyn et al. (2024), who used the ‘spectral’ scaling noise mode, relying solely on spectral domain correction. We chose a grid size of 301 pixels on the xy-axis and 15 channels on the spectral axis for this noise scaling step.
- (iii) The source finding step itself is performed with the ‘Smooth and Clip’ (S+C) finder algorithm, specifically designed for blind source detection. It smooths the mosaic with a set of spatial Gaussian filters and spectral boxcar kernels. We set these to (0, 7, 15) pixels, and (0, 135, 225, and 315) km s^{-1} , respectively. After each iteration of the smoothing process, the local rms noise is measured. SoFiA then clips all pixels below the source finding threshold of 4σ . The remaining pixels are stored in a source mask and, if connected pixels satisfy the specified linking radius set in the parameter file, they are merged into individual sources.
- (iv) Each detected source undergoes a reliability assessment using the method outlined in Serra et al. (2012). To be considered a valid detection and included in the SoFiA output catalog, a minimum SoFiA source-finding reliability threshold of 90% is set.
- (v) To ensure that sources near the detection threshold of the survey were not overlooked due to stochastic noise, we conducted a second run of SoFiA with a source finding threshold of 3.5σ . Both resulting SoFiA catalogs were cross-matched using `Cross_matching`⁹, duplicates were removed, and unique detections from each run were retained. After a verification process discussed in the next section, we obtained a final list of detections which also allowed us to reject false positives.

The final parameter settings, which encompass all these procedures, can be found in the SoFiA parameter file provided in Appendix A. The outlined approach was applied to all 10 mosaics.

3.2 Source classification

For the verification process, a Python script was created to automatically generate total flux density (mom-0), velocity field (mom-1) maps, and the global HI profiles for each detection listed in the SoFiA catalog, following the format shown in Fig. 5.

To generate moment maps and global HI profiles, we extracted cubelets with a spectral length of 10 MHz and dimensions defined by the bounding box results obtained from the SoFiA catalog around

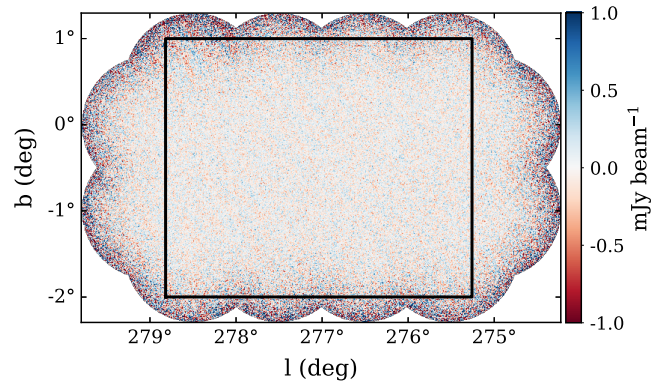


Figure 4. A random example showing spatial noise variation for a central channel map ($\text{rms} = 0.29 \text{ mJy beam}^{-1}$) in a Vela–SMGPS mosaic. The black rectangle outlines the SoFiA source-finding region.

each HI detection. Additionally, we added extra padding of $30''$ to $1'$ in both longitude and latitude depending on the redshift of the detection to account for the noise outside the source. To compute mom-0 and mom-1 maps, we selected the cubelet channels both before and after the systemic velocity provided by SoFiA, each with widths equal to half of the linewidth at the 20% peak flux density (w_{20}) and an additional channel on both sides. A 3σ clipping threshold was therefore applied, where σ is the local rms derived from four emission-free areas around each detected HI signal, used to mask the moment maps.

After the production of these data products, we performed visual verification simultaneously on the spectrum, unmasked mom-0 maps (to assess noise levels surrounding the source), and on masked mom-1 maps. Each potential detection was classified as ‘solid’, ‘possible’, or ‘reject’ according to the following qualitative guidelines:

To be considered a solid detection, firstly, the global HI profile should exhibit a clear peak with a relatively flat baseline, and the signal should be well above the noise level. Additionally, the source should have a well-defined disc in the mom-0 map and a distinct velocity field with evident rotation over at least two channels in the mom-1 map.

Special attention is given to compact sources less extended than 1.5 times the beam size. Such sources typically have an integrated signal-to-noise ratio (SNR) of less than 6, indicating low completeness and reliability. Faint unresolved sources with $\text{SNR} \leq 6$ (see Eq. 9) were conservatively moved from the solid to the possible detection list as they were difficult to distinguish from noise peaks visually. Similarly, in cases of low-velocity gradient (especially if a single channel peak), sources with low SNR are moved to the possible detection list.

In cases where one of these criteria is not met, but the detection is still deemed to be real, it is classified as a possible detection. An example is shown in the second panel of Fig. 5, where despite an evident rotation spanning four channels, its extent is only about the size of the beam. Additionally, this detection presents an integrated SNR of approximately 5. The highest point in its spectrum is also not very clear due to the varying noise in the detection area.

A detection is otherwise labeled as a reject. For instance, the existence of an extremely large source compared to its beam size (see bottom panel of Fig. 5), or a small dwarf, is not likely to be detectable in this survey at high redshift. This could also arise from a small noise peak (few pixels) that SoFiA misinterpreted as a detection, a source detected in more than 20 channels, or the identification of an imaging artifact caused by a residual continuum. The latter

⁹ https://github.com/TrystanScottLambert/Cross_Matching

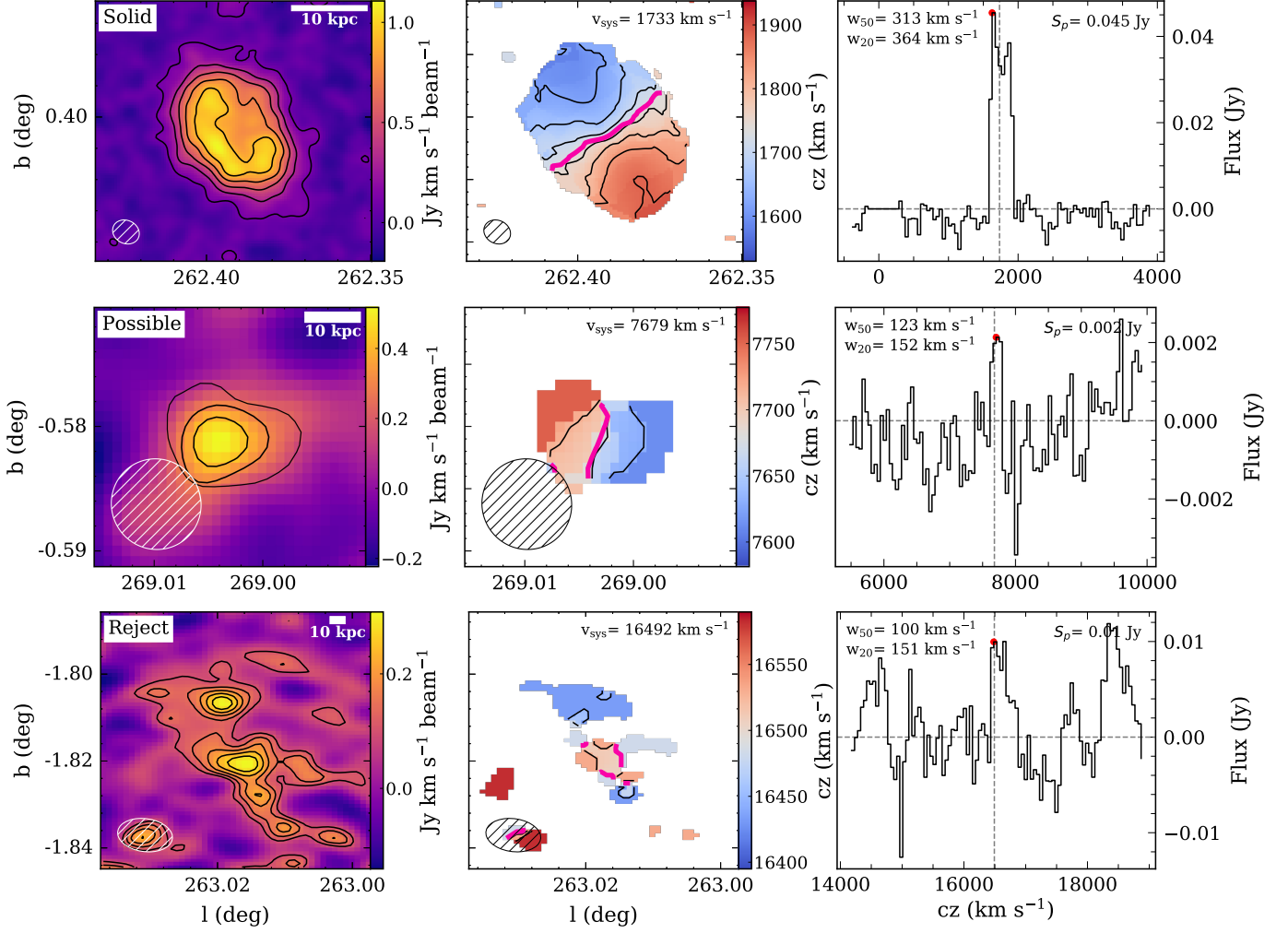


Figure 5. The three visual classifications of SoFiA detected sources: “Solid”, “Possible”, and “Reject” (from top to bottom). *Left panel:* Total flux (mom-0) map in Galactic coordinates with a color bar, a 10 kpc scale bar at the top, and the synthesized beam (white hatched ellipse) at the bottom corner. *Middle panel:* Masked mom-1 map in Galactic coordinates with a color bar revealing velocity fields. The heliocentric velocity is given in the top right corner and indicated as a magenta contour. *Right panel:* Global H I profile with a dashed vertical line indicating the heliocentric velocity of the galaxy; measured linewidths at 50% and 20% of the peak flux density are presented in the top left corner, with the peak flux density value denoted by the red point shown in the top right corner.

assessment was facilitated by an additional visual verification of each detection using CARTA¹⁰ – an interactive Astronomy Visualization tool. The adjudication process involved multiple team members to ensure the robustness of the source verification. Figure 5 displays typical examples of these three categories.

We then cataloged a total of 843 detections, comprising 646 solids and 197 possible detections based on this classification scheme. Given that SoFiA provides an estimate of the reliability of each source as defined by Serra et al. (2012), we used those individual reliability values to determine the estimated number of false detections present in the catalog. We estimate a value of 6.4% for false detections among possible detections, while solid detections yield a false detection rate of just 1.4%. Since multiple team members also inspected the moment maps visually, these estimates are likely to represent upper limits.

These detections were compiled into a Galaxy Atlas, which showcases their masked moment maps and H I global profiles. The

Galaxy Atlas is available at <https://doi.org/10.5281/zenodo.11160742>. Table 3 provides the number of detected sources per SoFiA run and per mosaic, their final classifications, as well as the average global and local rms variations per mosaic. The per-channel local rms noise of the 843 detections ranges from 0.22 to 0.94 mJy beam $^{-1}$, with an average of 0.33 mJy beam $^{-1}$. This is lower than the average global rms value of the mosaics and is consistent for solid and possible detections (see peak in Fig. 6). The solid and possible detections from each mosaic are combined into a final catalog (see Section 4 for details) with flags according to their classifications.

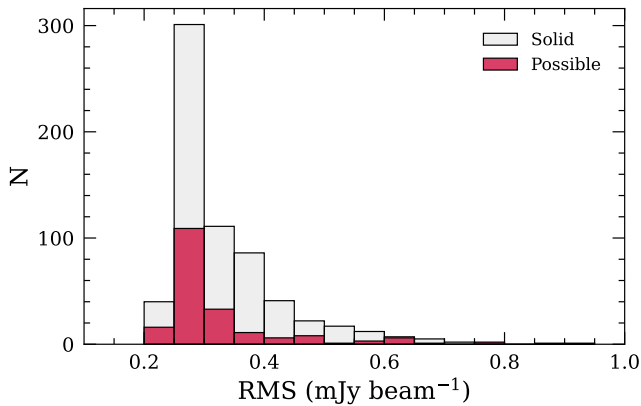
3.3 Parameterization

The SoFiA output list provides source parameters in native pixels and flux units. To convert them into physical parameters, such as centroid positions (in pixels) into Galactic coordinates (l and b in degrees), and to enable SoFiA to adjust the integrated fluxes (S_{int}) by the beam solid angle, we set SoFiA parameter.wcs and parameter.physical to True.

¹⁰ <https://cartavis.github.io>

Table 3. Number of detected sources per mosaic after the two SoFiA runs, including cross-matching, elimination of duplicates between mosaics, and visual verification. The last column presents the measured global and local rms values determined around detections.

Mosaic	Thresholds		Total retained (w/o dupl.)	Solid	Possible	Mean rms (mJy beam ⁻¹)	
	3.5σ	4σ				Global	Local
T24	51	65	54	42	12	0.47	0.39 ± 0.12
T25	56	58	32	25	7	0.49	0.50 ± 0.12
T26	60	72	53	48	5	0.50	0.41 ± 0.11
T27	137	155	116	97	19	0.30	0.32 ± 0.09
T28	108	116	102	65	37	0.29	0.28 ± 0.04
T29	98	111	91	70	21	0.31	0.29 ± 0.06
T30	120	134	114	92	22	0.30	0.31 ± 0.08
T31	119	107	75	52	23	0.56	0.38 ± 0.09
T32	131	125	103	72	31	0.31	0.31 ± 0.08
T33	138	139	103	83	20	0.33	0.30 ± 0.07
Total			843	646	197		

**Figure 6.** Histogram depicting the local rms noise measured around each solid detection (shaded in grey) and possible detection (shaded in red).

We first convert the SoFiA output parameters. The heliocentric systemic velocity V_{hel} is determined from the central frequency of the H I profile relative to the optical definition using the equation:

$$V_{\text{hel}} = c \left(\frac{\nu_0}{\nu} - 1 \right) = cz, \quad (1)$$

where c is the speed of light, ν_0 is the rest-frequency of the 21 cm line, and z is the observed barycentric redshift. No corrections have been applied to V_{hel} for the barycentre of the Local Group (V_{LG}).

In a few isolated cases, where the detection was composed of one or more companions, the SoFiA central frequency has been found slightly off-center. We then determined the systemic velocity as follows:

$$V_{\text{hel}} = 0.25(\nu_{20}^A + \nu_{50}^A + \nu_{20}^R + \nu_{50}^R), \quad (2)$$

where ν_{20} and ν_{50} are the corresponding velocities measured at the 20% and 50% levels of the peak flux densities (see Ramatsoku et al. 2016). A and R indicate the approaching and receding sides of the profile respectively.

We not only determined the systemic velocities but also calculated the linewidths and integrated fluxes of the detections. It is important to emphasize that the conversions were conducted using the source rest frame velocity convention, following the method outlined in Meyer et al. (2017).

To convert (w_{20}^V , w_{50}^V) from their default units in Hz to km s⁻¹, we

use the equation:

$$w = \frac{c(1+z)}{\nu_0} w^V. \quad (3)$$

When the signal-to-noise ratio is low, SoFiA could output an under- or overestimate, where the values of w_{20} and w_{50} are erroneously identical, contrary to what is expected in the spectrum. In such cases, we re-calculated the linewidths as:

$$w_{20} = \nu_{20}^R - \nu_{20}^A \quad \text{and} \quad w_{50} = \nu_{50}^R - \nu_{50}^A. \quad (4)$$

The 20% and 50% levels are measured from the first crossings of the peak flux density. The differences between the SoFiA linewidths and the re-calculated ones are on the order of half to one channel width. Additionally, the resulting linewidths have been corrected for instrumental broadening according to the method outlined in For et al. (2021) and Springob et al. (2005):

$$w^c = \frac{c(1+z)}{\nu_0} \sqrt{(w^V)^2 - (\Delta\nu)^2}, \quad (5)$$

where $\Delta\nu = 210$ kHz is the observed frequency width. Using Eq. 3, this can be further simplified to:

$$w^c = \sqrt{w^2 - (\Delta V)^2}. \quad (6)$$

Moreover, the default output from SoFiA for the integrated flux S^V is in Jy Hz. To determine the H I mass in Solar masses (M_{\odot}), we directly apply equation 48 from Meyer et al. (2017):

$$\left(\frac{M_{\text{HI}}}{M_{\odot}} \right) = 49.7 \left(\frac{D}{\text{Mpc}} \right)^2 \left(\frac{S^V}{\text{Jy Hz}} \right), \quad (7)$$

where $D = V_{\text{hel}}/H_0$ represents the Hubble distance in Mpc. For comparison purposes in the following sections, we convert the integrated fluxes (S^V) from Jy Hz to Jy km s⁻¹ (S^V), using the source rest frame convention:

$$S_{\text{int}} = \left(\frac{S^V}{\text{Jy km s}^{-1}} \right) = \frac{c(1+z)}{\nu_0} \left(\frac{S^V}{\text{Jy Hz}} \right). \quad (8)$$

3.4 Quality assessment

3.4.1 Internal quality assessment

We first conducted an internal consistency check for sources located within the overlapping regions of the mosaics to ensure consistency in source-finding, and to assess internal data quality. A source from an overlapping region was identified in adjacent mosaics consisting

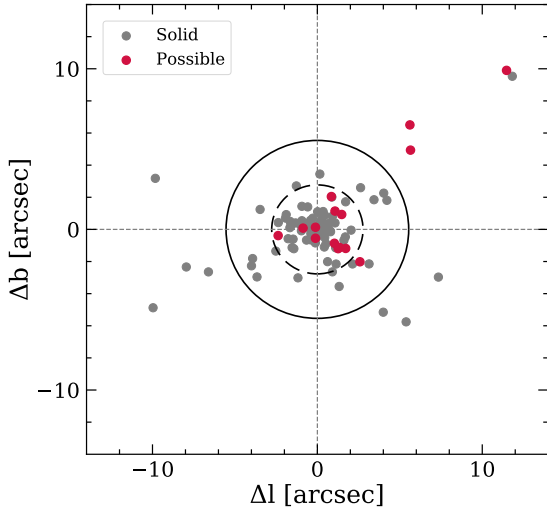


Figure 7. Internal coordinate offsets for detections found on overlapping regions of adjacent mosaics. Grey dots illustrate solid detections while red ones designate possible detections. The inner (dashed) and outer (solid) circles delimit the one and two sigmas standard deviations of $2.77''$ and $5.54''$, respectively.

of a slightly different configuration of pointings. We first investigated the positional agreement as demonstrated in Fig. 7. A mean coordinate precision of $2.16''$ with a 1σ standard deviation of $2.77''$ was achieved – less than one pixel size. No difference in positional offset between possible and solid detections was observed. We then examined the positional offsets as a function of the integrated signal-to-noise ratio (SNR; see Fig. 8). The integrated signal-to-noise ratio is defined as:

$$\text{SNR} = \frac{\sum S_i}{\sigma \sqrt{N_{\text{pix}} \Omega_{\text{PSF}}}}, \quad (9)$$

following the definition from Equation 4 in the SoFiA user manual¹¹. In this equation, $\sum S_i$ refers to the summation of flux densities within the source mask, σ is the local rms noise measured around the detection, N_{pix} denotes the total count of spatial and spectral pixels involved in the detection, and Ω_{PSF} indicates the beam solid angle measured in pixels.

Possible detections have on average a lower SNR compared to solid ones, while the 2σ -outliers (outside black solid circle in Fig. 7) all have $\text{SNR} < 25$. The coordinate separation is seen to decrease with increasing SNR as shown in Fig. 8.

The absolute differences in integrated fluxes, linewidths, and systemic velocities of the overlapping sources (i.e., the same object detected in two different mosaics) exhibit mean absolute errors and standard deviations in the range of $0.17 \pm 0.12 \text{ Jy km s}^{-1}$, $22 \pm 27 \text{ km s}^{-1}$, and $10 \pm 12 \text{ km s}^{-1}$, respectively. These values are consistent with their errors, and uncertainties in linewidths and velocities are well below the coarse channel resolution. However, for sources with very low SNR and detections situated close to the mosaic edges, the masking threshold may vary if the rms values differ in the two mosaics, potentially leading to larger flux uncertainties.

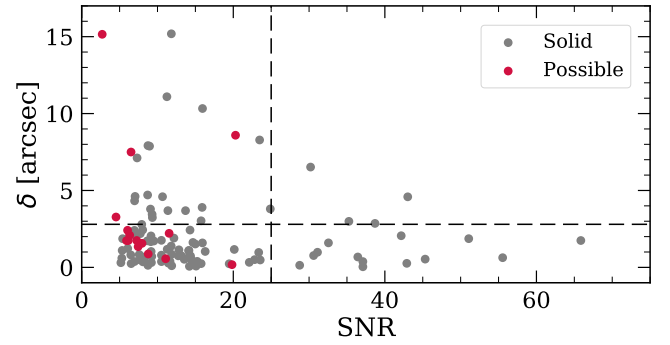


Figure 8. Vela–SMGPS internal coordinate offsets as a function of integrated signal-to-noise ratio (SNR). Red and grey dots represent possible and solid detections. Horizontal and vertical dashed lines mark the coordinate precision 1σ standard deviation, and an SNR of 25, respectively.

3.4.2 Ancillary data comparison

In the next step, we quantify the accuracy of Vela–SMGPS H I parameters. Despite the high extinction in the inner ZOA, we utilized the NASA/IPAC Extragalactic Database (NED)¹², and the Vizier¹³ Catalogue access tool to search for Optical, IR, and H I counterparts within our survey region. The search radius was determined in quadrature to the positional uncertainty of Vela–SMGPS (as discussed in Section 3.4.1) and the typical coordinate precision of the catalog used for comparison. For instance, we conducted searches within a radius of $10''$ from each galaxy’s position for OPT/IR counterparts, and $\sim 4'$ for H I counterparts, considering that HIZOA galaxies (Staveley-Smith et al. 2016) are with few exceptions the only H I counterparts available at these latitudes.

Out of 843 detections, 57 detections ($\sim 7\%$) have likely IR and/or H I counterparts in the existing literature. Among these 57, the distribution of IR counterparts is as follows: 7 (12%) have IRAS counterparts, 40 (70%) are associated with 2MASS/2MASX counterparts, 50 (88%) are identified with WISE counterparts, and 17 (30%) have IRSF counterparts. The median coordinate separation between the H I position and the potential IR counterpart is approximately $3.3''$.

In terms of H I counterparts, our survey area encompasses 39 HIZOA detections (68% of 57), with 6 of them also detected in HIPASS (Meyer et al. 2004). Vela–SMGPS successfully retrieved all HIZOA detections. Interestingly, we recovered the most H I-massive spiral galaxy hidden behind the Milky Way, identified as HIZOA J0836-43 (see Kraan-Korteweg et al. 2005), named SMGPS-HI J083650-433738 in Vela–SMGPS (displayed in the top left panel of Fig. B1). This galaxy is the most H I-massive object within the entire HIPASS volume, and underwent subsequent follow-up observations with the Australia Telescope Compact Array (ATCA; Donley et al. 2006). This optically obscured galaxy was found to be a Luminous Infrared Galaxy (LIRG) with an actively star-forming disk spanning over 50 kpc (Cluver et al. 2010).

We used both the ATCA and HIZOA data for this H I massive galaxy to examine the consistency in our positions, fluxes, velocities, and linewidths. We observe a positional difference of $9''$ and $23''$, respectively. While the ATCA and HIZOA measurements report integrated H I flux densities of $14.5 \pm 0.7 \text{ Jy km s}^{-1}$ and $14.38 \pm 1.69 \text{ Jy km s}^{-1}$, our analysis using Vela–SMGPS yields

¹¹ <https://gitlab.com/SoFiA-Admin/SoFiA-2/-/wikis/home#resources-and-documentation>

¹² <http://ned.ipac.caltech.edu>

¹³ <https://vizier.cds.unistra.fr/viz-bin/VizieR>

a value of $15.15 \pm 1.59 \text{ Jy km s}^{-1}$. All three measurements fall within the range of expected errors, indicating excellent agreement with each other. The slightly higher flux value of J083650 in Vela-SMGPS may be attributed to its position near the mosaic edge. We observed higher noise levels and baseline irregularities in this area, which could have influenced this case’s flux measurement. Moreover, the systemic velocities and linewidths exhibit exceptional agreement with the HIZOA results after correcting the linewidths for instrumental broadening. Both show differences of 8 km s^{-1} in the velocities and w_{20} , while only 1 km s^{-1} for w_{50} . When compared to ATCA data, there is a 10 km s^{-1} difference in velocities, and larger offsets of 30 km s^{-1} and 15 km s^{-1} are observed in the w_{50} and w_{20} values, respectively.

The comparison with the sole interferometric dataset within our survey region provides consistent measurements. However, the statistical analysis is limited to only one galaxy. Hence, we utilize the HIZOA dataset for an independent comparison of H I parameters, given its unique status as the only source with redshift information in our multi-wavelength counterpart search.

The 39 HIZOA galaxies are identified out to 12000 km s^{-1} . The Vela-SMGPS dataset comprises 471 detections within this velocity range, marking a noteworthy twelve-fold increase in the galaxy count. The mean positional offset is $\sim 2'$, a reasonable value given the large $\sim 15.5'$ beam size of HIZOA. This is also consistent with findings between HIZOA/HIPASS and other data sets (e.g., [Staveley-Smith et al. 2016](#)). Six of the HIZOA detections were resolved into several distinct H I sources due to the higher resolution of the MeerKAT interferometric data. Figure 9 presents an illustration of two examples, showcasing HIZOA J0913-48 blended into two distinct sources, and HIZOA J0917-49 with a satellite companion as seen in their H I distributions. Moment maps of the 39 HIZOA detections as observed by Vela-SMGPS are shown in Appendix B. Furthermore, 19 of these HIZOA detections have likely WISE counterparts.

Figures 10, 11, and 12 display the comparison between the linewidths, systemic velocities, and integrated fluxes of the Vela-SMGPS detections and their corresponding HIZOA counterparts. Out of the 39 detections, we excluded detections that are conformed of multiple counterparts or close to a continuum residual artifact, leaving 31 detections for comparison.

The 50% peak flux density linewidths show a nearly indistinguishable deviation from a one-to-one relation (black dashed line), with a mean error of approximately 15 km s^{-1} and a standard deviation of 12 km s^{-1} . A formal fit yields a regression with a slope of 0.994 ± 0.067 (cyan line) reaching an R^2 value of 0.97 at a 95% confidence interval. Similarly, the one-to-one linear fit for Vela-SMGPS and HIZOA heliocentric velocities also exhibits a slope of almost unity (1.002 ± 0.002). We chose to plot their differences, $\Delta v = V_{\text{Vela-SMGPS}} - V_{\text{HIZOA}}$, for a more comprehensive comparison. The results show a mean error of $15 \pm 10 \text{ km s}^{-1}$. Given the coarse SMGPS channel width (44.3 km s^{-1}) and the (smoothed) HIZOA spectral resolution (27 km s^{-1}), this achievement is remarkable, affirming the high quality of the SMGPS calibration and H I parameters.

We furthermore verified the agreement in integrated fluxes, as illustrated in Fig. 12. To derive the integrated flux error ϵ_s , we adopt the method used by [Ramatsoku et al. \(2016\)](#). We selected four emission-free regions located at the corners of the cubelet by dividing each cubelet into a 3×3 grid of the same size as the source mask. ϵ_s is then computed as the mean of the standard deviations

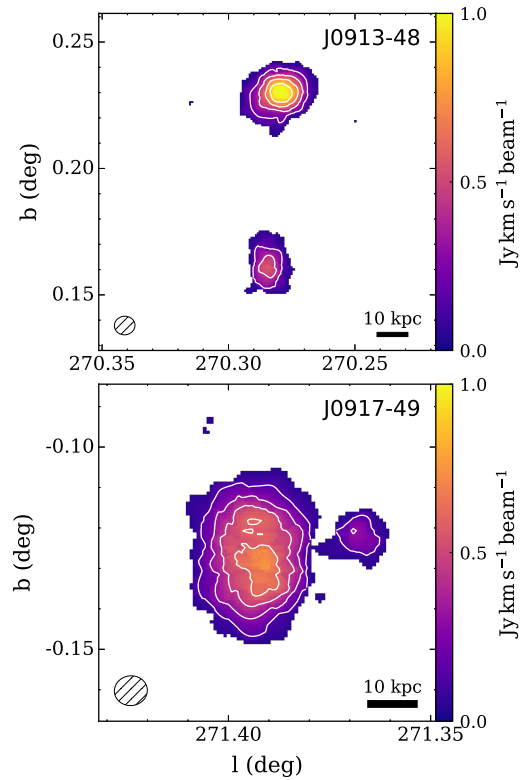


Figure 9. Moment-0 H I emission maps for two HIZOA sources (J0913-48, and J0917-49) reveal them to consist of several counterparts in Vela-SMGPS. A 10 kpc scale bar and the beam size are shown in the right and left bottom corners of each image.

of the measured integrated fluxes within these boxes. We observe typical flux uncertainties of $\sim 32\%$, 19% , 14% , and 10% for H I masses below 10^8 , 10^9 , 10^{10} and above $10^{10} M_{\odot}$, respectively. The measured slope, nearly equal to unity (1.015 ± 0.135), along with $R^2 = 0.89$ at a 95% confidence interval, underlines the consistency between SMGPS and HIZOA flux measurements with less than 2% offset to unity. Overall, the parameters of the comparison sample show excellent agreement with our measurements.

4 RESULTS

The resulting Vela-SMGPS catalog contains 843 H I detections. Across the full velocity range ($V_{\text{hel}} < 25000 \text{ km s}^{-1}$), this corresponds to an average of ~ 9.37 galaxies per deg^2 . Around 93% of the galaxies have no optical or IR counterpart. Apart from the 39 HIZOA galaxies +1 ATCA (massive galaxy), no other redshift measurements exist. Of the 843 detections, 187 galaxies have velocities within $19500 \pm 3500 \text{ km s}^{-1}$ and might be associated with the Vela overdensity. Of these, 76 galaxies lie within the velocity range of $16000 - 19000 \text{ km s}^{-1}$, and 111 galaxies within the $19000 - 23000 \text{ km s}^{-1}$ range, which conform to the two walls of the VSCL. The H I parameters of the 843 H I detections are compiled into a catalog, which is presented in Appendix C as Table C1.

Figure 13 illustrates the wedge diagrams in Galactic longitude and latitude of the Vela-SMGPS detections which demonstrate the impressive sensitivity of this survey. The newly detected H I

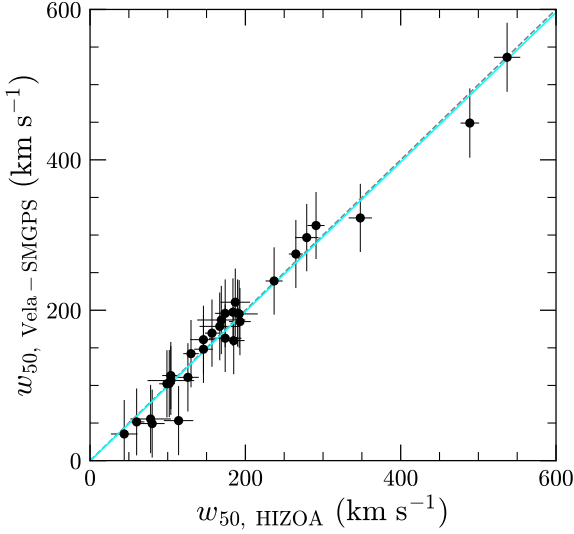


Figure 10. Comparison of H I linewidths w_{50} among the 31 HIZOA detections within the Vela–SMGPS survey. The cyan line represents the best-fit linear regression

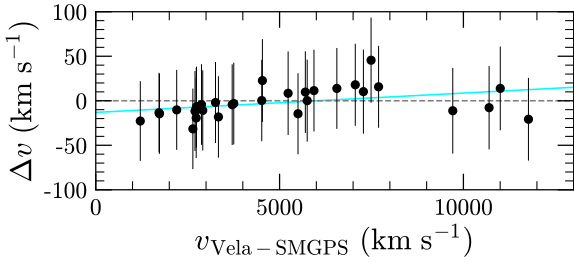


Figure 11. Comparison of Heliocentric Velocities from Vela–SMGPS and the difference $V_{\text{Vela-SMGPS}} - V_{\text{HIZOA}}$.

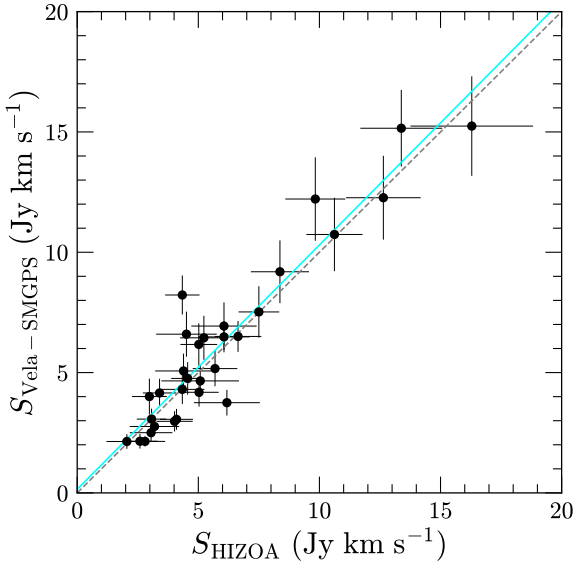


Figure 12. Comparison of the integrated fluxes of 31 galaxies in common with HIZOA. The cyan line illustrates the best-fit linear regression, closely following the one-to-one relation indicated by the grey dashed line.

galaxies are indicated by the light blue dots, and the previously known HIZOA galaxies by red dots. The majority of the galaxies below 4000 km s^{-1} were also found by HIZOA with its sensitivity of 6 mJy beam^{-1} . At higher velocities, the HIZOA dataset predominantly captures the more massive spiral galaxies, but the uncovered structure closely aligns with the general shape (filaments) delineated by Vela–SMGPS. A detailed discussion of the LSS uncovered by Vela–SMGPS will be presented in Section 6.

4.1 Completeness

One way to determine the completeness of a survey involves fitting a power law to the histogram of mean flux density, calculated as the integrated flux divided by the linewidth (cf. Donley et al. 2005; McIntyre et al. 2015; Staveley-Smith et al. 2016). The distribution is expected to follow a Euclidean power law, $N(S) \sim S_{\text{mean}}^{-2.5}$, corresponding to a linear power law with a slope $-3/2$ in log-log space. The completeness threshold becomes apparent when the histogram distribution starts to deviate from this projected line. In Fig. 14, we illustrate solid detections (red), as well as the sample including both solid and possible detections (black). We use w_{50} rather than w_{20} because w_{20} is more influenced by noise variations. The difference in completeness is a mere 0.02 dex in the last bin, indicating that galaxies with S_{mean} exceeding 9.5 and 10 mJy are detected with high completeness in the full and solid samples, respectively. The similarity implies that possible detections are also quite reliable galaxy candidates. We therefore include both solid and possible detections in the further analysis. However, it is important to note that this method works best under the assumption of survey homogeneity and isotropy. A more rigorous completeness test (Rauzy 2001) will be conducted in a forthcoming paper.

4.2 Simulations

For a better interpretation of our results, especially in discerning the presence of overdensity peaks indicative of LSS, we compare our H I data with a simulation. The latter, referred to as S45, utilizes a similar framework as the one discussed in Staveley-Smith & Oosterloo (2015) for the SKA-H I science case. In this approach, constant H I mass and velocity width functions are assumed across redshifts, using the bivariate stepwise maximum likelihood method outlined in Zwaan et al. (2005). The simulation randomly distributes galaxies up to the observations sensitivity threshold (see also Steyn et al. 2024), providing output H I parameters such as peak flux density, integrated fluxes, H I masses, linewidths, and redshifts, without any spatial structure. Here, S45 is tailored to the specifications of the SMGPS, i.e., a sensitivity of $0.45 \text{ mJy beam}^{-1}$ to account for the average noise variation, the coarse channel widths of 44.3 km s^{-1} , and a survey area of 528 deg^2 similar to the full SMGPS survey.

As a result, S45 does not simulate LSS. Instead, it represents a close proxy for a homogeneous distribution. S45 predicts the number of galaxies (with $\text{SNR} > 5$) as a function of redshift, distributed over an area equivalent to the full SMGPS. For the specification of the full SMGPS, it predicts 5591 galaxies in the volume delimited by $V_{\text{hel}} < 25000 \text{ km s}^{-1}$, respectively 953 galaxies for the Vela survey region ($528 \text{ deg}^2/90 \text{ deg}^2$). By comparing it to our observations, we can identify and quantify peaks and gaps indicative of overdensities and underdensities. While LSS in the data can be discerned visually, some structures may result from observational effects. Thus, using S45 enables a clear distinction between real structures and those

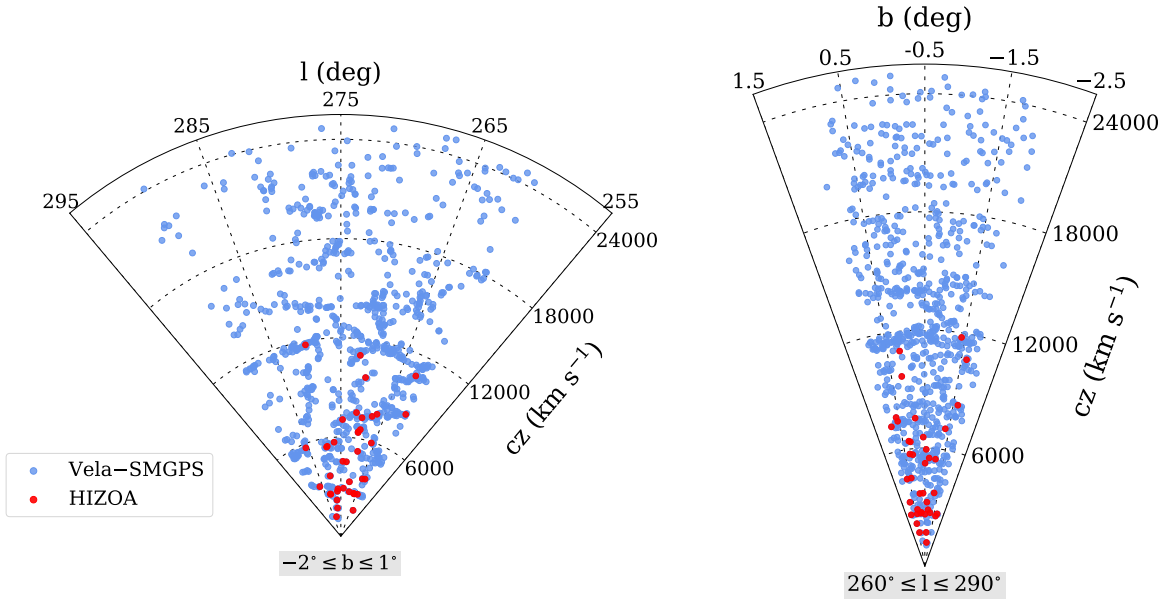


Figure 13. Redshift wedge diagrams illustrating the distribution of H I-detected galaxies up to $V_{\text{hel}} < 25000 \text{ km s}^{-1}$ in Vela-SMGPS (blue dots) and HIZOA (red dots). The left panel depicts a longitude wedge plot covering the latitude range $-2^\circ \leq b \leq 1^\circ$, while the right panel displays a latitude wedge plot spanning the longitude range $260^\circ \leq \ell \leq 290^\circ$.

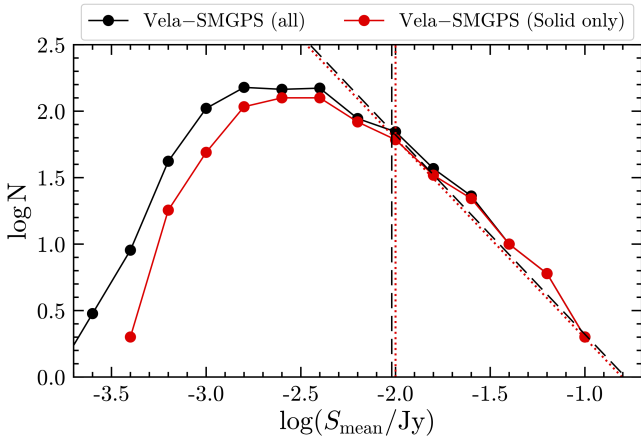


Figure 14. Completeness assessment using a log-log plot of the mean H I flux density $S_{\text{mean}} = (S_{\text{int}}/w_{50})$ for all 843 Vela-SMGPS detections in black and 646 solid detections exclusively in red. The black dashed and red dotted lines correspond to the expected $-3/2$ slope for a homogeneous distribution in both samples.

influenced by selection effects, facilitating a more robust characterization of LSS through its comparison with a homogeneous galaxy distribution (see Section 6.1).

5 VELA-SMGPS H I PROPERTIES DISTRIBUTION

We display the distribution of H I properties for our detections with light-red filled histograms in Figs. 15 and 16. The light blue lines represent the S45 simulations. We appropriately scaled the S45 counts per bin to match the surveyed area. The properties under comparison include velocities (Fig. 15), linewidths, integrated

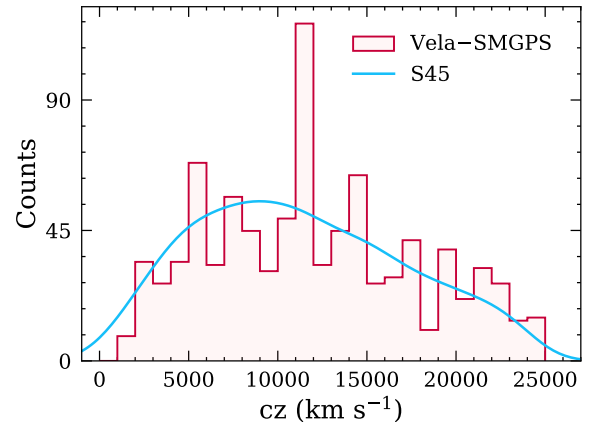


Figure 15. Velocity distribution for the full survey range ($260^\circ \leq \ell \leq 290^\circ$) of Vela-SMGPS detections (light-red histograms). The cyan lines correspond to the S45 simulations (rms $\sim 0.45 \text{ mJy beam}^{-1}$).

fluxes, H I masses, and SNR (Fig. 16).

Velocity distribution. Fig. 15 visually presents an initial view of the overall velocity distribution in the survey area of Vela-SMGPS. The survey counts exhibit a shape quite similar to the simulations, with comparable median velocities: 11592 km s^{-1} (Vela-SMGPS) and 11209 km s^{-1} (S45). However, some peaks stand out, such as a prominent narrow peak around $\sim 12000 \text{ km s}^{-1}$ with roughly 1.85 times higher counts than predicted. This feature is clearly seen as a strong wall-like feature in Fig. 13. Additionally, there is a hint of broader overdensity at the high-velocity end, i.e., $V_{\text{hel}} > 18500 - 23000 \text{ km s}^{-1}$.

w_{50} linewidth distribution. The linewidth histogram for Vela-SMGPS ranges from $12 - 615 \text{ km s}^{-1}$. As expected

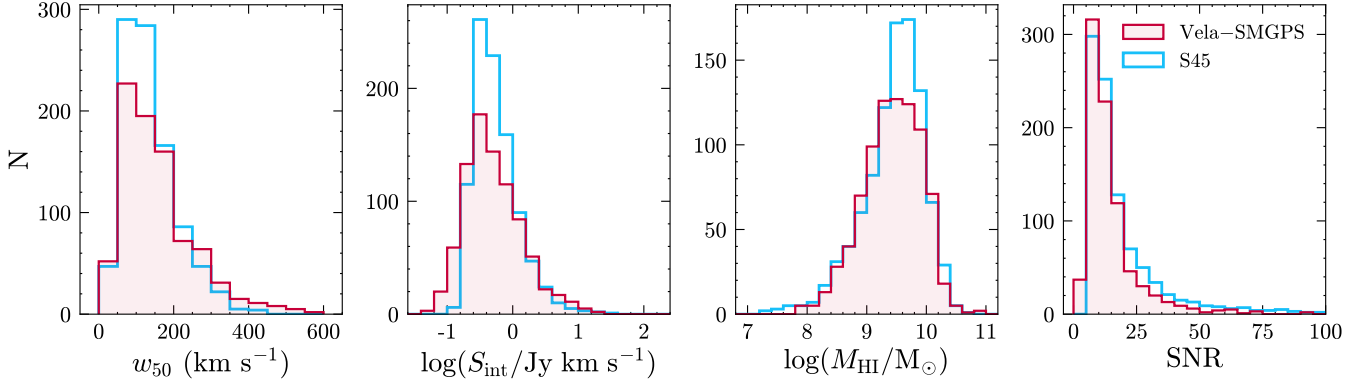


Figure 16. Distribution of global H I parameters in Vela–SMGPS (light-red filled histogram) and S45 simulation (cyan histogram). The four panels display, from left to right, the linewidth (w_{50}) measured at the 50% level of peak flux density, the logarithm of integrated flux (S_{int}), the logarithm of H I mass (M_{HI}), and the integrated signal-to-noise ratio (SNR).

from a systematic blind H I survey (e.g., Haynes et al. 2011; Staveley-Smith et al. 2016), a strong prevalence at low-linewidth galaxies ($w_{50} \sim 50 - 200 \text{ km s}^{-1}$) is observed. This trend is also confirmed by S45. Both distributions exhibit maximum peaks in the $50 - 100 \text{ km s}^{-1}$ bin range. We measure mean values of $158 \pm 99 \text{ km s}^{-1}$ and $137 \pm 71 \text{ km s}^{-1}$ for Vela–SMGPS and S45, respectively. The lower value for S45 reflects its higher proportion of low linewidth galaxies. On the other hand, the distribution in Vela–SMGPS shows more high- w_{50} galaxies. The deviations at the low and high linewidth distributions can be attributed to the inclusion of sources captured with their satellites, which were not spatially resolved in our data cubes. In contrast, S45 exclusively simulated unique galaxies.

Integrated H I flux densities. The second panel illustrates the distribution of the logarithm of the integrated flux. It ranges from a minimal value of $\log(S_{\text{int}}/\text{Jy km s}^{-1}) = -1.37$ ($S_{\text{int}} = 0.04 \text{ Jy km s}^{-1}$) to a maximum of $\log(S_{\text{int}}/\text{Jy km s}^{-1}) = 1.29$ ($S_{\text{int}} = 19.43 \text{ Jy km s}^{-1}$). Vela–SMGPS and S45 both peak at $\log(S_{\text{int}}/\text{Jy km s}^{-1}) \sim -0.5$. S45 presents a slightly higher mean value ($S_{\text{int}} = 0.55 \text{ Jy km s}^{-1}$) compared to Vela–SMGPS with a mean value of $S_{\text{int}} = 0.5 \text{ Jy km s}^{-1}$. This slight difference is attributed to S45 excluding all galaxies with $\text{SNR} < 5$.

H I mass distribution. In both Vela–SMGPS and S45, the galaxies span three orders of magnitude in H I mass, ranging from $10^{7.8} M_{\odot}$ to $10^{10.9} M_{\odot}$ and $10^{7.1} M_{\odot}$ to $10^{10.8} M_{\odot}$ respectively. Apart from the more pronounced peaks at $\log(M_{\text{HI}}/M_{\odot}) \sim 9.5$ in Vela–SMGPS and 9.7 in S45, the overall distributions are very similar. Their mean H I masses only differ by approximately 3% with S45 being slightly higher. We find an average H I mass of $10^{9.43} M_{\odot}$ and $10^{9.44} M_{\odot}$ for Vela–SMGPS and S45, respectively. These values are comparable to the measurement of the H I mass of the Milky Way (see e.g., Nakanishi & Sofue 2003).

Integrated signal-to-noise ratio. In the rightmost panel, we compare the integrated signal-to-noise ratio between the simulation and the H I detections from our survey, calculated using Eq. 9. Both distributions exhibit striking similarity, with a peak occurring at $\sim 7\sigma$. As the SNR decreases, the number of detections increases steeply.

In Fig. 17 we compare the distribution of the individual detections

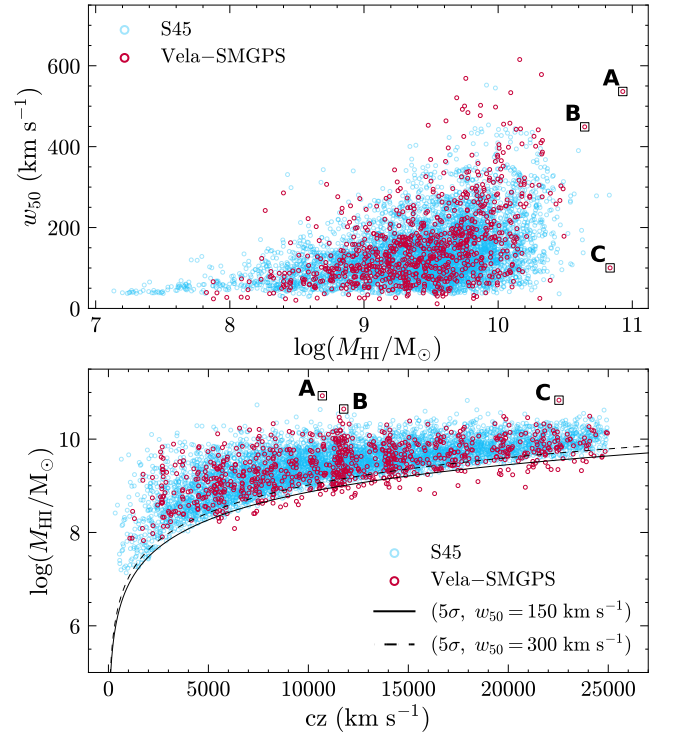


Figure 17. Dependence of H I linewidth w_{50} as a function of H I mass (top panel) and H I mass versus velocity (bottom panel). Vela–SMGPS detections (red dots) are overlaid on simulated S45 galaxies (cyan dots). The solid and dashed black lines represent sensitivity curves for the 5σ H I mass detection level, assuming w_{50} values of 150 and 300 km s^{-1} , with $\sigma = 0.45 \text{ mJy beam}^{-1}$. SMGPS-HI J083650-433738 (A), J095513-561846 (B), and J084731-432134 (C) are marked inside black squares.

in Vela–SMGPS (red dots) in $w_{50} - \log M_{\text{HI}}$ and $\log M_{\text{HI}} - V_{\text{hel}}$ plots. We again add simulations to provide an idea about the expected distribution. The resulting distributions suggest that both the simulations and Vela–SMGPS sample the same population. Vela–SMGPS detects a slightly larger fraction of galaxies toward the high-mass end. We mark three galaxies seen as outliers in the figure due to their large H I masses. The first one, SMGPS-HI J083650-433738 (marked as galaxy A), with $w_{50} = 536 \text{ km s}^{-1}$ and $M_{\text{HI}} = 10^{10.93} M_{\odot}$, is the most H I-massive spiral recovered in HIPASS/HIZOA J0836-43, discussed earlier in Section 3.4.2. J095513-561846 (B) or HI-

ZOA J0955-56, another broad linewidth galaxy with $w_{50} = 449$ km s^{-1} and $M_{\text{HI}} = 10^{10.65} M_{\odot}$. Another massive spiral galaxy, with a lower linewidth, J084731-432134 (C, $w_{50} = 100$ km s^{-1} , $M_{\text{HI}} = 10^{10.83} M_{\odot}$), was also detected as an outlier in Fig. 17 at $V_{\text{hel}} \sim 22500$ km s^{-1} . It resembles a large face-on galaxy when examined in the Galaxy Atlas.

The bottom panel of Fig. 17 shows the so-called sensitivity curve displaying $\log M_{\text{HI}}$ vs. velocity. The black solid and dashed lines represent the 5σ detection limit for galaxies with 150 km s^{-1} and 300 km s^{-1} linewidth as a function of redshift, respectively. First, Vela–SMGPS only found galaxies with masses $\log(M_{\text{HI}}/M_{\odot}) > 7.8$, whereas the simulation identifies galaxies below that threshold. This discrepancy may be attributed to the lower number of low linewidth galaxies (50 to 150 km s^{-1}) detected in Vela–SMGPS compared to S45 (see the left panel in Fig. 16). It could also be due to the coarse channel width or even LSS because we did not detect galaxies in the volume below $cz \leq 800$ km s^{-1} . Second, the distributions of detections and simulations both show that we are sensitive to normal spirals ($w_{50} \sim 200$ km s^{-1}) with $5\sigma \log(M_{\text{HI}}/M_{\odot}) \geq 9.5$ at the VSCL distance of $V_{\text{hel}} = 18000$ km s^{-1} , and $5\sigma \log(M_{\text{HI}}/M_{\odot}) \geq 9.7$ out to the surveyed redshift limit of $V_{\text{hel}} = 25000$ km s^{-1} . This demonstrates that we are sensitive to galaxies below M_{HI}^* at the VSCL distance.

The figure also highlights various signatures of LSS in its distribution. These high degrees of clustering seem to occur at various scales and are closely aligned to the hint of peak overdensities observed in the velocity distribution presented earlier in Fig 15. Four prominent clumps around 3000 km s^{-1} , 5000 – 6000 km s^{-1} , 11000 – 12000 km s^{-1} , and ~ 14000 km s^{-1} are observed. Notably, the clump at 11000 – 12000 km s^{-1} exhibits an elongated distribution along the HI mass. To examine this more closely, we will, in the next sections, divide the survey into different longitude ranges, and wedge diagrams, for a further analysis of the uncovered LSS.

6 LARGE SCALE STRUCTURES ANALYSIS

In this section, we will first inspect the velocity distribution of the survey detections in comparison to the simulation to assess peak overdensities, giving particular emphasis to areas where the VSCL walls are predicted to intersect. Subsequently, we examine the distribution of Vela–SMGPS galaxies in the inner ZOA to pinpoint these overdensities and assess their significance on on-sky plots and redshift slice diagrams.

6.1 LSS in Velocity Space

In Section 5, we showed the overall velocity distribution of Vela–SMGPS (see Fig. 15) with potential peak overdensities. To localize these peaks and set a better understanding of these potential filaments and/or walls, we divide the survey area into different subregions with a longitude interval of $\Delta\ell = 10^\circ$ (see Fig. 18).

The first panel of Fig. 18 spans the range $280^\circ \leq \ell \leq 290^\circ$. We observe a subtle enhancement at 2000 – 4000 km s^{-1} and a more pronounced peak at 5000 – 6000 km s^{-1} , also notable in Fig. 17. These hints are suggestive of links with the Hydra/Antlia wall (Kraan-Korteweg et al. 1995) and AS639 cluster (Stein 1996), respectively (see Section 6.2 for further details). Most prominent is the significant peak at ~ 12000 km s^{-1} which is also present in the other subregions. Its visibility is particularly pronounced in this first panel, with a factor of ~ 2 higher than predicted counts. It is also quite conspicuous in the mass-redshift space (see bottom panel of Fig. 17). The peak appears

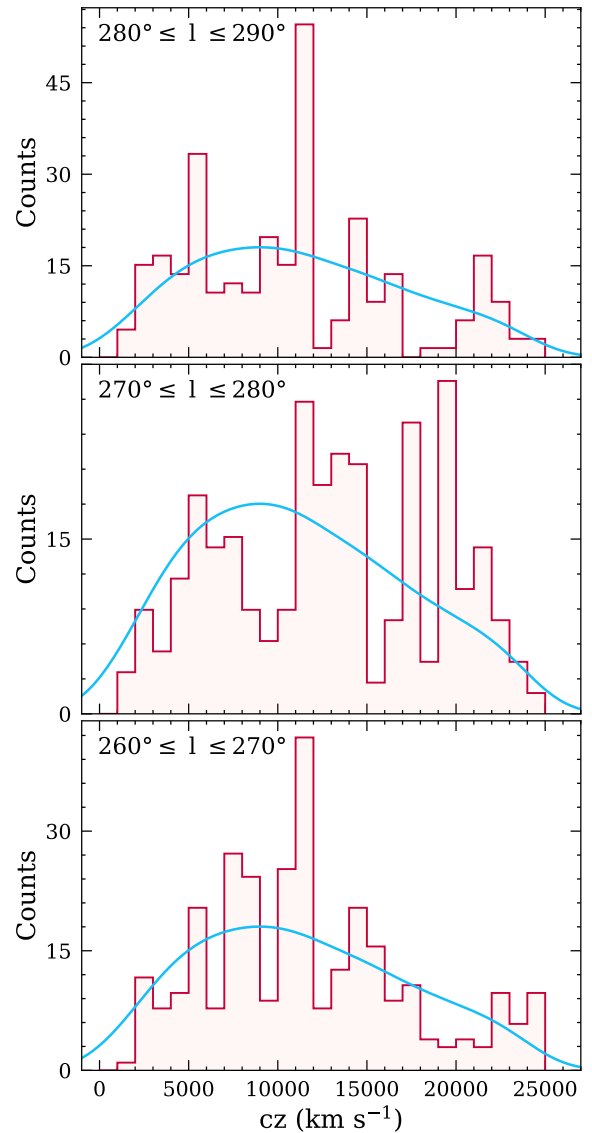


Figure 18. Velocity distribution histograms similar to Fig. 15, where the three different panels subsample distinct longitude ranges: $280^\circ \leq \ell \leq 290^\circ$, $270^\circ \leq \ell \leq 280^\circ$, and $260^\circ \leq \ell \leq 270^\circ$.

to be due to a narrow but very extended filament aligned along the survey’s length in both longitude and latitude (see also Section 5).

The second panel covers the longitude range of $270^\circ \leq \ell \leq 280^\circ$. We see distinct features corresponding to higher redshift structures in Vela–SMGPS. This includes the significant clump observed at velocities of 14000 – 16000 km s^{-1} in Fig. 17, which is also visible in the other panels at velocities of 14000 – 15000 km s^{-1} . Furthermore, two additional prominent peaks related to the VSCL ($V_{\text{hel}} > 16000$ km s^{-1}) stand out over the predicted counts from S45. The counts are roughly 2.8 times higher than expected for the velocity range of 17000 – 18000 km s^{-1} , and nearly 3.6 times higher for the range of 19000 – 20000 km s^{-1} . This closely matches the longitude range (270° – 280°) of the first Wall (W1) in VSCL, found from optical spectroscopy at latitudes $|b| \gtrsim 7^\circ$ (KK2017). There is a hint of the second higher redshift Wall (W2) visible around 21000 – 22000 km s^{-1} . The second Wall is, however, quite prominent in the last panel, $260^\circ \leq \ell \leq 270^\circ$, with counts that are roughly 2.5 times higher than those in the simulations.

6.2 LSS crossing the ZOA

We now look at the on-sky distributions of the newly discovered galaxies in a sequence of velocity intervals and discuss the unveiled LSS in connection to known LSS above and below the ZOA. Figures 19a and 19b present a total of five on-sky (2D) distributions, each spanning a velocity range of $\Delta v = 4500 \text{ km s}^{-1}$. The recently identified HI galaxies are located within black dashed boxes which demarcate the survey area of Vela–SMGPS. Symbolized by cyan, green, and blue, each 1500 km s^{-1} bin represents the closest to the highest velocity bin within the respective panel. Grey contour lines, representing DIRBE/IRAS extinction contours (Schlegel et al. 1998; Schlafly & Finkbeiner 2011) at $A_B = 3^{m0}$, highlight regions where the ZOA is opaque to optical galaxies (e.g., Woudt & Kraan-Korteweg 2001). We display redshift wedges alongside the on-sky plots since galaxies that appear spatially aligned in the sky might not share the same alignment in redshift space. An investigation of both displays simultaneously allows a comprehensive examination of the galaxy clustering and density peaks seen in Figs. 17 and 18.

We will start from the nearest velocity bin in Fig. 19a:

($2000 < V_{\text{hel}} < 6500 \text{ km s}^{-1}$): a noticeable concentration of cyan dots ($2000 - 3500 \text{ km s}^{-1}$) is centered around $\ell \sim 280^\circ \pm 4^\circ$, $b \sim 0^\circ$ (see red circle). An alignment of blue points at $\sim 3000 \text{ km s}^{-1}$ in the wedge diagram provides further support. This could be the signature associated with the filamentary structure known as the Hydra/Antlia extension (Kraan-Korteweg et al. 1995; Kraan-Korteweg 2000), which crosses the ZOA at these coordinates.

The upper right panel of the on-sky plot ($6500 < V_{\text{hel}} < 11000 \text{ km s}^{-1}$) exhibits fewer pronounced features. Nevertheless, we observe a filament from $260^\circ \leq \ell \leq 277^\circ$ in the wedge diagram, which appears as a peak overdensity at $7000 - 9000 \text{ km s}^{-1}$ in the last panel of Fig. 18. This structure may be linked to the cluster AS639 ($280^\circ, +6^\circ, 6000 \text{ km s}^{-1}$; Stein 1996).

In the bottom left panel ($11000 < V_{\text{hel}} < 15500 \text{ km s}^{-1}$), the distribution of galaxies in the velocity range of $11000 - 12500 \text{ km s}^{-1}$ (cyan dots) is most remarkable. It spans the entire longitude range of $\Delta \ell = 30^\circ$ within the survey area as seen in a highly significant peak present in all the panels of Fig. 18. The on-sky plot and wedge unveil a narrow filament at constant velocity, estimated to have a width of $\sim 500 \text{ km s}^{-1}$ ($\sim 7 \text{ Mpc}$) and an approximate length of 90 Mpc at $\sim 12000 \text{ km s}^{-1}$. Upon closer examination of the wedge slice, it looks like this structure could potentially consist of two intersecting filaments, possibly crossing between $270^\circ \leq \ell \leq 280^\circ$. This observation is strengthened when looking at the on-sky plot displayed in the bottom left panel of Fig. 19a, which shows Vela–SMGPS in context with known LSS data from the literature in the surrounding area ($245^\circ < \ell < 305^\circ$, $|b| < 25^\circ$). These include data from HyperLEDA (Paturel et al. 2003), 2MRS (Huchra et al. 2012; Macri et al. 2019), combined with unpublished redshift data from AAOmega+2dF, SALT, OPTOPUS, and 6dF in the Hydra/Antlia region (Kraan-Korteweg, priv. comm). One of the filaments is suggested to cross the GP around $275^\circ \leq \ell \leq 280^\circ$ (indicated by the clustering of green dots inside the red circle), continuing toward positive latitudes above the GP and slightly higher redshifts (blue dots).

We now turn our attention to the structures at the highest velocity intervals ($15500 < V_{\text{hel}} < 24500 \text{ km s}^{-1}$), illustrated in Fig. 19b. This specific redshift incorporates the volume of the Vela Supercluster ($\ell = 272.5^\circ \pm 20^\circ$, $b = 0^\circ \pm 10^\circ$, $19500 \pm 3500 \text{ km s}^{-1}$, KK2017).

In the upper left panel ($15500 < V_{\text{hel}} < 20000 \text{ km s}^{-1}$), a distinct

clustering of green dots ($17000 - 18500 \text{ km s}^{-1}$) is observed, concentrated primarily around $\ell \sim 270^\circ - 277^\circ$ (light green rectangle). This marks the identified main VSCL Wall (W1). Additionally, a segment of the second Wall (W2) at higher velocities (blue dots at $18500 - 20000 \text{ km s}^{-1}$) is noted in a similar region ($\ell \sim 272^\circ - 280^\circ$, indicated by the blue rectangle), with a higher density peak towards $\ell \sim 277^\circ$. These clusterings are seen as density peaks when compared to simulations in the second panel of Fig. 18.

As we transition to the lower left panel ($20000 < V_{\text{hel}} < 24500 \text{ km s}^{-1}$) to investigate W2, around 22000 km s^{-1} , a consistent pattern emerges. The clustering of points, although more diffuse, indicates the presence of a broader and less compact wall. The cyan and green dots converge around $\ell \sim 272^\circ - 278^\circ$, and $V_{\text{hel}} \sim 20000 - 23000 \text{ km s}^{-1}$ (marked by the intersection of the cyan and green rectangles). This coincides with the smaller peaks in the last two panels of Fig. 18, less notable compared to W1. Interestingly, the representation of the walls in the wedge plot (see red arrows) strikingly mirrors the structures identified on both sides of the ZOA as seen in Fig. 3 of the VSCL discovery paper (KK2017).

As a result, despite only capturing a portion of VSCL due to the limited HI mass sensitivity of $\log(M_{\text{HI}}/M_\odot) \sim 9.5$ at the VSCL distance, our findings are in support of the existence of clear overdensities associated with the surmised walls of the VSCL, W1 at $\sim 18500 \text{ km s}^{-1}$ and W2 at $\sim 21500 \text{ km s}^{-1}$, and point in the approximate direction of the core of a substantial overdensity as derived from independent reconstructions (Sorice et al. 2017; Courtois et al. 2019). These structures seem to cross in the inner ZOA around $272^\circ \leq \ell \leq 278^\circ$ (see orange circle in the wedge), thus reinforcing the findings presented by KK2017.

Even with the addition of new SMGPS data, the paucity of data at intermediate latitudes ($1.5^\circ \leq |b| \leq 7^\circ$) remains prominent in the on-sky plots, which makes it difficult to visualize the morphology of the walls and any potential merging process in detail. The forthcoming MeerKAT Vela–HI survey (Rajohnson et al., in prep) will present newly obtained HI data similar to the SMGPS. It will bridge the gap between the SMGPS and the optical spectroscopic data ($1.5^\circ \leq |b| \leq 7^\circ$) in the VSCL region. These will allow an expanded discussion into how these peaks of overdensity in the inner ZOA from Vela–SMGPS connect with known LSS at much higher latitudes above $|b| \gtrsim 7^\circ$.

7 CONCLUSIONS

This paper presents the HI data extracted from the SARAO MeerKAT Galactic Plane Survey, centered on the Vela region (Vela–SMGPS; $260^\circ \leq \ell \leq 290^\circ$, $-2^\circ \leq b \leq 1^\circ$). With a velocity coverage reaching out to $V_{\text{hel}} \sim 25000 \text{ km s}^{-1}$, and a sensitivity of $\sim 0.39 \text{ mJy beam}^{-1}$, we have successfully cataloged galaxies along a narrow 3° strip covering the most opaque part of the ZOA. Using SoFia in conjunction with a visual verification process, we identified 843 HI galaxies across the 10 contiguous mosaics covering the survey area. Among them, only 39 possessed ancillary redshift information for independent comparison, having previously been detected by the HIZOA survey. Six of these sources were found to consist of two or more counterparts (illustrated in Fig. B2). Notably, Vela–SMGPS successfully recovered the most HI-massive spiral, HIZOA J0836-43, exhibiting consistent measurements with ATCA and HIZOA. The HI properties of the galaxies in common are also in excellent agreement and exhibit a linear relation, consistent – within the errors – with a

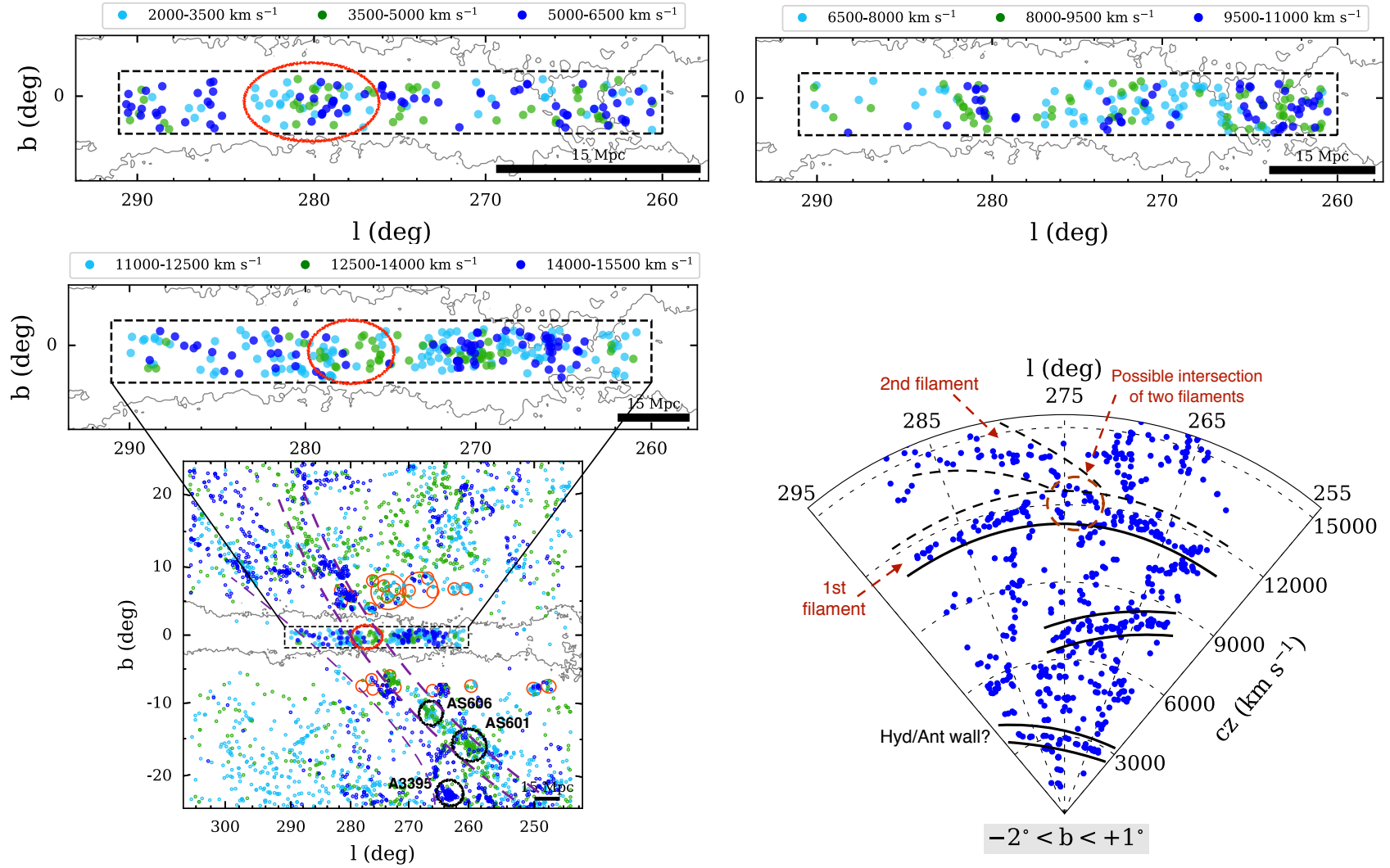


Figure 19a. On-sky distributions of galaxies in the Vela–SMGPS survey, divided into three redshift intervals within the nearby velocity range $2000 < V_{\text{hel}} < 15500 \text{ km s}^{-1}$. Each panel spans $\Delta v = 4500 \text{ km s}^{-1}$, with cyan, green, and blue indicating velocity bins increasing in steps of 1500 km s^{-1} . The black dashed box highlights the newly detected H I galaxies. The bottom left panel (velocity interval $11000 - 15500 \text{ km s}^{-1}$) is accompanied by the on-sky plot of its surrounding area ($245^\circ < \ell < 305^\circ$, $|b| < 25^\circ$), and includes ancillary data with known redshifts from HyperLEDA, 2MRS, and KK2017. The latter is shown inside the orange open circles. Grey contour outlines dust extinction based on DIRBE maps (Schlegel et al. 1998; Schlafly & Finkbeiner 2011) at $A_B = 3^{\text{m}0}$. Each on-sky plot has a 15 Mpc scale bar at its bottom right corner. An accompanying wedge diagram limited to $V_{\text{hel}} < 15500 \text{ km s}^{-1}$ is displayed in the bottom right panel.

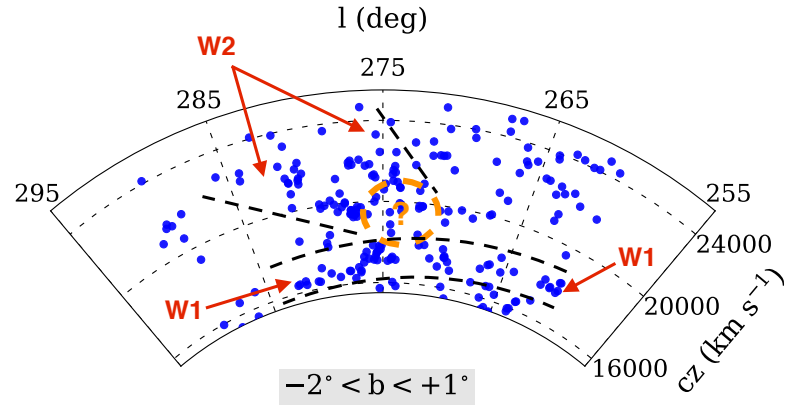
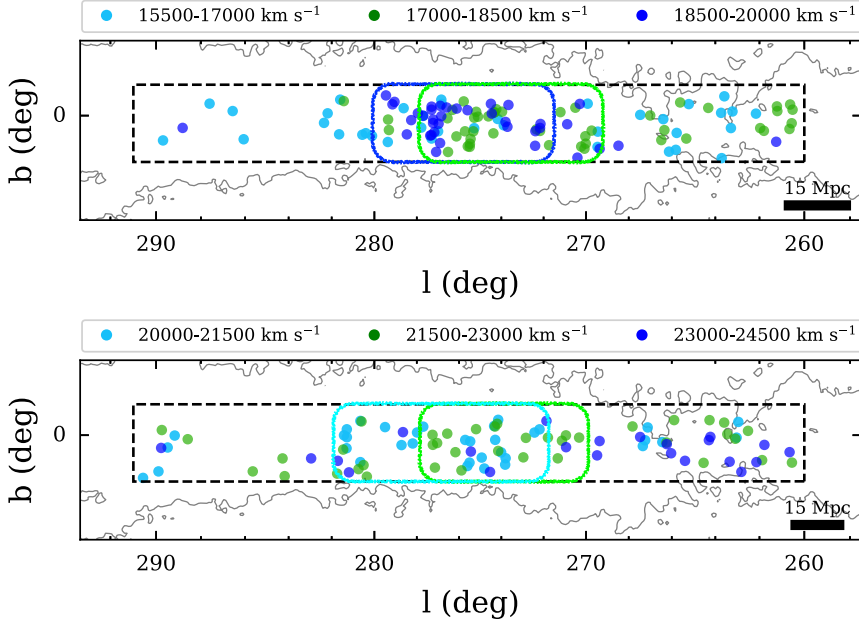


Figure 19b. Continuing from Fig. 19a, this figure presents two velocity bins with $\Delta v = 4500 \text{ km s}^{-1}$ in the left panels, covering the higher redshift range ($V_{\text{hel}} > 15500 \text{ km s}^{-1}$). The right panel features a wedge diagram within $15500 < V_{\text{hel}} < 24500 \text{ km s}^{-1}$.

- Daza-Perilla I. V., et al., 2023, *MNRAS*, **524**, 678
- Donley J. L., et al., 2005, *AJ*, **129**, 220
- Donley J. L., Koribalski B. S., Staveley-Smith L., Kraan-Korteweg R. C., Schröder A., Henning P. A., 2006, *MNRAS*, **369**, 1741
- Erdođdu P., et al., 2006a, *MNRAS*, **368**, 1515
- Erdođdu P., et al., 2006b, *MNRAS*, **373**, 45
- Falco E. E., et al., 1999, *PASP*, **111**, 438
- Feldman H. A., Watkins R., Hudson M. J., 2010, *MNRAS*, **407**, 2328
- For B. Q., et al., 2021, *MNRAS*, **507**, 2300
- Goedhart S., et al., 2023, *arXiv e-prints*, p. [arXiv:2312.07275](https://arxiv.org/abs/2312.07275)
- Hasegawa T., et al., 2000, *MNRAS*, **316**, 326
- Haynes M. P., et al., 2011, *AJ*, **142**, 170
- Helou G., Walker D. W., 1988, in *Infrared astronomical satellite (IRAS) catalogs and atlases. Volume 7*.
- Hinshaw G., et al., 2013, *ApJS*, **208**, 19
- Hoffman Y., Courtois H. M., Tully R. B., 2015, *MNRAS*, **449**, 4494
- Hoffman Y., Pomarède D., Tully R. B., Courtois H. M., 2017, *Nature Astronomy*, **1**, 0036
- Hong T., et al., 2014, *MNRAS*, **445**, 402
- Hong T., et al., 2019, *MNRAS*, **487**, 2016
- Howlett C., Said K., Lucey J. R., Colless M., Qin F., Lai Y., Tully R. B., Davis T. M., 2022, *MNRAS*, **515**, 953
- Huchra J., Davis M., Latham D., Tonry J., 1983, *ApJS*, **52**, 89
- Huchra J. P., et al., 2012, *ApJS*, **199**, 26
- Hudson M. J., Smith R. J., Lucey J. R., Branchini E., 2004, *MNRAS*, **352**, 61
- Jarrett T. H., Chester T., Cutri R., Schneider S., Skrutskie M., Huchra J. P., 2000, *AJ*, **119**, 2498
- Jones D. H., et al., 2009, *MNRAS*, **399**, 683
- Józsa G. I. G., et al., 2020, CARACal: Containerized Automated Radio Astronomy Calibration pipeline (ascl:2006.014)
- Kenyon J. S., Smirnov O. M., Grobler T. L., Perkins S. J., 2018, *MNRAS*, **478**, 2399
- Kourkchi E., et al., 2020, *ApJ*, **902**, 145
- Kraan-Korteweg R. C., 2000, *A&AS*, **141**, 123
- Kraan-Korteweg R. C., 2005, *Reviews in Modern Astronomy*, **18**, 48
- Kraan-Korteweg R. C., Lahav O., 2000, *A&A Rev.*, **10**, 211
- Kraan-Korteweg R. C., Fairall A. P., Balkowski C., 1995, *A&A*, **297**, 617
- Kraan-Korteweg R. C., Staveley-Smith L., Donley J., Koribalski B., Henning P. A., 2005, in Colless M., Staveley-Smith L., Stathakis R. A., eds, *IAU Symposium No. 216 Vol. 216, Maps of the Cosmos*. Astron. Soc. Pac., San Francisco. p. 203, doi:[10.1017/S0074180900196640](https://doi.org/10.1017/S0074180900196640)
- Kraan-Korteweg R. C., Cluver M. E., Bilicki M., Jarrett T. H., Colless M., Elagali A., Böhringer H., Chon G., 2017, *MNRAS*, **466**, L29
- Kurapati S., et al., 2024, *MNRAS*, **528**, 542
- Lahav O., Yamada T., Scharf C., Kraan-Korteweg R. C., 1993, *MNRAS*, **262**, 711
- Lauer T. R., Postman M., 1994, *ApJ*, **425**, 418
- Lavaux G., Tully R. B., Mohayaee R., Colombi S., 2010, *ApJ*, **709**, 483
- Loeb A., Narayan R., 2008, *MNRAS*, **386**, 2221
- Macri L. M., et al., 2019, *ApJS*, **245**, 6
- Makhathini S., 2018, PhD thesis, Rhodes University, South Africa
- Masters K. L., Springob C. M., Haynes M. P., Giovanelli R., 2006, *ApJ*, **653**, 861
- Masters K. L., et al., 2007, in *American Astronomical Society Meeting Abstracts #210*. p. 84.03
- Mauch T., et al., 2020, *ApJ*, **888**, 61
- McIntyre T. P., Henning P. A., Minchin R. F., Momjian E., Butcher Z., 2015, *AJ*, **150**, 28
- Meyer M. J., et al., 2004, *MNRAS*, **350**, 1195
- Meyer M., Robotham A., Obreschkow D., Westmeier T., Duffy A. R., Staveley-Smith L., 2017, *PASA*, **34**, 52
- Nakanishi H., Sofue Y., 2003, *PASJ*, **55**, 191
- Offringa A. R., 2010, AOFlogger: RFI Software (ascl:1010.017)
- Offringa A. R., et al., 2014, *MNRAS*, **444**, 606
- Patuel G., Petit C., Prugniel P., Theureau G., Rousseau J., Brouty M., Dubois P., Cambrésy L., 2003, *A&A*, **412**, 45
- Peebles P. J. E., 1976, *ApJ*, **205**, 318
- Planck Collaboration et al., 2020, *A&A*, **641**, A1
- Proctor R., 1878, *The Universe of Stars: Presenting Researches Into and New Views Respecting the Constitution of the Heavens*. Longmans, Green, and Company, <https://books.google.co.za/books?id=85DvAAAAAAAJ>
- Qin F., 2021, *Research in Astronomy and Astrophysics*, **21**, 242
- Qin F., Howlett C., Staveley-Smith L., Hong T., 2018, *MNRAS*, **477**, 5150
- Qin F., Howlett C., Staveley-Smith L., Hong T., 2019, *MNRAS*, **482**, 1920
- Rajohnson S. H. A., et al., 2022, *MNRAS*, **512**, 2697
- Ramatsoku M., et al., 2016, *MNRAS*, **460**, 923
- Rauzy S., 2001, *MNRAS*, **324**, 51
- Rivers A. J., Henning P. A., Kraan-Korteweg R. C., 1999, *PASA*, **16**, 48
- Said K., Kraan-Korteweg R. C., Jarrett T. H., Staveley-Smith L., Williams W. L., 2016, *MNRAS*, **462**, 3386
- Schlafly E. F., Finkbeiner D. P., 2011, *ApJ*, **737**, 103
- Schlegel D. J., Finkbeiner D. P., Davis M., 1998, *ApJ*, **500**, 525
- Scrimgeour M. I., et al., 2016, *MNRAS*, **455**, 386
- Serra P., Jurek R., Flöer L., 2012, *PASA*, **29**, 296–300
- Shapley H., 1961, *Galaxies*.
- Sorce J. G., Colless M., Kraan-Korteweg R. C., Gottlöber S., 2017, *MNRAS*, **471**, 3087
- Springob C. M., Haynes M. P., Giovanelli R., Kent B. R., 2005, *ApJS*, **160**, 149
- Springob C. M., Masters K. L., Haynes M. P., Giovanelli R., Marinoni C., 2007, *ApJS*, **172**, 599
- Springob C. M., et al., 2014, *MNRAS*, **445**, 2677
- Springob C. M., et al., 2016, *MNRAS*, **456**, 1886
- Staveley-Smith L., Oosterloo T., 2015, in *Advancing Astrophysics with the Square Kilometre Array (AASKA14)*. p. 167 ([arXiv:1506.04473](https://arxiv.org/abs/1506.04473))
- Staveley-Smith L., Kraan-Korteweg R. C., Schröder A. C., Henning P. A., Koribalski B. S., Stewart I. M., Heald G., 2016, *AJ*, **151**, 52
- Stein P., 1996, *A&AS*, **116**, 203
- Steyn N., 2023, First MeerKAT H I survey results mapping large scale structures hidden behind the Milky Way out to $z = 0.08$, <http://hdl.handle.net/11427/38045>
- Steyn N., et al., 2024, *MNRAS*, **529**, L88
- Strauss M. A., Willick J. A., 1995, *Phys. Rep.*, **261**, 271
- Tempel E., Stoica R. S., Martínez V. J., Liivamägi L. J., Castellan G., Saar E., 2014, *MNRAS*, **438**, 3465
- Tully R. B., Courtois H. M., Sorce J. G., 2016, *AJ*, **152**, 50
- Tully R. B., et al., 2023, *ApJ*, **944**, 94
- Turnbull S. J., Hudson M. J., Feldman H. A., Hicken M., Kirshner R. P., Watkins R., 2012, *MNRAS*, **420**, 447
- Wakamatsu K., Malkan M. A., Nishida M. T., Parker Q. A., Saunders W., Watson F. G., 2005, in Fairall A. P., Woudt P. A., eds, *Astronomical Society of the Pacific Conference Series Vol. 329, Nearby Large-Scale Structures and the Zone of Avoidance*. p. 189
- Watkins R., Feldman H. A., Hudson M. J., 2009, *MNRAS*, **392**, 743
- Westmeier T., et al., 2021, *MNRAS*, **506**, 3962
- Williams W. L., Kraan-Korteweg R. C., Woudt P. A., 2014, *MNRAS*, **443**, 41
- Woudt P. A., 1998, PhD thesis, University of Cape Town, South Africa
- Woudt P. A., Kraan-Korteweg R. C., 2001, *A&A*, **380**, 441
- Wright E. L., et al., 2010, *AJ*, **140**, 1868
- Zwaan M. A., Meyer M. J., Staveley-Smith L., Webster R. L., 2005, *MNRAS*, **359**, L30
- da Costa L. N., et al., 1998, *AJ*, **116**, 1

APPENDIX A: SOFIA-2 PARAMETER FILE

The appendix below provides the parameter file employed in SoFiA 2.3.1, using the smooth + clip (S + C) finder with a 4σ noise threshold. The same parameter configuration is utilized for the second SoFiA run but with the adjustment `scfind.threshold = 3.5`.

```
# Global settings

pipeline.verbose      = false
pipeline.pedantic    = false

# Input

input.data            = Taper15_T30/to_galactic/T30_gal-taper15.fits
input.region          = 1268, 5470, 355, 3958, 9, 525
input.gain            =
input.noise           = Taper15_T30/to_galactic/T30_gal-taper15_noise.fits
input.weights        =
input.mask            =
input.invert          = false

# Flagging

flag.region          =
flag.auto            = false
flag.threshold       = 5.0
flag.log             = true

# Noise scaling

scaleNoise.enable    = true
scaleNoise.mode      = local
scaleNoise.statistic = mad
scaleNoise.windowXY  = 301
scaleNoise.windowZ   = 15
scaleNoise.gridXY    = 0
scaleNoise.gridZ     = 0
scaleNoise.interpolate = true
scaleNoise.scfind    = false

# S+C finder (smooth & clip)

scfind.enable        = true
scfind.kernelsXY     = 0, 7, 15
scfind.kernelsZ      = 0, 3, 5, 7
scfind.threshold     = 4 #and 3.5
scfind.replacement   = 1.5
scfind.statistic     = mad
scfind.fluxRange     = negative

# Linker

linker.radiusXY      = 5
linker.radiusZ       = 3
linker.minSizeXY     = 10
linker.minSizeZ      = 3
linker.maxSizeXY     = 0
linker.maxSizeZ      = 50

# Reliability

reliability.enable   = true
reliability.threshold = 0.90
reliability.scaleKernel = 0.25
reliability.minSNR   = 3
reliability.plot     = true
reliability.debug    = true

# Parameterisation

parameter.enable     = true
parameter.wcs        = true
parameter.physical   = true
parameter.prefix     = SoFiA
parameter.offset     = true

# Output

output.directory     = Taper15_T30/sofia_new/local/4_sigma
output.filename      = T30_gal_local_4_sigma_
output.writeCatASCII = true
output.writeCatXML   = false
output.writeCatSQL   = false

output.writeNoise    = false
output.writeFiltered = false
output.writeMask     = true
output.writeMask2d   = false
output.writeMoments  = false
output.writeCubelets = false
output.marginCubelets = 0
output.override      = true
```


APPENDIX B: HIZOA DETECTIONS IN VELA–SMGPS

The 39 Vela–SMGPS detections in common with HIZOA (Staveley-Smith et al. 2016) are shown in Fig. B1 (unique) and B2 (multiple counterparts).

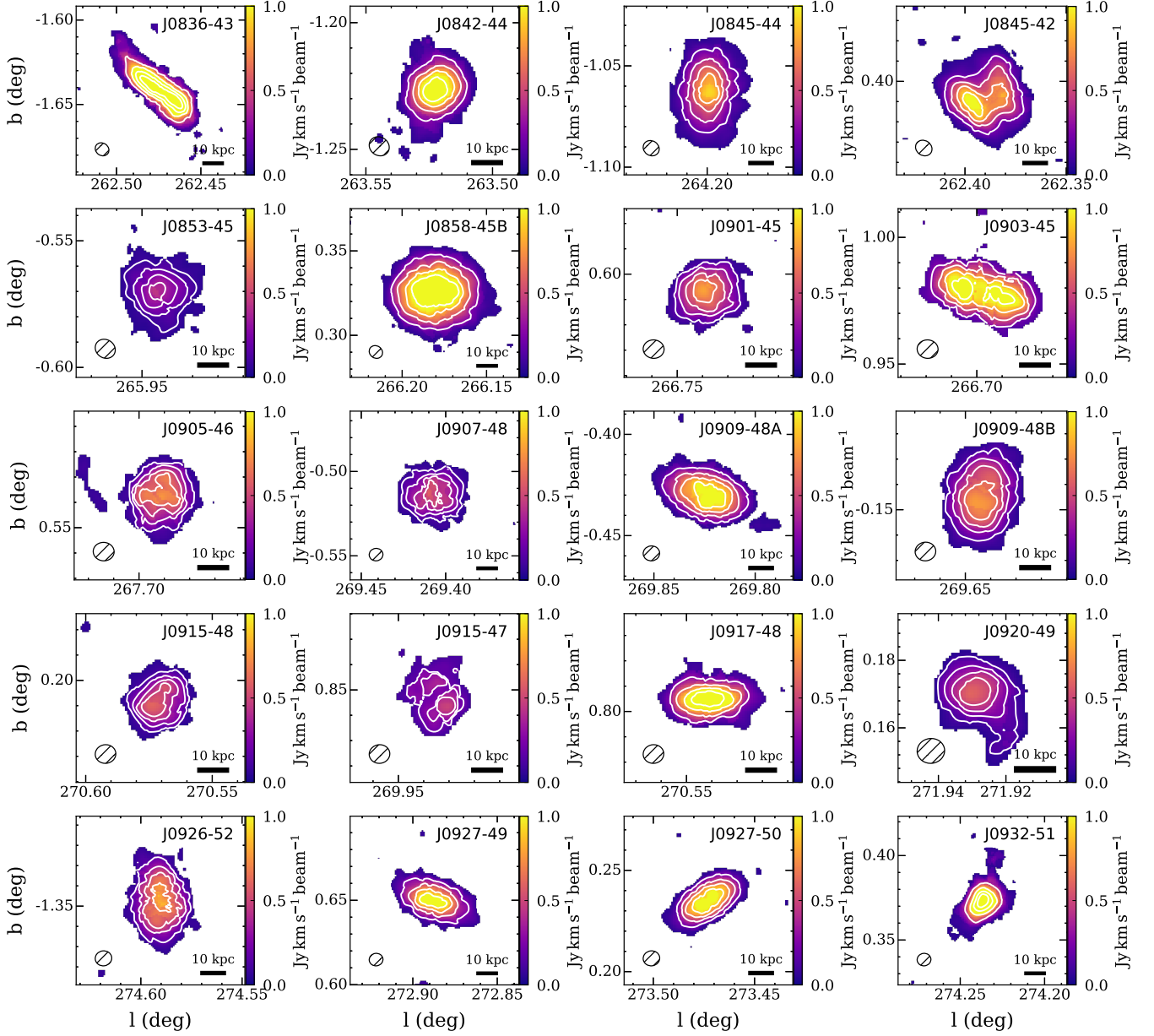


Figure B1. Moment-0 maps of HIZOA galaxies detected in Vela–SMGPS. The HIZOA identification name, the beam size, and a 10 kpc scale are shown in the upper right, bottom left, and bottom right corners of each image, respectively.

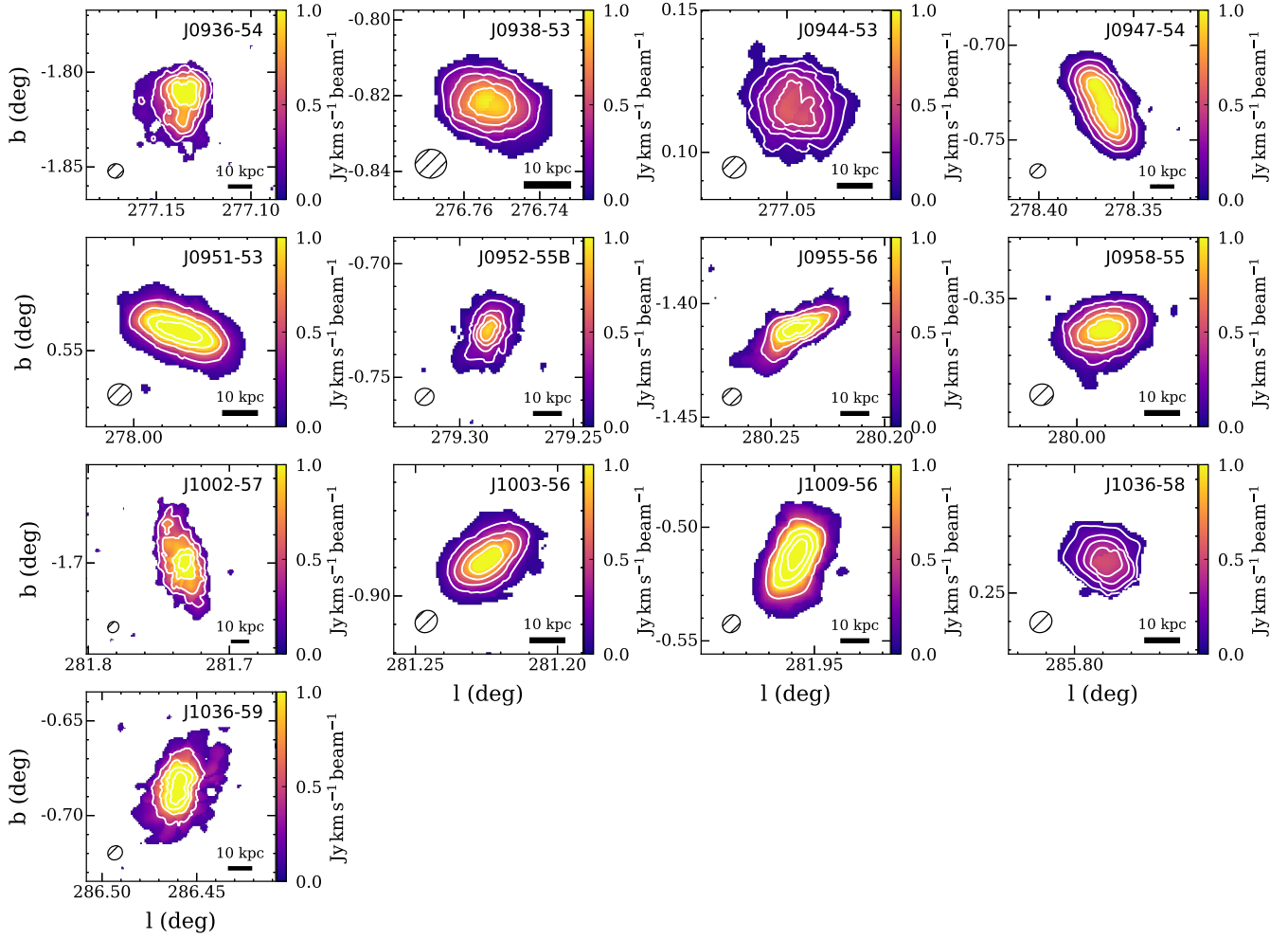


Figure B1. Moment-0 maps of HIZOA galaxies detected in Vela-SMGPS (Continued).

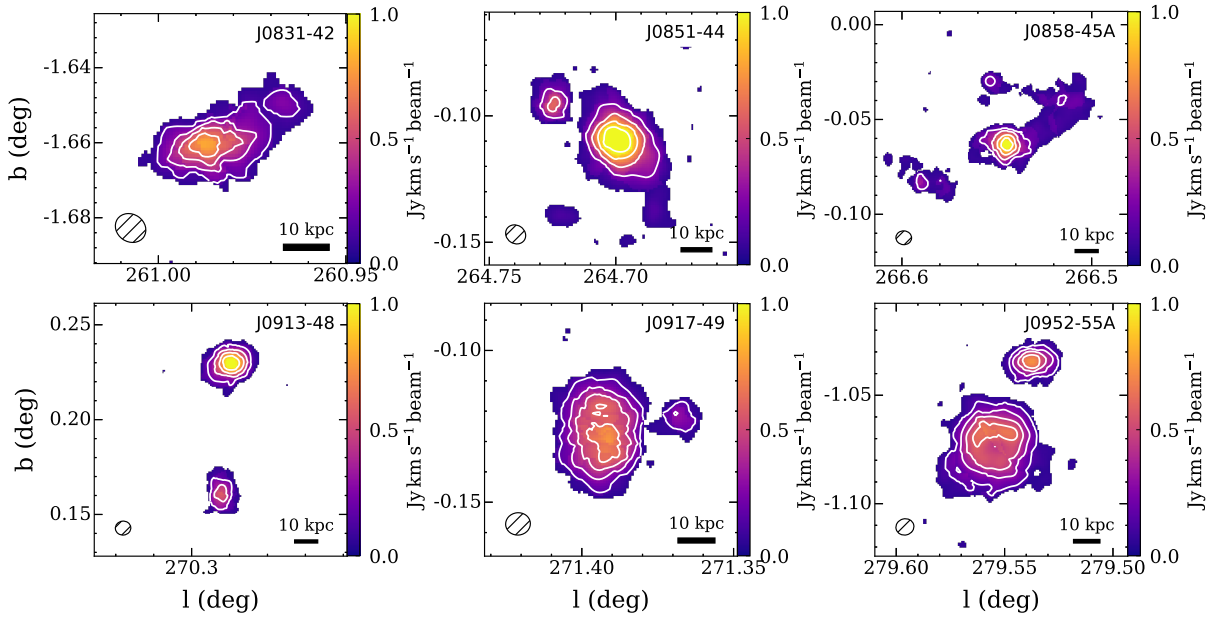


Figure B2. Moment-0 maps of HIZOA galaxies resolved into several galaxies in Vela-SMGPS.

APPENDIX C: VELA–SMGPS FULL CATALOG

In Table C1, we provide the derived HI properties obtained for the detected Vela–SMGPS detections ($260^\circ \leq \ell \leq 290^\circ$). A brief description of the columns in the catalog is provided below:

Column 1: Galaxy identifier (ID): Prefixed with SMGPS-HI followed by JHHMMSS-DDMMSS representing the rounded J2000 equatorial coordinates (RA and DEC) of the source.

Column 2: The Vela–SMGPS Mosaic (T_{xx}) in which the source has been detected (see e.g. top panel of Fig. 3) [T24–T33].

Columns 3 and 4: Galactic coordinates ℓ and b in units of degrees.

Column 5: Peak flux density S_{peak} as derived from the Global HI profile in Jy.

Columns 6 and 7: Integrated flux S_{int} with its corresponding error (ϵ_s) in Jy km s^{-1} (see Eq. 8 in Section 3.3).

Column 8: Mean local rms in mJy beam^{-1} .

Column 9: Optical heliocentric systemic velocity V_{hel} in km s^{-1} .

Columns 10 and 11: Linewidths (w_{20} , w_{50}) in km s^{-1} . These represent the measured linewidths at which the profile reaches 20% and 50% of its peak flux density, corrected for instrumental broadening (see Eq. 3 and Eq. 6).

Column 12: Logarithm of the HI mass determined from Eq. 7 [$\log(M_{\text{HI}}/M_\odot)$].

Column 13: Flags 1 or 2, where 1 signifies that the detection was classified as solid, 2 for a possible detection according to the visual verification process of each source (see Section 3.2). An asterisk (*) next to the flag code means that the detection has also been found in the area with the adjacent mosaic.

Column 14: Notes describing whether a galaxy is interacting (*i*), presents one or multiple companions (*w.comp(s)*), exhibits a wiggly baseline in its profile (*BL*) or if the measurement of w_{20} is uncertain due to the baseline behaviour (w_{20} *unc.*). Additionally, galaxies detected in major HI and IR catalogs are marked. For galaxies found in HIZOA (Staveley-Smith et al. 2016), their object names (e.g., J0831-42) are provided. ‘H’ denotes HI counterparts for galaxies also detected in HIPASS (Meyer et al. 2004). ‘I’ refers to the IRAS Point Source Catalog (Helou & Walker 1988), ‘M’ stands for 2MASX (Jarrett et al. 2000), ‘W’ represents matches from the Wide-field Infrared Survey Explorer catalog (WISE, Cutri et al. 2021), and ‘Z’ signifies Deep NIR follow-up observations of HIZOA galaxies obtained with the IRSF Telescope (Williams et al. 2014; Said et al. 2016).

Table C1. Vela-SMGPS full galaxy catalog: H I properties.

Name	Mosaic	ℓ	b	S_{peak}	S_{int}	ϵ_S	rms	V_{hel}	w_{20}	w_{50}	M_{HI}	Flag	Note
J2000	TXX	deg	deg	Jy	Jy km s ⁻¹	Jy km s ⁻¹	mJy beam ⁻¹	km s ⁻¹	km s ⁻¹	km s ⁻¹	log(M_{HI}/M_{\odot})	1/2	(14)
(1)	(2)	(3)	(4)	(5)	(6)	(7)	(8)	(9)	(10)	(11)	(12)	(13)	(14)
J082930-421453	T33	260.566	-1.903	0.010	1.25	0.23	0.46	2710	209	86	8.65	1	
J083133-422815	T33	260.970	-1.726	0.018	6.45	0.64	0.40	8242	466	415	10.33	1	J0831-42? w.comp (J083154-422631), M, W, Z
J083154-422631	T33	260.983	-1.659	0.018	2.99	0.42	0.36	8347	235	171	10.01	1	J0831-42, i, w.comp (J083133-422815)
J083217-415102	T33	260.548	-1.251	0.005	0.63	0.06	0.23	21824	315	277	10.18	1	
J083223-421453	T33	260.881	-1.471	0.003	0.26	0.05	0.27	8427	251	200	8.95	2	
J083236-423939	T33	261.237	-1.683	0.008	1.26	0.18	0.40	10767	448	330	9.85	1	
J083253-425142	T33	261.429	-1.762	0.006	1.22	0.17	0.43	8251	396	363	9.61	1	M, W
J083312-425407	T33	261.497	-1.737	0.011	2.28	0.22	0.39	11612	337	284	10.18	1	
J083406-414353	T33	260.655	-0.907	0.007	0.60	0.11	0.25	5427	126	61	8.93	1	
J083418-413412	T33	260.548	-0.780	0.003	0.19	0.03	0.24	10672	122	67	9.01	1	
J083440-413902	T33	260.653	-0.775	0.006	0.42	0.04	0.24	24375	177	89	10.09	1	
J083442-430649	T33	261.830	-1.644	0.007	1.14	0.16	0.32	8240	238	183	9.58	1	
J083446-422256	T33	261.251	-1.197	0.008	0.62	0.06	0.26	19550	123	86	10.07	1	
J083513-431435	T33	261.989	-1.647	0.004	0.30	0.04	0.35	11228	119	76	9.27	1	
J083523-413320	T33	260.657	-0.610	0.002	0.35	0.05	0.24	18205	373	274	9.76	2	
J083545-411907	T33	260.508	-0.414	0.015	4.51	0.64	0.26	4977	523	492	9.73	1	M, W
J083547-415531	T33	260.999	-0.711	0.006	0.44	0.06	0.25	13350	97	37	9.58	2	
J083550-430530	T33	261.937	-1.465	0.018	1.67	0.24	0.30	11223	124	87	10.01	1	
J083603-431104	T33	262.033	-1.491	0.010	2.21	0.31	0.33	5274	285	240	9.47	1	
J083611-411912	T33	260.560	-0.348	0.004	0.62	0.09	0.25	18221	411	396	10.01	1	
J083632-430608	T33	262.021	-1.371	0.017	1.94	0.28	0.30	5291	162	124	9.42	1	I, M, W
J083635-411721	T33	260.580	-0.269	0.022	2.54	0.36	0.26	5112	159	124	9.51	1	
J083650-433738	T33	262.474	-1.642	0.054	15.15	1.59	0.39	10699	595	536	10.93	1	J0836-43, BL, e, w.comp, I, H, M, W
J083703-425113	T33	261.881	-1.144	0.005	0.27	0.04	0.27	22009	91	63	9.82	2	
J083730-430654	T33	262.138	-1.237	0.005	0.64	0.06	0.28	24035	463	425	10.27	2	
J083732-431307	T33	262.225	-1.294	0.013	1.08	0.15	0.30	5278	106	72	9.16	1	
J083742-413835	T33	260.989	-0.316	0.011	0.83	0.12	0.26	9389	105	60	9.55	1	
J083746-435546	T33	262.817	-1.690	0.005	0.53	0.05	0.37	24183	271	251	10.19	1	
J083751-421432	T33	261.482	-0.658	0.004	0.30	0.04	0.26	11416	200	160	9.28	1	
J083815-435953	T33	262.924	-1.663	0.015	2.08	0.30	0.39	3899	152	120	9.18	1	
J083818-420056	T33	261.352	-0.454	0.002	0.33	0.05	0.25	10808	178	156	9.27	1	
J083824-413039	T33	260.963	-0.132	0.003	0.38	0.07	0.26	7061	198	143	8.96	1	
J083826-441859	T33	263.196	-1.831	0.009	0.55	0.08	0.56	10188	194	79	9.44	1	
J083831-440328	T33	263.000	-1.661	0.007	0.35	0.07	0.37	5657	201	92	8.74	1	
J083841-405454	T33	260.521	0.270	0.004	0.29	0.04	0.24	17809	169	128	9.66	1	
J083843-423114	T33	261.801	-0.699	0.003	0.24	0.03	0.25	18032	294	263	9.58	2	
J083847-444025	T32	263.519	-1.997	0.007	0.62	0.09	0.61	10139	479	368	9.50	2	BL
J083849-425455	T33	262.125	-0.924	0.010	1.36	0.19	0.29	10760	263	235	9.89	1	
J083851-440501	T33	263.057	-1.629	0.007	0.56	0.08	0.38	10380	204	115	9.47	1	w.comp (J083855-440223)
J083855-440223	T33	263.029	-1.594	0.017	2.24	0.22	0.38	10586	302	259	10.09	1	i, w.comp (J083851-440501), M, W
J083901-432543	T33	262.555	-1.207	0.006	0.35	0.05	0.29	8028	119	89	9.04	1	
J083902-441944	T33	263.272	-1.752	0.008	0.65	0.09	0.48	10211	201	142	9.52	1	
J083910-414722	T33	261.270	-0.189	0.002	0.11	0.04	0.26	9402	223	168	8.67	2	
J083935-444823	T32	263.711	-1.965	0.009	0.53	0.08	0.53	15792	290	88	9.81	1*	
J083942-412453	T33	261.034	0.119	0.003	0.19	0.03	0.25	10684	239	94	9.02	2	
J083944-422055	T33	261.778	-0.446	0.003	0.31	0.04	0.25	24072	185	176	9.95	1	
J083948-423436	T33	261.967	-0.574	0.003	0.28	0.04	0.25	17695	131	44	9.63	1	
J083951-420632	T33	261.602	-0.282	0.002	0.16	0.03	0.25	10541	98	61	8.94	2	
J083952-423922	T33	262.037	-0.614	0.003	0.20	0.03	0.26	10559	124	108	9.04	1	
J083958-410700	T33	260.829	0.341	0.004	0.26	0.05	0.24	7548	151	98	8.86	1	
J084001-405123	T33	260.629	0.508	0.003	0.21	0.03	0.24	17669	194	130	9.52	1	i
J084020-425103	T33	262.244	-0.665	0.004	0.16	0.03	0.26	10577	169	106	8.95	1	
J084025-421634	T33	261.798	-0.302	0.017	1.62	0.30	0.28	2714	138	87	8.76	1	
J084037-412924	T33	261.199	0.209	0.008	1.14	0.11	0.26	17802	320	304	10.25	1	
J084050-414324	T33	261.408	0.097	0.001	0.14	0.02	0.24	24694	262	228	9.63	1	
J084050-445537	T32	263.941	-1.864	0.007	0.61	0.09	0.53	7935	244	159	9.27	1*	
J084054-440439	T33	263.277	-1.334	0.008	0.57	0.11	0.31	3592	97	70	8.55	1	
J084057-420725	T33	261.738	-0.130	0.003	0.17	0.03	0.26	8215	157	91	8.75	1	
J084058-410610	T33	260.933	0.498	0.002	0.20	0.04	0.25	8233	128	97	8.81	1	
J084102-411337	T33	261.040	0.433	0.011	0.57	0.11	0.27	2785	132	38	8.33	1	
J084110-413150	T33	261.293	0.265	0.006	0.56	0.10	0.26	5003	199	143	8.83	1	
J084115-434114	T33	263.006	-1.046	0.008	1.25	0.18	0.31	8002	226	147	9.59	1	w.comps (one is J084129-433917)
J084121-422045	T33	261.959	-0.208	0.003	0.12	0.01	0.25	10602	164	120	8.82	2	
J084129-433917	T33	263.007	-0.992	0.013	1.86	0.26	0.31	8084	292	134	9.77	1	i, w.comp (J084115-434114), M, W
J084130-434638	T33	263.106	-1.064	0.004	0.36	0.07	0.29	5482	341	307	8.72	2	
J084136-412249	T33	261.225	0.421	0.008	1.05	0.10	0.27	17740	437	178	10.21	1	w.comp
J084137-405157	T33	260.822	0.741	0.005	0.56	0.08	0.30	11637	169	148	9.57	1	
J084137-440359	T33	263.348	-1.225	0.003	0.15	0.02	0.28	24284	186	186	9.64	2	
J084143-423941	T33	262.249	-0.348	0.009	0.86	0.12	0.28	13747	193	105	9.90	2	
J084145-420920	T33	261.855	-0.031	0.008	0.30	0.04	0.26	11375	102	54	9.28	2	
J084158-422930	T33	262.144	-0.207	0.009	1.65	0.16	0.28	11364	426	345	10.02	1	BL, i, w.comp (J084218-422946), M, W
J084159-440321	T33	263.378	-1.168	0.006	0.36	0.07	0.29	3747	310	49	8.39	2	
J084159-430044	T33	262.556	-0.526	0.004	0.32	0.05	0.28	10874	216	177	9.27	1	
J084205-434825	T33	263.195	-0.999	0.006	0.36	0.05	0.28	9403	158	93	9.19	1	
J084213-441221	T32	263.523	-1.227	0.034	5.07	0.72	0.30	3754	204	163	9.54	1*	J0842-44, W, Z
J084218-422946	T33	262.186	-0.161	0.007	2.36	0.23	0.27	11398	443	407	10.18	1	w.comp (J084158-422930), M, W
J084219-425250	T33	262.489	-0.397	0.003	0.29	0.05	0.27	5228	152	90	8.59	1	
J084227-433808	T33	263.100	-0.842	0.003	0.13	0.02	0.27	11316	70	52	8.92	2	

* Detected by the overlapping region of the next mosaic as well.

Table C1 continued

Name	Mosaic	l	b	S_{peak}	S_{int}	ε_S	rms	V_{hel}	w_{20}	w_{50}	M_{HI}	Flag	Note
J2000	TXX	deg	deg	Jy	Jy km s ⁻¹	Jy km s ⁻¹	mJy beam ⁻¹	km s ⁻¹	km s ⁻¹	km s ⁻¹	log(M_{HI}/M_{\odot})	1/2	(14)
(1)	(2)	(3)	(4)	(5)	(6)	(7)	(8)	(9)	(10)	(11)	(12)	(13)	(14)
J084233-445800	T32	264.159	-1.649	0.011	0.67	0.09	0.40	7782	110	78	9.30	1	
J084246-412920	T33	261.445	0.526	0.007	1.25	0.18	0.27	11528	302	266	9.91	1	
J084252-450235	T32	264.254	-1.651	0.006	0.43	0.06	0.39	7728	119	83	9.10	1	
J084254-441017	T32	263.572	-1.108	0.014	1.45	0.21	0.30	4478	117	101	9.15	1*	
J084300-421251	T33	262.044	0.115	0.003	0.24	0.03	0.24	11489	256	208	9.20	1	
J084311-445941	T32	264.251	-1.578	0.008	0.75	0.11	0.36	9302	157	126	9.50	1	
J084312-422427	T33	262.218	0.024	0.004	0.23	0.03	0.25	13772	208	173	9.32	1	
J084317-421906	T33	262.158	0.091	0.007	0.81	0.08	0.25	16772	203	170	10.05	1	
J084319-432446	T33	263.021	-0.582	0.003	0.20	0.04	0.27	8269	150	79	8.81	2	
J084320-451123	T32	264.420	-1.677	0.015	2.20	0.31	0.39	7737	315	297	9.81	1	
J084358-433829	T33	263.273	-0.631	0.006	0.49	0.09	0.29	5574	321	49	8.87	1	M, W
J084400-421558	T33	262.199	0.228	0.020	1.22	0.23	0.27	2693	71	53	8.63	1	
J084416-433712	T33	263.290	-0.575	0.003	0.16	0.02	0.28	16396	126	109	9.32	1	
J084424-424448	T33	262.622	-0.012	0.004	0.24	0.05	0.28	8253	229	104	8.91	1	
J084429-433211	T33	263.249	-0.492	0.007	0.79	0.11	0.30	8155	218	161	9.41	1	
J084443-454133	T32	264.966	-1.798	0.010	0.68	0.10	0.48	8144	88	55	9.34	1	
J084444-454709	T32	265.040	-1.854	0.014	1.61	0.16	0.55	14075	345	312	10.19	1	M, W
J084457-423159	T33	262.516	0.199	0.004	0.38	0.05	0.25	22479	277	178	9.98	2	
J084458-444013	T32	264.191	-1.129	0.004	0.19	0.03	0.26	14759	157	90	9.31	1	
J084458-450543	T32	264.525	-1.392	0.008	0.58	0.08	0.30	11309	113	73	9.56	1	
J084507-430208	T33	262.928	-0.091	0.014	3.79	0.37	0.30	8133	512	458	10.09	1	M, W
J084512-440508	T32	263.760	-0.732	0.005	0.52	0.10	0.29	3356	197	162	8.45	1*	
J084513-424336	T33	262.699	0.118	0.014	1.62	0.30	0.28	2755	121	96	8.77	1	
J084517-443806	T32	264.199	-1.062	0.039	6.17	0.88	0.29	2732	200	170	9.35	1	J0845-44, W, Z
J084518-440603	T32	263.783	-0.727	0.003	0.20	0.04	0.28	5565	194	93	8.47	2	
J084520-431229	T33	263.089	-0.165	0.007	0.61	0.06	0.28	22252	245	91	10.18	1	
J084522-421848	T33	262.392	0.395	0.046	12.21	1.73	0.26	1733	364	313	9.25	1	J0845-42, I, M, W, Z
J084522-430750	T33	263.032	-0.113	0.004	0.23	0.03	0.27	20839	303	150	9.70	1	W
J084530-450210	T32	264.537	-1.282	0.005	0.27	0.04	0.28	22618	76	29	9.84	2	
J084546-450241	T32	264.573	-1.251	0.005	0.34	0.05	0.29	9535	175	110	9.18	2	
J084549-424337	T33	262.767	0.202	0.006	0.68	0.13	0.27	5108	212	198	8.94	1	M, W
J084600-421004	T33	262.352	0.579	0.003	0.19	0.03	0.30	11234	214	185	9.07	1	
J084618-460230	T32	265.412	-1.799	0.008	0.43	0.08	0.44	6261	161	128	8.92	1	
J084624-435746	T32	263.799	-0.487	0.004	0.40	0.06	0.27	11244	322	186	9.39	2*	
J084700-452834	T32	265.046	-1.351	0.002	0.27	0.04	0.29	14209	199	155	9.42	2	
J084708-444731	T32	264.527	-0.903	0.012	0.93	0.17	0.28	4118	165	132	8.89	1	
J084713-424301	T33	262.920	0.409	0.007	0.62	0.09	0.29	10403	162	126	9.51	1	
J084717-422558	T33	262.706	0.597	0.003	0.16	0.03	0.28	11248	122	52	9.00	2	
J084719-430510	T33	263.219	0.191	0.007	0.74	0.11	0.29	16431	332	283	10.00	1	
J084731-432134	T32	263.455	0.049	0.024	2.70	0.27	0.29	22535	150	100	10.83	1*	i, w.comp
J084738-420048	T33	262.422	0.912	0.017	2.18	0.31	0.54	4890	165	114	9.40	1	
J084746-423651	T33	262.903	0.552	0.004	0.37	0.05	0.29	9192	109	75	9.18	1	
J084753-451709	T32	264.995	-1.111	0.005	0.24	0.03	0.28	9515	68	51	9.03	1	
J084753-440535	T32	264.067	-0.360	0.003	0.20	0.03	0.26	14908	214	177	9.35	2	
J084755-441119	T32	264.145	-0.416	0.010	2.44	0.24	0.32	10195	623	533	10.09	1	M, W
J084758-441230	T32	264.167	-0.421	0.002	0.25	0.05	0.30	8369	185	159	8.93	2	
J084811-423659	T33	262.954	0.611	0.004	0.43	0.06	0.31	21213	281	281	9.99	1	
J084813-462001	T32	265.847	-1.724	0.005	0.32	0.04	0.38	8300	238	144	9.03	1	
J084813-421337	T33	262.656	0.862	0.009	0.73	0.10	0.40	8153	164	146	9.37	1	
J084823-464139	T32	266.145	-1.928	0.009	0.45	0.06	0.69	7613	163	128	9.10	1	
J084831-460825	T32	265.728	-1.563	0.008	0.54	0.08	0.30	6302	208	96	9.02	2	
J084833-440720	T32	264.166	-0.285	0.004	0.37	0.05	0.27	15087	171	156	9.62	1	
J084834-441019	T32	264.205	-0.316	0.006	0.75	0.11	0.31	8356	244	179	9.41	1	i
J084840-425345	T33	263.227	0.504	0.014	1.78	0.25	0.33	4842	230	171	9.31	1	
J084842-461332	T32	265.814	-1.592	0.007	0.65	0.09	0.32	16633	229	208	9.95	1	
J084847-424221	T33	263.093	0.640	0.005	0.23	0.07	0.37	2691	124	39	7.90	1	
J084850-433142	T32	263.736	0.128	0.005	0.29	0.04	0.27	15948	146	99	9.56	1*	
J084857-453839	T32	265.390	-1.192	0.003	0.27	0.04	0.26	23259	305	241	9.86	2	
J084902-452938	T32	265.284	-1.085	0.016	2.39	0.34	0.29	5953	262	247	9.61	1	w.comp (J084909-453234), M
J084909-453234	T32	265.334	-1.100	0.004	0.21	0.04	0.27	5878	106	73	8.54	1	w.comp (J084902-452938)
J084911-432810	T32	263.732	0.216	0.005	0.60	0.09	0.27	14047	363	337	9.77	1*	BL
J084913-451301	T32	265.089	-0.885	0.004	0.40	0.06	0.27	9571	170	81	9.25	2	
J084915-441112	T32	264.294	-0.230	0.006	0.25	0.04	0.27	23915	89	63	9.86	2	
J084917-453107	T32	265.330	-1.067	0.003	0.07	0.01	0.26	17485	108	56	9.00	2	
J084921-460424	T32	265.768	-1.407	0.003	0.35	0.05	0.27	14413	209	165	9.56	1	
J084927-463119	T32	266.127	-1.677	0.005	0.65	0.09	0.39	16617	368	200	9.95	1	
J084930-461726	T32	265.952	-1.526	0.007	0.49	0.09	0.31	4291	141	74	8.64	1	
J084939-440217	T32	264.225	-0.079	0.003	0.12	0.02	0.25	23730	124	12	9.55	2	
J084957-440836	T32	264.340	-0.105	0.012	1.85	0.26	0.30	10139	224	216	9.97	1	
J085007-424438	T33	263.277	0.805	0.007	0.43	0.06	0.49	10475	120	83	9.37	2	
J085013-461004	T32	265.935	-1.353	0.009	1.02	0.14	0.28	4977	78	78	9.09	1	
J085013-462501	T32	266.130	-1.509	0.005	0.53	0.08	0.33	7201	160	113	9.13	1	
J085017-463558	T32	266.277	-1.617	0.015	0.81	0.12	0.36	8365	94	38	9.44	1	
J085017-430800	T33	263.597	0.582	0.003	0.33	0.05	0.30	22055	282	198	9.91	1*	
J085025-453538	T32	265.515	-0.960	0.003	0.15	0.03	0.27	5938	78	78	8.40	2	
J085111-452112	T32	265.413	-0.705	0.004	0.71	0.10	0.28	7937	166	150	9.34	2	BL
J085113-442532	T32	264.702	-0.109	0.057	8.21	1.16	0.30	3702	203	143	9.74	1	J0851-44, i, w.comp, W, Z
J085126-453420	T32	265.610	-0.810	0.007	0.57	0.08	0.26	14042	162	111	9.75	1	

* Detected by the overlapping region of the next mosaic as well.

Table C1 continued

Name	Mosaic	l	b	S_{peak}	S_{int}	ϵ_s	rms	V_{hel}	w_{20}	w_{50}	M_{HI}	Flag	Note
J2000	TXX	deg	deg	Jy	Jy km s^{-1}	Jy km s^{-1}	mJy beam^{-1}	km s^{-1}	km s^{-1}	km s^{-1}	$\log(M_{\text{HI}}/M_{\odot})$	1/2	(14)
(1)	(2)	(3)	(4)	(5)	(6)	(7)	(8)	(9)	(10)	(11)	(12)	(13)	(14)
J085131-462516	T32	266.274	-1.339	0.004	0.36	0.07	0.29	7655	169	135	9.01	1	W
J085132-450447	T32	265.243	-0.481	0.004	0.30	0.04	0.27	9749	104	69	9.14	2	
J085133-425550	T32	263.589	0.891	0.007	1.65	0.16	0.45	15979	441	410	10.32	1*	M, W
J085149-442844	T32	264.811	-0.061	0.004	0.13	0.02	0.26	11991	104	61	8.95	2	
J085152-435013	T32	264.323	0.356	0.011	0.72	0.07	0.28	17742	117	84	10.05	1	
J085203-454143	T32	265.774	-0.805	0.004	0.31	0.04	0.26	15588	202	148	9.57	2	
J085206-464105	T31	266.542	-1.430	0.009	0.52	0.07	0.30	7733	77	45	9.18	1*	
J085219-461341	T32	266.214	-1.110	0.003	0.10	0.02	0.25	8608	79	65	8.55	2	
J085250-455458	T32	266.031	-0.842	0.005	0.37	0.05	0.26	23095	172	93	10.00	1	
J085256-470941	T31	267.000	-1.625	0.003	0.48	0.07	0.48	11551	163	130	9.49	1	
J085300-440408	T32	264.632	0.365	0.006	0.27	0.05	0.27	4994	199	132	8.51	1	
J085303-451624	T32	265.561	-0.401	0.006	0.39	0.05	0.25	14288	93	30	9.59	2	
J085307-433430	T32	264.265	0.696	0.006	0.29	0.04	0.37	22591	135	112	9.88	1	
J085309-454426	T32	265.933	-0.685	0.006	1.13	0.16	0.26	11530	543	502	9.87	1	M, W
J085311-462719	T31	266.484	-1.140	0.005	0.61	0.09	0.27	17634	278	263	9.97	1*	BL
J085315-444917	T32	265.237	-0.084	0.004	0.30	0.04	0.24	15399	180	180	9.54	1	
J085323-441225	T32	264.782	0.329	0.008	0.77	0.14	0.27	3732	122	97	8.71	1	
J085334-440625	T32	264.726	0.418	0.006	0.38	0.05	0.26	15115	209	170	9.64	1	
J085342-454028	T32	265.943	-0.570	0.029	2.15	0.30	0.27	5935	100	49	9.57	1	J0853-45
J085342-452233	T32	265.714	-0.378	0.002	0.18	0.03	0.25	14852	180	160	9.30	2	
J085342-434122	T32	264.423	0.706	0.016	1.70	0.24	0.37	5405	123	103	9.38	1	NaN
J085345-462655	T31	266.542	-1.061	0.004	0.15	0.02	0.30	14870	174	142	9.22	2	
J085358-460401	T32	266.274	-0.787	0.007	0.54	0.08	0.26	12198	176	143	9.59	1	w.comp (J085406-460319)
J085406-460319	T32	266.280	-0.761	0.006	0.96	0.14	0.27	12134	342	302	9.84	1	w.comp (J085358-460401), W
J085422-443613	T32	265.198	0.208	0.025	2.07	0.29	0.28	8387	113	73	9.85	1	
J085424-443700	T32	265.213	0.205	0.003	0.27	0.04	0.24	15464	369	315	9.50	1	
J085425-462543	T31	266.600	-0.961	0.003	0.30	0.06	0.31	7369	293	254	8.90	2*	
J085435-450802	T32	265.630	-0.103	0.005	0.34	0.05	0.25	14620	76	30	9.55	2	
J085443-460254	T32	266.343	-0.676	0.003	0.56	0.08	0.26	17690	400	343	9.94	1	
J085444-460725	T31	266.402	-0.723	0.014	2.11	0.21	0.27	11446	231	177	10.13	1*	
J085457-441324	T32	264.976	0.534	0.003	0.15	0.03	0.30	8975	79	79	8.78	2	
J085459-454736	T32	266.178	-0.476	0.009	1.60	0.23	0.28	7810	225	175	9.68	1	
J085459-440524	T32	264.878	0.625	0.008	1.08	0.15	0.32	10184	256	127	9.73	1	w.comp (J085526-440611)
J085511-445242	T32	265.501	0.141	0.012	1.49	0.21	0.27	8307	255	188	9.70	1	
J085520-451121	T32	265.758	-0.037	0.004	0.17	0.02	0.24	15292	123	87	9.29	2	
J085522-445251	T32	265.525	0.165	0.017	1.40	0.20	0.26	11478	181	78	9.95	1	
J085526-440611	T32	264.939	0.677	0.006	0.37	0.05	0.34	10073	122	87	9.27	1	w.comp (J085459-440524)
J085526-454748	T32	266.232	-0.417	0.005	0.30	0.04	0.25	23760	144	62	9.93	2	
J085533-450322	T32	265.680	0.077	0.007	0.63	0.09	0.25	15031	110	72	9.84	1	
J085549-454527	T32	266.246	-0.341	0.003	0.26	0.04	0.24	22440	216	176	9.82	2	
J085550-442422	T32	265.216	0.535	0.007	0.60	0.09	0.29	16342	304	257	9.90	1	
J085637-455329	T31	266.438	-0.321	0.003	0.23	0.03	0.25	20959	177	157	9.70	2*	
J085645-444218	T32	265.551	0.467	0.003	0.18	0.02	0.25	11387	178	152	9.05	1	
J085648-443706	T32	265.489	0.528	0.007	0.68	0.10	0.28	10094	122	105	9.53	1	
J085652-444850	T32	265.647	0.412	0.005	0.43	0.06	0.24	14815	173	87	9.67	1	
J085657-440927	T32	265.158	0.850	0.006	0.14	0.03	0.49	11323	121	57	8.94	2	
J085700-450923	T32	265.921	0.206	0.004	0.14	0.03	0.25	11364	121	78	8.94	1	
J085708-454520	T32	266.393	-0.165	0.005	0.65	0.09	0.26	15979	230	184	9.91	1	
J085712-461138	T31	266.732	-0.443	0.004	0.64	0.09	0.30	11851	198	50	9.64	1*	i
J085717-455459	T31	266.531	-0.251	0.004	0.11	0.02	0.26	7415	79	69	8.46	2	
J085725-454339	T31	266.403	-0.110	0.004	0.24	0.03	0.26	11781	130	118	9.21	1*	
J085735-445640	T32	265.828	0.422	0.004	0.32	0.05	0.24	15199	162	125	9.56	1	
J085736-443930	T32	265.613	0.611	0.005	0.50	0.07	0.28	18191	228	193	9.92	1	
J085745-450353	T32	265.939	0.367	0.006	0.32	0.05	0.26	14763	139	40	9.53	2	
J085755-442607	T32	265.481	0.799	0.009	1.15	0.16	0.37	10098	331	189	9.76	1	
J085801-463229	T31	267.089	-0.561	0.010	0.80	0.11	0.53	11701	412	81	9.73	1	w.comp (J085803-463915)
J085803-463915	T31	267.177	-0.631	0.007	0.48	0.07	0.49	11469	178	166	9.49	1	w.comp (J085801-463229)
J085810-454817	T31	266.548	-0.060	0.021	6.30	0.89	0.32	2699	323	249	9.35	1*	J0858-45A, i
J085814-443142	T32	265.588	0.781	0.008	1.51	0.21	0.35	11355	563	498	9.98	1	W
J085814-455101	T31	266.590	-0.081	0.017	1.84	0.34	0.32	2828	180	129	8.85	1	One of J0858-45A's companions
J085815-465136	T31	267.356	-0.738	0.007	0.50	0.09	0.49	4877	109	71	8.76	1	
J085828-451630	T32	266.181	0.325	0.099	19.43	2.76	0.31	2691	280	234	9.83	1	J0858-45B, I, H, M, W, Z
J085832-472623	T31	267.825	-1.082	0.011	1.39	0.20	0.67	4881	191	149	9.21	1	
J085833-454015	T32	266.489	0.076	0.004	0.15	0.03	0.28	7706	111	72	8.62	2*	
J085841-445601	T32	265.947	0.577	0.002	0.15	0.02	0.29	15450	203	163	9.24	1	
J085901-444836	T32	265.892	0.702	0.006	0.49	0.05	0.34	22948	297	109	10.11	2	
J085902-461756	T31	267.020	-0.269	0.006	0.85	0.12	0.34	7493	256	234	9.37	1	
J085914-464157	T31	267.344	-0.507	0.006	0.30	0.04	0.43	20020	126	107	9.78	1	
J085918-460511	T31	266.889	-0.096	0.005	0.43	0.04	0.30	24959	235	226	10.13	1*	
J085936-480854	T31	268.479	-1.410	0.006	0.51	0.07	0.38	19661	270	63	9.99	1	
J090000-462624	T31	267.235	-0.237	0.008	0.70	0.07	0.37	20087	173	147	10.14	1	
J090010-460609	T31	267.000	0.007	0.005	0.24	0.03	0.31	17352	277	277	9.56	2	
J090034-462609	T31	267.296	-0.161	0.003	0.23	0.03	0.39	11728	145	110	9.19	1	
J090117-453901	T31	266.788	0.451	0.011	0.74	0.11	0.35	14288	164	99	9.87	1*	
J090120-461723	T31	267.273	0.034	0.007	0.76	0.11	0.35	14066	259	236	9.87	1	
J090132-464811	T31	267.682	-0.279	0.007	0.31	0.04	0.49	11423	122	76	9.29	1	
J090133-463052	T31	267.468	-0.085	0.004	0.51	0.05	0.35	24277	183	136	10.18	1	
J090139-474512	T31	268.408	-0.891	0.004	0.55	0.08	0.51	14929	307	179	9.78	1	

* Detected by the overlapping region of the next mosaic as well.

Table C1 continued

Name J2000 (1)	Mosaic TXX (2)	l deg (3)	b deg (4)	S_{peak} Jy (5)	S_{int} Jy km s ⁻¹ (6)	ε_s Jy km s ⁻¹ (7)	rms mJy beam ⁻¹ (8)	V_{hel} km s ⁻¹ (9)	w_{20} km s ⁻¹ (10)	w_{50} km s ⁻¹ (11)	M_{HI} log(M_{HI}/M_{\odot}) (12)	Flag 1/2 (13)	Note (14)
J090142-453108	T31	266.738	0.593	0.029	3.07	0.44	0.39	7693	129	111	9.95	1*	J0901-45
J090204-462557	T31	267.465	0.036	0.006	0.68	0.10	0.37	16584	407	245	9.97	2	i
J090209-454345	T31	266.947	0.512	0.004	0.22	0.03	0.35	14367	180	180	9.36	1*	
J090209-455723	T31	267.117	0.362	0.006	0.15	0.02	0.34	21228	170	148	9.52	2	
J090226-485427	T31	269.360	-1.558	0.006	0.26	0.11	0.37	19941	311	260	9.72	2	i
J090241-471529	T31	268.153	-0.432	0.003	0.21	0.03	0.46	13369	125	109	9.26	2	
J090259-482628	T31	269.070	-1.181	0.003	0.13	0.02	0.32	12510	179	161	8.99	1	
J090301-490306	T30	269.530	-1.583	0.004	0.25	0.04	0.36	10058	190	94	9.10	2	
J090309-484812	T31	269.359	-1.401	0.003	0.37	0.07	0.34	3754	397	286	8.40	2	
J090312-451400	T31	266.697	0.978	0.046	7.52	1.07	0.71	2699	210	196	9.42	1*	J0903-45, W, Z
J090315-485528	T31	269.461	-1.469	0.007	0.63	0.09	0.34	15501	389	281	9.88	2*	
J090322-481912	T31	269.022	-1.054	0.006	0.42	0.08	0.35	6688	199	157	8.96	1	w.comp (J090327-482346)
J090327-482346	T31	269.089	-1.093	0.009	0.73	0.10	0.32	6763	126	101	9.21	1	w.comp (J090322-481912)
J090340-482052	T31	269.077	-1.034	0.005	0.47	0.07	0.32	12404	200	142	9.55	2	
J090341-461941	T31	267.572	0.314	0.003	0.45	0.04	0.31	24899	241	197	10.14	1	
J090358-473135	T31	268.497	-0.449	0.012	1.02	0.14	0.50	13260	174	138	9.95	1	w.comp
J090407-460259	T31	267.415	0.556	0.008	0.48	0.07	0.37	11432	190	147	9.49	1	
J090411-483953	T30	269.369	-1.182	0.002	0.27	0.04	0.31	12546	173	157	9.31	1*	
J090430-482338	T31	269.204	-0.961	0.003	0.17	0.02	0.35	10073	143	94	8.91	2	
J090432-463202	T31	267.822	0.285	0.004	0.13	0.02	0.33	8233	72	53	8.63	2	
J090433-464436	T31	267.980	0.147	0.004	0.24	0.03	0.34	11592	182	154	9.20	2	
J090448-495749	T30	270.404	-1.974	0.008	0.32	0.05	0.64	19203	133	133	9.77	2	
J090453-474342	T31	268.751	-0.469	0.006	0.80	0.11	0.45	7382	281	249	9.33	2	BL, w.comp?
J090504-462707	T31	267.824	0.409	0.003	0.26	0.04	0.31	22664	346	296	9.83	2	
J090505-455504	T31	267.429	0.768	0.008	0.48	0.07	0.45	15164	180	180	9.73	1	
J090513-461504	T31	267.692	0.562	0.025	3.75	0.53	0.37	7489	219	187	10.01	1	J0905-46, M, W
J090517-460554	T31	267.585	0.672	0.010	0.76	0.11	0.38	7426	119	104	9.31	1	
J090518-471541	T31	268.452	-0.103	0.013	3.21	0.32	0.44	11720	383	276	10.33	1	w.comp (J090553-472056)
J090520-460530	T31	267.586	0.684	0.010	1.10	0.16	0.39	5136	174	93	9.15	1	w.comp (J090526-460504)
J090522-492610	T30	270.074	-1.553	0.004	0.77	0.08	0.37	17492	330	268	10.07	1	
J090524-475928	T31	269.003	-0.581	0.002	0.17	0.03	0.42	7679	152	123	8.68	2	
J090526-460504	T31	267.592	0.700	0.010	0.72	0.10	0.39	5626	146	68	9.04	1	w.comp (J090520-460530)
J090526-462127	T31	267.795	0.518	0.004	0.37	0.07	0.34	7409	136	82	9.00	1	
J090541-483526	T30	269.481	-0.948	0.003	0.26	0.04	0.27	24008	186	125	9.88	2	
J090545-465324	T31	268.226	0.201	0.004	0.18	0.03	0.32	11674	121	105	9.07	1	
J090546-463737	T31	268.033	0.379	0.003	0.06	0.01	0.34	6307	143	28	8.08	2	
J090551-482819	T30	269.411	-0.848	0.012	3.22	0.46	0.32	6697	355	338	9.85	1*	M
J090553-472056	T31	268.581	-0.091	0.017	1.71	0.17	0.40	11787	174	127	10.07	1	w.comps (one is J090518-471541)
J090554-480541	T31	269.137	-0.588	0.005	0.94	0.13	0.35	13056	275	100	9.89	1	
J090612-491359	T30	270.013	-1.317	0.003	0.35	0.05	0.30	17485	221	193	9.73	1	
J090617-481155	T31	269.257	-0.610	0.008	1.42	0.14	0.33	13058	441	398	10.08	1	i, W
J090625-482605	T30	269.447	-0.752	0.009	1.22	0.12	0.29	16899	332	278	10.24	1*	
J090628-492858	T30	270.228	-1.452	0.006	0.47	0.07	0.33	17887	243	121	9.87	1	
J090633-465354	T31	268.325	0.297	0.012	0.62	0.12	0.35	5165	120	105	8.91	1	
J090633-462039	T31	267.915	0.670	0.007	0.53	0.07	0.43	7453	265	171	9.15	1	
J090649-460729	T31	267.783	0.851	0.008	1.23	0.18	0.51	11722	239	215	9.92	1	W
J090649-462701	T31	268.024	0.633	0.011	1.68	0.24	0.45	7486	313	296	9.66	1	
J090651-464741	T31	268.282	0.404	0.010	1.33	0.19	0.39	11917	371	312	9.96	1	
J090656-491507	T30	270.107	-1.241	0.008	1.36	0.19	0.31	11389	379	322	9.94	1	
J090659-470105	T31	268.463	0.271	0.003	0.31	0.04	0.33	11630	182	159	9.31	2	
J090703-490718	T30	270.025	-1.138	0.006	0.34	0.05	0.29	14747	112	76	9.56	1	
J090707-483649	T30	269.658	-0.787	0.002	0.21	0.03	0.28	12828	177	140	9.22	1*	
J090719-481439	T30	269.406	-0.514	0.028	4.65	0.66	0.31	5232	215	179	9.79	1*	J0907-48, M, W, Z
J090725-484244	T30	269.763	-0.818	0.003	0.19	0.03	0.27	12883	159	104	9.18	2*	
J090749-483657	T30	269.736	-0.705	0.002	0.35	0.05	0.27	17300	276	198	9.72	2*	W
J090751-490047	T30	270.033	-0.969	0.003	0.48	0.07	0.27	17560	336	270	9.87	1	
J090753-465328	T31	268.473	0.470	0.002	0.17	0.02	0.33	11416	230	194	9.03	2	BL
J090754-482422	T30	269.590	-0.553	0.003	0.38	0.05	0.28	11753	154	69	9.41	1*	
J090756-482311	T30	269.580	-0.535	0.002	0.15	0.03	0.29	13320	223	139	9.10	2*	
J090812-480306	T30	269.364	-0.276	0.003	0.30	0.04	0.27	23590	318	62	9.91	2	
J090813-471517	T31	268.779	0.266	0.021	2.82	0.40	0.34	7426	176	176	9.88	1	
J090815-484027	T30	269.829	-0.690	0.002	0.19	0.03	0.27	13060	215	198	9.19	1*	
J090818-490253	T30	270.109	-0.938	0.005	0.45	0.06	0.27	14638	169	149	9.67	1	
J090831-484919	T30	269.967	-0.758	0.004	0.64	0.09	0.29	13063	314	220	9.73	1	w.comp (J090847-484916)
J090837-462740	T31	268.243	0.855	0.009	0.68	0.10	0.60	14299	194	117	9.84	2	
J090847-484916	T30	269.995	-0.726	0.005	0.65	0.12	0.28	13350	619	569	9.76	1	w.comp (J090831-484919), M, W
J090851-470752	T31	268.761	0.428	0.030	2.18	0.22	0.34	15066	165	69	10.39	1	M, W
J090852-481924	T30	269.639	-0.378	0.004	0.32	0.08	0.27	13999	193	104	9.49	1*	
J090853-474727	T31	269.251	-0.014	0.015	2.75	0.39	0.33	7205	305	279	9.84	1	M, W
J090907-492111	T30	270.424	-1.046	0.005	0.37	0.07	0.29	2751	181	27	8.13	2	
J090923-482937	T30	269.823	-0.430	0.034	8.22	0.81	0.31	6558	326	275	10.24	1*	J0909-48A
J090944-465316	T31	268.685	0.704	0.009	0.80	0.11	0.42	6525	164	148	9.22	1	
J090952-473855	T31	269.258	0.203	0.004	0.31	0.04	0.30	12943	248	120	9.41	2	
J090952-482335	T30	269.803	-0.303	0.003	0.29	0.04	0.27	11913	175	137	9.31	1*	w.comp (J090958-482533)
J090955-481005	T30	269.644	-0.145	0.029	4.30	0.61	0.30	2740	187	142	9.19	1*	J0909-48B
J090955-493550	T30	270.691	-1.117	0.006	0.88	0.13	0.31	6745	217	177	9.29	1	
J090958-482533	T30	269.838	-0.314	0.006	0.70	0.10	0.28	11879	246	195	9.69	1*	w.comp (J090952-482335)
J091001-495746	T30	270.970	-1.354	0.008	0.64	0.09	0.33	7844	229	176	9.28	1	Hole in the middle of MOM1

* Detected by the overlapping region of the next mosaic as well.

Table C1 continued

Name	Mosaic	l	b	S_{peak}	S_{int}	ϵ_S	rms	V_{hel}	w_{20}	w_{50}	M_{HI}	Flag	Note
J2000	TXX	deg	deg	Jy	Jy km s ⁻¹	Jy km s ⁻¹	mJy beam ⁻¹	km s ⁻¹	km s ⁻¹	km s ⁻¹	log(M_{HI}/M_{\odot})	1/2	(14)
(1)	(2)	(3)	(4)	(5)	(6)	(7)	(8)	(9)	(10)	(11)	(12)	(13)	(14)
J091001-495256	T30	270.912	-1.298	0.005	0.54	0.08	0.30	14824	213	154	9.77	1	
J091008-484117	T30	270.049	-0.472	0.005	0.79	0.11	0.28	14840	322	317	9.93	1	
J091008-485410	T30	270.207	-0.617	0.003	0.25	0.04	0.27	11696	135	90	9.22	1	
J091017-504030	T30	271.521	-1.808	0.007	0.52	0.10	0.44	5329	115	79	8.86	1	
J091033-495915	T30	271.046	-1.308	0.005	0.37	0.05	0.30	14824	175	153	9.60	1	
J091037-492044	T30	270.585	-0.862	0.003	0.32	0.05	0.27	13422	167	147	9.45	1	
J091104-474016	T30	269.412	0.335	0.002	0.10	0.02	0.31	7329	116	87	8.41	2	
J091105-492122	T30	270.644	-0.814	0.005	1.61	0.16	0.27	13689	658	615	10.16	1	w.comp
J091117-480529	T30	269.744	0.075	0.005	0.83	0.12	0.29	14202	227	227	9.91	1*	
J091127-485110	T30	270.318	-0.426	0.004	0.39	0.06	0.27	13992	201	163	9.58	1	
J091138-484641	T30	270.284	-0.352	0.003	0.22	0.03	0.26	14001	149	89	9.34	2	
J091143-484129	T30	270.230	-0.284	0.005	1.09	0.11	0.28	14005	324	248	10.02	1	
J091153-501751	T30	271.418	-1.365	0.004	0.28	0.04	0.31	11287	161	107	9.24	1	
J091155-494040	T30	270.972	-0.935	0.003	0.73	0.10	0.27	14568	353	306	9.88	1	
J091212-494148	T30	271.017	-0.914	0.002	0.21	0.03	0.27	14253	205	155	9.31	2	w.comp (J091155-494040)
J091213-483248	T30	270.182	-0.123	0.004	0.31	0.04	0.27	13999	213	159	9.48	1	
J091218-492335	T30	270.806	-0.696	0.005	0.53	0.08	0.28	6684	153	118	9.06	1	
J091218-482237	T30	270.068	0.003	0.005	0.98	0.10	0.27	15031	408	385	10.04	1	M, W
J091226-494559	T30	271.093	-0.936	0.002	0.17	0.02	0.25	14169	152	120	9.21	2	w.comp (J091234-494502)
J091234-494502	T30	271.096	-0.909	0.006	0.49	0.07	0.27	14381	407	262	9.69	2	w.comps (J091155, J091212 and J091226)
J091234-492735	T30	270.885	-0.709	0.004	0.38	0.07	0.28	6699	198	158	8.91	1	
J091245-500241	T30	271.331	-1.089	0.005	0.43	0.04	0.27	22459	178	142	10.04	1	
J091252-483837	T30	270.325	-0.113	0.003	0.26	0.04	0.26	21824	226	186	9.79	1	
J091304-492224	T30	270.878	-0.591	0.004	0.34	0.05	0.27	13941	187	80	9.50	2	
J091309-503303	T30	271.742	-1.392	0.003	0.18	0.03	0.29	17970	127	106	9.47	1	
J091310-483138	T30	270.276	0.004	0.003	0.21	0.03	0.27	14019	173	158	9.30	2	
J091327-492401	T30	270.940	-0.564	0.005	0.37	0.05	0.26	23811	223	161	10.03	2	
J091330-473234	T30	269.601	0.722	0.006	0.62	0.09	0.36	13726	216	164	9.76	1*	
J091336-503146	T30	271.775	-1.326	0.011	1.75	0.25	0.34	8222	334	284	9.76	1	
J091344-504624	T30	271.966	-1.478	0.004	0.35	0.05	0.33	11959	143	86	9.39	1	
J091354-482529	T30	270.284	0.161	0.009	1.42	0.20	0.29	6360	245	206	9.45	1	J0913-48 (blended HIZOA detection), M, W, Z
J091356-491507	T30	270.887	-0.405	0.004	0.45	0.06	0.26	19739	209	173	9.94	1	
J091403-492707	T30	271.045	-0.530	0.005	0.33	0.06	0.29	7373	179	133	8.94	1	
J091404-485216	T30	270.626	-0.127	0.005	0.31	0.04	0.26	14135	152	79	9.48	1	
J091405-472109	T30	269.531	0.926	0.012	2.38	0.23	0.53	11587	462	307	10.19	1*	M
J091407-475312	T30	269.922	0.561	0.006	0.61	0.09	0.33	16040	268	253	9.89	1	
J091410-494602	T30	271.286	-0.734	0.004	0.18	0.03	0.27	24845	192	161	9.74	2	
J091410-482229	T30	270.280	0.229	0.016	3.19	0.45	0.30	6404	248	217	9.80	1	J0913-48 (blended HIZOA detection)
J091416-491341	T30	270.908	-0.349	0.007	1.49	0.21	0.27	11801	272	205	10.01	1	
J091429-483621	T30	270.483	0.107	0.004	0.54	0.08	0.27	14167	256	204	9.72	1	
J091439-474438	T30	269.880	0.724	0.004	0.20	0.03	0.38	14186	161	121	9.30	1*	
J091441-492511	T30	271.093	-0.432	0.005	0.46	0.06	0.28	8979	117	102	9.26	1	
J091446-501010	T30	271.643	-0.943	0.004	0.15	0.03	0.27	11264	66	26	8.97	1	
J091455-474530	T30	269.922	0.747	0.008	0.68	0.10	0.42	14994	191	126	9.88	1	
J091458-491219	T30	270.971	-0.250	0.005	0.30	0.04	0.26	11874	112	52	9.32	1	
J091500-491522	T30	271.011	-0.282	0.002	0.34	0.05	0.26	10618	343	297	9.27	1	i
J091506-500015	T30	271.561	-0.789	0.003	0.23	0.04	0.28	7562	335	276	8.80	2	
J091514-483634	T30	270.570	0.193	0.021	2.76	0.27	0.30	9711	185	106	10.10	1	J0915-48
J091520-480644	T30	270.224	0.550	0.003	0.43	0.06	0.35	11505	214	168	9.45	1	
J091525-474154	T30	269.936	0.847	0.035	2.50	0.36	0.57	7280	128	55	9.81	1	J0915-47
J091537-480949	T30	270.294	0.548	0.011	1.57	0.15	0.34	19773	315	296	10.48	1	
J091537-491950	T30	271.134	-0.262	0.007	0.57	0.06	0.26	22452	153	96	10.15	1	
J091543-482610	T30	270.502	0.372	0.006	0.31	0.04	0.28	17001	112	74	9.64	1	
J091547-510222	T29	272.383	-1.428	0.005	0.48	0.07	0.30	10905	120	104	9.45	1*	NaN
J091554-510251	T29	272.401	-1.421	0.004	0.38	0.05	0.29	19732	499	477	9.87	1*	
J091556-490111	T30	270.946	-0.009	0.002	0.09	0.01	0.24	22484	78	58	9.35	2	
J091558-492057	T30	271.188	-0.233	0.005	0.26	0.05	0.27	7323	106	50	8.83	2	
J091605-480639	T30	270.311	0.642	0.003	0.12	0.02	0.35	9670	106	70	8.75	1	
J091609-510253	T29	272.428	-1.394	0.008	1.86	0.18	0.29	10772	395	365	10.02	1*	NaN
J091630-493522	T30	271.420	-0.338	0.005	1.03	0.15	0.27	13952	519	379	10.00	1	i
J091641-484532	T30	270.845	0.262	0.001	0.22	0.03	0.27	14098	201	141	9.33	2	
J091641-494721	T30	271.585	-0.455	0.002	0.16	0.02	0.25	13781	164	139	9.16	1	
J091718-492515	T30	271.391	-0.126	0.027	5.84	0.58	0.29	7537	325	259	10.21	1	J0917-49, i, w.comp, I, M, W, Z
J091728-515713	T29	273.222	-1.877	0.006	0.23	0.03	0.60	10466	218	182	9.09	1	
J091745-480943	T30	270.541	0.805	0.031	5.17	0.73	0.44	3337	244	211	9.44	1	J0917-48
J091747-490507	T30	271.205	0.164	0.002	0.24	0.03	0.26	17340	258	224	9.55	1	w.comp
J091755-502411	T30	272.161	-0.744	0.003	0.41	0.06	0.27	12166	490	453	9.48	1	M, W
J091756-494530	T30	271.704	-0.289	0.003	0.47	0.07	0.27	14026	241	198	9.66	1	
J091801-505621	T29	272.556	-1.106	0.003	0.29	0.04	0.27	10788	215	166	9.23	1*	
J091803-502335	T30	272.169	-0.721	0.005	0.41	0.06	0.26	17918	126	108	9.81	1	
J091820-510310	T29	272.671	-1.152	0.009	1.33	0.19	0.29	8536	177	161	9.68	1*	
J091828-503349	T29	272.338	-0.793	0.005	0.25	0.05	0.28	8267	79	79	8.93	1*	
J091840-501737	T30	272.168	-0.580	0.002	0.19	0.03	0.25	19840	200	137	9.56	1	
J091858-503324	T29	272.388	-0.732	0.005	0.66	0.07	0.27	19859	217	154	10.11	1*	
J091900-505249	T29	272.622	-0.956	0.003	0.08	0.02	0.26	12317	226	106	8.80	1*	
J091902-484000	T30	271.051	0.604	0.006	0.49	0.07	0.38	7170	201	139	9.09	1	
J091907-494203	T30	271.796	-0.113	0.004	0.26	0.04	0.25	22394	267	220	9.81	1	
J091908-502743	T30	272.339	-0.647	0.004	0.23	0.03	0.25	18438	155	97	9.59	1	

* Detected by the overlapping region of the next mosaic as well.

Table C1 continued

Name	Mosaic	l	b	S_{peak}	S_{int}	ε_S	rms	V_{hel}	w_{20}	w_{50}	M_{HI}	Flag	Note
J2000	TXX	deg	deg	Jy	Jy km s ⁻¹	Jy km s ⁻¹	mJy beam ⁻¹	km s ⁻¹	km s ⁻¹	km s ⁻¹	log(M_{HI}/M_{\odot})	1/2	(14)
(1)	(2)	(3)	(4)	(5)	(6)	(7)	(8)	(9)	(10)	(11)	(12)	(13)	(14)
J091917-494513	T30	271.853	-0.131	0.004	1.02	0.15	0.26	14070	351	320	10.00	1	i, M, W
J091924-515723	T29	273.431	-1.668	0.009	1.07	0.15	0.39	10478	199	168	9.76	1	M, W
J091925-500852	T30	272.148	-0.393	0.004	0.28	0.04	0.25	19857	159	96	9.73	1	
J091930-510118	T29	272.778	-0.998	0.003	0.10	0.02	0.28	7269	72	54	8.40	1*	
J091937-513048	T29	273.141	-1.331	0.003	0.18	0.03	0.29	10579	116	95	8.99	1	
J091952-511718	T29	273.008	-1.146	0.004	0.34	0.05	0.29	8686	152	120	9.10	1	
J092001-500209	T30	272.135	-0.247	0.003	0.30	0.04	0.26	12146	212	173	9.34	1	
J092006-511054	T29	272.958	-1.044	0.003	0.36	0.05	0.26	22968	413	363	9.98	2	
J092012-483336	T30	271.110	0.815	0.009	0.66	0.09	0.53	11339	143	92	9.62	1	
J092025-512218	T29	273.128	-1.143	0.004	0.29	0.04	0.28	12498	152	108	9.35	1	
J092055-493541	T30	271.927	0.169	0.027	2.14	0.21	0.26	11003	129	53	10.10	1	J0920-49, i
J092114-504633	T29	272.797	-0.631	0.007	0.55	0.08	0.29	12409	131	131	9.62	1*	w.comp
J092123-504955	T29	272.853	-0.655	0.005	0.53	0.08	0.28	7192	275	52	9.13	2	
J092127-515408	T29	273.616	-1.405	0.005	0.49	0.09	0.31	4016	161	130	8.58	1	
J092129-483248	T30	271.251	0.975	0.012	0.67	0.30	0.77	9394	486	326	9.46	2	
J092137-490410	T30	271.635	0.619	0.013	1.39	0.20	0.33	9264	171	156	9.77	1	
J092137-485233	T30	271.499	0.757	0.014	2.32	0.23	0.38	11221	351	317	10.16	1	
J092137-500628	T29	272.368	-0.115	0.003	0.18	0.02	0.25	11246	122	106	9.04	1*	
J092143-514632	T29	273.556	-1.286	0.003	0.19	0.03	0.28	11291	174	104	9.08	1	
J092146-490555	T30	271.673	0.617	0.005	0.32	0.05	0.30	11273	259	49	9.30	1	
J092154-502919	T29	272.668	-0.354	0.011	1.43	0.14	0.27	12208	196	122	10.02	1*	i
J092206-514715	T29	273.606	-1.254	0.006	0.36	0.07	0.30	6644	84	34	8.89	2	
J092213-503257	T29	272.747	-0.361	0.008	1.05	0.15	0.28	5861	175	163	9.24	1*	
J092227-520157	T29	273.818	-1.388	0.003	0.22	0.04	0.29	20809	298	267	9.68	2	
J092231-490341	T30	271.735	0.730	0.009	0.56	0.08	0.40	9396	153	85	9.38	1	
J092231-495120	T30	272.294	0.166	0.004	0.42	0.06	0.27	7378	216	150	9.04	1*	
J092233-494226	T30	272.192	0.275	0.006	1.32	0.13	0.26	20969	514	267	10.46	1	
J092236-510400	T29	273.155	-0.686	0.004	0.73	0.10	0.33	12166	309	274	9.72	1	
J092248-500445	T29	272.484	0.039	0.004	0.35	0.05	0.26	14019	225	208	9.53	1*	
J092251-491135	T30	271.865	0.674	0.004	0.38	0.05	0.34	23095	120	79	10.00	1	
J092253-495827	T29	272.419	0.123	0.020	1.46	0.21	0.27	7384	100	40	9.59	1*	
J092257-495856	T29	272.431	0.124	0.003	0.19	0.03	0.25	20607	290	67	9.60	1*	
J092320-500423	T29	272.540	0.103	0.005	0.38	0.05	0.26	13966	131	90	9.56	1*	
J092339-502642	T29	272.837	-0.126	0.004	0.13	0.02	0.24	21856	123	101	9.50	1	
J092340-494740	T29	272.382	0.339	0.006	0.60	0.09	0.27	9237	176	159	9.40	1*	
J092340-491154	T30	271.965	0.765	0.009	1.01	0.14	0.44	11289	238	140	9.80	1	
J092344-514805	T29	273.796	-1.086	0.003	0.18	0.03	0.28	20689	117	87	9.59	1	
J092413-524651	T29	274.535	-1.733	0.004	0.22	0.04	0.37	23912	473	192	9.79	1	
J092428-503201	T29	272.990	-0.100	0.014	2.26	0.32	0.28	6523	211	180	9.67	1	
J092502-503253	T29	273.065	-0.047	0.002	0.18	0.03	0.25	11175	119	53	9.04	2	
J092508-514441	T29	273.911	-0.894	0.005	0.54	0.08	0.32	12638	165	114	9.63	1	
J092513-504721	T29	273.255	-0.198	0.011	1.22	0.17	0.29	10726	178	136	9.84	1	
J092522-503238	T29	273.101	-0.006	0.002	0.14	0.02	0.25	13968	163	122	9.13	1	
J092541-495937	T29	272.755	0.424	0.003	0.09	0.02	0.26	12347	176	119	8.84	2*	
J092551-512031	T29	273.711	-0.526	0.007	0.53	0.08	0.33	19869	174	134	10.02	1	
J092557-514513	T29	274.009	-0.811	0.003	0.09	0.01	0.29	20974	82	69	9.30	1	
J092615-525114	T29	274.806	-1.571	0.006	0.62	0.06	0.36	20872	189	131	10.13	1	
J092615-523237	T29	274.591	-1.348	0.031	6.48	0.64	0.37	7059	371	323	10.20	1	J0926-52, M, W
J092627-505440	T29	273.480	-0.151	0.007	0.48	0.10	0.35	6276	195	102	8.97	1	
J092655-514801	T29	274.148	-0.742	0.003	0.22	0.03	0.28	22441	313	282	9.74	2	
J092658-512442	T29	273.884	-0.456	0.005	0.46	0.07	0.32	15838	177	136	9.76	1	
J092715-495524	T29	272.887	0.650	0.034	6.60	0.94	0.38	4515	211	197	9.81	1	J0927-49
J092717-511426	T29	273.802	-0.298	0.003	0.21	0.06	0.29	19930	255	163	9.64	2	
J092728-522455	T29	274.635	-1.127	0.007	0.90	0.13	0.33	7061	170	132	9.34	1	
J092733-520133	T29	274.375	-0.836	0.002	0.19	0.03	0.28	18455	293	167	9.49	2	
J092807-503741	T29	273.473	0.235	0.019	4.76	0.68	0.29	2910	255	239	9.29	1	J0927-50
J092816-494613	T29	272.899	0.873	0.006	0.29	0.05	0.51	8322	79	79	8.99	1	
J092829-530538	T29	275.215	-1.512	0.003	0.25	0.05	0.33	6913	168	81	8.77	1	
J092903-524320	T29	275.021	-1.183	0.014	2.00	0.28	0.31	4496	200	168	9.29	1	
J092909-523748	T29	274.969	-1.106	0.002	0.30	0.04	0.27	12505	279	254	9.37	2	i
J092911-523359	T29	274.929	-1.056	0.003	0.42	0.06	0.27	20595	223	127	9.94	2	
J092921-531251	T28	275.392	-1.509	0.010	0.96	0.18	0.31	3988	205	159	8.87	1*	
J092930-524018	T29	275.036	-1.100	0.003	0.36	0.05	0.27	12384	185	124	9.43	1	
J092937-512341	T29	274.172	-0.159	0.002	0.24	0.03	0.27	16035	169	74	9.48	2	
J092942-512211	T29	274.165	-0.131	0.011	0.55	0.10	0.26	6129	70	25	9.00	1	
J092944-515926	T29	274.594	-0.580	0.007	0.32	0.06	0.31	2951	97	46	8.14	1	
J092948-524044	T29	275.074	-1.073	0.004	0.26	0.04	0.26	14375	248	173	9.41	2	
J092949-503730	T29	273.668	0.424	0.003	0.17	0.03	0.28	7484	106	67	8.68	1	
J092954-513113	T29	274.290	-0.220	0.002	0.12	0.02	0.25	21027	199	117	9.41	2	
J093002-531530	T28	275.497	-1.472	0.003	0.14	0.02	0.26	17477	133	35	9.33	2*	
J093008-503351	T29	273.663	0.502	0.003	0.10	0.01	0.26	19550	75	55	9.26	1	
J093009-510014	T29	273.966	0.184	0.003	0.39	0.05	0.26	17137	323	221	9.75	2	
J093035-531813	T28	275.589	-1.447	0.002	0.19	0.03	0.24	17303	203	113	9.44	1*	
J093039-531910	T28	275.606	-1.452	0.003	0.55	0.05	0.26	21334	287	213	10.10	1	
J093039-530847	T28	275.488	-1.326	0.004	0.19	0.03	0.25	17489	86	55	9.45	1*	
J093041-521723	T29	274.906	-0.698	0.003	0.22	0.04	0.27	4148	321	242	8.26	2	
J093054-530808	T28	275.507	-1.293	0.002	0.28	0.04	0.25	21191	563	200	9.80	2*	
J093105-533944	T28	275.888	-1.658	0.003	0.19	0.03	0.37	21846	82	82	9.65	1	

* Detected by the overlapping region of the next mosaic as well.

Table C1 continued

Name	Mosaic	l	b	S_{peak}	S_{int}	ϵ_s	rms	V_{hel}	w_{20}	w_{50}	M_{HI}	Flag	Note
J2000	TXX	deg	deg	Jy	Jy km s ⁻¹	Jy km s ⁻¹	mJy beam ⁻¹	km s ⁻¹	km s ⁻¹	km s ⁻¹	log(M_{HI}/M_{\odot})	1/2	(14)
(1)	(2)	(3)	(4)	(5)	(6)	(7)	(8)	(9)	(10)	(11)	(12)	(13)	(14)
J093113-515814	T29	274.748	-0.408	0.006	0.53	0.10	0.30	5320	128	90	8.86	1	
J093129-523512	T29	275.198	-0.831	0.002	0.29	0.05	0.26	7024	176	142	8.85	2	
J093132-525730	T28	275.456	-1.099	0.002	0.19	0.03	0.29	17107	228	45	9.45	2*	
J093140-504601	T29	273.978	0.519	0.008	0.32	0.06	0.33	4480	65	20	8.49	1	
J093140-511548	T29	274.317	0.157	0.004	0.24	0.03	0.25	17203	210	72	9.55	1	
J093146-511747	T29	274.350	0.143	0.006	0.96	0.10	0.26	17152	354	228	10.15	1	
J093147-514939	T29	274.713	-0.245	0.008	2.96	0.29	0.30	12038	616	578	10.32	1	M, W
J093156-510619	T29	274.240	0.301	0.003	0.19	0.03	0.25	17277	213	81	9.45	1	
J093203-512355	T29	274.452	0.098	0.003	0.19	0.04	0.24	18869	249	127	9.52	2	i
J093213-513627	T29	274.614	-0.037	0.004	0.34	0.05	0.26	17078	262	184	9.69	1	
J093214-510300	T29	274.237	0.373	0.037	6.93	0.98	0.29	4533	269	195	9.84	1	J0932-51, i, I, M, Z
J093216-515945	T29	274.884	-0.316	0.008	0.71	0.13	0.28	5326	111	76	8.99	1	
J093231-523634	T28	275.328	-0.741	0.007	0.96	0.09	0.24	17598	322	306	10.17	1*	
J093240-510358	T29	274.298	0.408	0.004	0.21	0.03	0.25	21557	134	71	9.68	1	
J093245-505416	T29	274.197	0.535	0.002	0.43	0.06	0.28	21755	424	405	10.01	1	
J093256-524235	T28	275.442	-0.772	0.004	0.12	0.02	0.28	23305	121	41	9.52	2	
J093258-522817	T28	275.285	-0.593	0.002	0.25	0.04	0.29	15726	294	168	9.48	2*	
J093259-510439	T29	274.341	0.432	0.002	0.13	0.02	0.25	21354	134	115	9.48	1	
J093305-524517	T28	275.490	-0.789	0.002	0.22	0.04	0.27	6878	152	104	8.71	2	
J093320-504400	T29	274.149	0.723	0.005	0.33	0.05	0.36	21446	329	252	9.88	1	
J093327-525749	T28	275.672	-0.906	0.002	0.13	0.02	0.27	13159	124	104	9.06	2*	
J093353-510516	T29	274.452	0.521	0.009	0.47	0.11	0.27	4422	72	26	8.65	1	
J093353-525541	T28	275.696	-0.836	0.003	0.13	0.02	0.25	12769	295	245	9.02	2	
J093400-540801	T28	276.523	-1.713	0.005	0.35	0.05	0.34	17295	264	134	9.71	2	
J093401-534017	T28	276.213	-1.370	0.002	0.12	0.02	0.27	13899	122	107	9.04	1	
J093414-510521	T29	274.493	0.556	0.003	0.31	0.04	0.27	19471	253	169	9.77	1	w.comp
J093419-505455	T29	274.386	0.694	0.004	0.34	0.06	0.32	7176	286	224	8.93	2	w.comp?
J093426-525227	T28	275.721	-0.740	0.003	0.40	0.06	0.29	17140	282	225	9.77	1*	
J093430-515708	T29	275.107	-0.052	0.002	0.13	0.02	0.24	17832	179	162	9.31	1	
J093438-523942	T28	275.599	-0.563	0.003	0.21	0.03	0.28	13095	166	147	9.24	1*	w.comp (J093441-523744)
J093441-523744	T28	275.584	-0.533	0.005	0.87	0.12	0.27	13138	299	256	9.87	1*	w.comp (J093438-523942)
J093443-504536	T29	274.329	0.852	0.005	0.50	0.07	0.45	6703	249	209	9.04	2	
J093451-510739	T29	274.592	0.594	0.004	0.19	0.03	0.28	12727	121	90	9.19	1	
J093509-520622	T29	275.284	-0.099	0.003	0.26	0.04	0.25	17816	381	133	9.61	1	
J093512-521335	T28	275.371	-0.182	0.008	0.40	0.06	0.28	8213	69	24	9.12	2	
J093513-522238	T28	275.474	-0.292	0.002	0.08	0.01	0.27	20219	156	26	9.24	2	
J093515-523442	T28	276.174	-1.054	0.005	0.26	0.04	0.26	13878	165	58	9.39	1	w.comp
J093522-531928	T28	276.127	-0.980	0.002	0.18	0.03	0.27	17192	228	210	9.43	1	
J093554-515009	T29	275.189	0.180	0.002	0.14	0.02	0.25	17645	182	127	9.33	2	
J093621-521128	T28	275.478	-0.038	0.006	0.47	0.09	0.28	5742	112	60	8.88	1*	
J093624-514546	T29	275.196	0.285	0.003	0.27	0.04	0.26	22442	184	162	9.83	1	
J093624-531326	T28	276.174	-0.801	0.004	0.33	0.05	0.24	21783	378	292	9.90	2	
J093626-520845	T28	275.456	0.003	0.002	0.24	0.05	0.27	8617	164	145	8.94	2*	
J093638-541538	T28	276.894	-1.548	0.007	0.41	0.06	0.33	7962	152	103	9.10	1	
J093638-543723	T28	277.137	-1.817	0.093	10.74	1.52	0.58	2734	162	102	9.59	1	J0936-54
J093640-522905	T28	275.710	-0.224	0.003	0.24	0.03	0.24	21281	184	160	9.72	1	i?
J093642-533923	T28	276.498	-1.091	0.008	0.53	0.08	0.29	8885	111	78	9.31	1	
J093643-520914	T28	275.494	0.027	0.003	0.23	0.03	0.26	11692	130	130	9.19	1*	
J093652-520737	T28	275.495	0.063	0.014	1.47	0.21	0.28	6344	149	100	9.46	1*	
J093653-543036	T28	277.087	-1.709	0.003	0.22	0.03	0.37	19394	130	74	9.61	1	
J093745-523439	T28	275.894	-0.184	0.006	0.82	0.12	0.27	13280	408	262	9.85	1	
J093750-540431	T28	276.901	-1.293	0.005	0.19	0.03	0.30	19294	192	54	9.55	1	
J093800-542441	T28	277.144	-1.527	0.004	0.78	0.08	0.30	22072	420	401	10.28	1	
J093814-520318	T28	275.603	0.256	0.003	0.33	0.05	0.29	19998	134	134	9.82	1*	
J093830-532009	T28	276.483	-0.675	0.003	0.10	0.02	0.26	8867	79	58	8.59	2	
J093835-540554	T28	276.999	-1.237	0.004	0.19	0.03	0.28	12340	164	132	9.16	2	
J093838-513506	T28	275.337	0.649	0.007	0.77	0.11	0.31	11703	178	152	9.72	1*	
J093843-522553	T28	275.908	0.024	0.009	0.79	0.11	0.26	5764	159	60	9.10	1	
J093906-512449	T29	275.278	0.825	0.004	0.28	0.03	0.42	11512	341	204	9.26	1*	
J093907-535208	T28	276.906	-1.013	0.009	1.04	0.15	0.28	7830	175	123	9.49	1	
J093912-533731	T28	276.753	-0.822	0.016	2.98	0.42	0.28	2876	230	185	9.08	1	J0938-53, W, Z
J093924-515551	T28	275.655	0.468	0.002	0.18	0.03	0.27	11794	213	173	9.10	2*	
J094035-522115	T28	276.071	0.270	0.005	0.76	0.11	0.26	13332	260	175	9.82	1	
J094047-534324	T28	276.994	-0.741	0.003	0.28	0.04	0.25	16796	188	137	9.59	1	
J094052-541056	T28	277.305	-1.079	0.002	0.19	0.03	0.26	16272	191	167	9.40	2	
J094053-515144	T28	275.780	0.670	0.005	0.28	0.04	0.34	17847	109	78	9.64	1*	
J094056-541601	T28	277.369	-1.136	0.004	0.09	0.02	0.28	9499	88	60	8.59	1	
J094104-522012	T28	276.115	0.332	0.005	0.57	0.08	0.27	19380	358	326	10.03	1	
J094113-521440	T28	276.071	0.416	0.013	1.06	0.15	0.30	6331	119	61	9.31	1	
J094115-525806	T28	276.550	-0.126	0.003	0.20	0.03	0.25	17015	266	91	9.46	1	
J094131-535218	T28	277.173	-0.782	0.003	0.36	0.05	0.30	19282	357	25	9.82	2	
J094137-540349	T28	277.311	-0.917	0.004	0.57	0.06	0.26	19461	237	187	10.03	1	
J094142-520341	T28	276.008	0.604	0.007	0.74	0.14	0.36	5298	155	122	9.01	1	w.comp (J094157-520308)
J094148-523056	T28	276.316	0.269	0.004	0.80	0.08	0.26	17534	218	184	10.09	1	
J094148-540703	T28	277.366	-0.940	0.003	0.32	0.04	0.27	19442	317	282	9.77	1	
J094157-520308	T28	276.029	0.635	0.003	0.18	0.03	0.35	5355	96	57	8.40	1	
J094200-531607	T28	276.832	-0.280	0.004	0.32	0.06	0.27	6761	128	117	8.85	1	
J094210-524930	T28	276.561	0.073	0.002	0.24	0.03	0.22	22092	289	244	9.77	2	

* Detected by the overlapping region of the next mosaic as well.

Table C1 continued

Name	Mosaic	l	b	S_{peak}	S_{int}	ϵ_S	rms	V_{hel}	w_{20}	w_{50}	M_{HI}	Flag	Note
J2000	TXX	deg	deg	Jy	Jy km s ⁻¹	Jy km s ⁻¹	mJy beam ⁻¹	km s ⁻¹	km s ⁻¹	km s ⁻¹	log(M_{HI}/M_{\odot})	1/2	(14)
(1)	(2)	(3)	(4)	(5)	(6)	(7)	(8)	(9)	(10)	(11)	(12)	(13)	(14)
J094212-542646	T28	277.626	-1.150	0.003	0.38	0.05	0.23	14334	262	214	9.58	2	
J094215-532618	T28	276.971	-0.384	0.007	0.53	0.07	0.25	19435	310	58	9.99	1	
J094225-522520	T28	276.327	0.402	0.009	1.37	0.19	0.28	6849	202	172	9.50	1	
J094235-524304	T28	276.538	0.194	0.010	0.59	0.11	0.26	4509	106	68	8.77	1	
J094239-532824	T28	277.040	-0.370	0.002	0.20	0.03	0.24	21863	324	185	9.67	2	
J094308-522041	T28	276.359	0.533	0.002	0.13	0.05	0.28	24679	503	464	9.61	2	NaN
J094310-530512	T28	276.845	-0.028	0.004	0.49	0.07	0.26	19777	253	175	9.98	1	
J094311-552945	T27	278.418	-1.853	0.007	1.57	0.22	0.41	11344	457	375	10.00	1*	
J094317-530347	T28	276.843	0.002	0.003	0.59	0.08	0.27	13853	475	425	9.74	1	M
J094319-534009	T28	277.243	-0.454	0.002	0.21	0.03	0.26	21841	242	67	9.69	2	
J094339-523637	T28	276.591	0.382	0.002	0.27	0.04	0.26	19740	245	125	9.72	2	
J094343-533456	T28	277.231	-0.350	0.004	0.23	0.03	0.30	19418	98	48	9.63	2	
J094356-552847	T27	278.487	-1.773	0.005	0.29	0.04	0.36	12118	142	85	9.31	1*	
J094359-533458	T27	278.561	-1.845	0.010	0.79	0.11	0.41	12114	310	288	9.76	1*	
J094423-522603	T28	276.562	0.588	0.003	0.30	0.04	0.28	13881	146	98	9.45	1	w.comp (J094436-523539)
J094425-532714	T28	277.227	-0.184	0.004	0.28	0.04	0.25	19591	250	166	9.72	1	
J094430-533031	T27	278.568	-1.742	0.006	0.60	0.09	0.34	12182	130	130	9.64	1*	
J094430-545453	T28	278.184	-1.289	0.002	0.16	0.02	0.27	13191	181	86	9.13	2	
J094436-523539	T28	276.690	0.488	0.005	0.44	0.06	0.29	13853	153	108	9.62	1	w.comp (J094423-522603)
J094445-524813	T28	276.843	0.343	0.007	0.63	0.12	0.28	4507	165	99	8.79	1	i
J094449-530629	T28	277.047	0.117	0.028	4.18	0.59	0.28	5701	199	161	9.82	1	J0944-53, W, Z
J094504-545459	T27	278.246	-1.237	0.003	0.17	0.02	0.26	13235	212	114	9.17	1*	
J094527-531914	T28	277.258	0.016	0.002	0.11	0.02	0.28	21985	275	122	9.41	2	
J094530-524441	T28	276.891	0.460	0.001	0.09	0.01	0.29	19634	107	56	9.24	2	
J094530-523757	T28	276.819	0.546	0.003	0.29	0.04	0.30	16622	395	335	9.59	2	
J094535-543357	T28	278.077	-0.922	0.006	0.40	0.13	0.26	2215	126	27	7.98	2	
J094541-540631	T28	277.792	-0.564	0.002	0.16	0.02	0.23	16652	165	141	9.34	1	
J094543-535448	T28	277.670	-0.411	0.003	0.11	0.02	0.25	13987	163	100	9.04	2	
J094552-532617	T28	277.380	-0.034	0.005	0.59	0.11	0.28	2717	193	75	8.33	1	
J094605-555133	T27	278.965	-1.864	0.008	0.77	0.11	0.58	11965	214	184	9.74	1	
J094609-540336	T28	277.813	-0.482	0.003	0.22	0.03	0.27	14018	180	31	9.32	2	
J094620-553842	T27	278.854	-1.679	0.011	0.69	0.13	0.38	4883	126	65	8.90	1	
J094621-531930	T28	277.363	0.099	0.010	0.88	0.16	0.25	1699	105	73	8.09	1	
J094629-522925	T28	276.842	0.752	0.005	0.34	0.05	0.37	16539	163	126	9.66	1	
J094630-542620	T28	278.097	-0.739	0.008	0.58	0.11	0.26	2230	104	66	8.14	1	
J094646-542636	T28	278.129	-0.718	0.004	0.37	0.07	0.27	5355	118	99	8.71	1	
J094650-530910	T28	277.308	0.277	0.003	0.37	0.05	0.23	19634	219	170	9.86	1	
J094706-554932	T27	279.052	-1.748	0.003	0.16	0.02	0.42	14061	163	129	9.19	2	
J094720-550816	T27	278.637	-1.198	0.003	0.30	0.04	0.25	10818	180	89	9.23	1*	
J094725-530220	T28	277.303	0.422	0.004	0.20	0.03	0.25	19626	104	51	9.58	1	
J094730-550328	T27	278.604	-1.122	0.003	0.14	0.03	0.26	10869	80	61	8.91	1*	
J094738-533707	T28	277.697	-0.004	0.001	0.22	0.03	0.25	19985	302	260	9.63	2	
J094739-533809	T28	277.711	-0.015	0.004	0.80	0.08	0.24	16643	409	352	10.04	1	
J094745-545318	T27	278.523	-0.968	0.002	0.16	0.02	0.26	11642	140	76	9.03	1*	
J094751-544722	T27	278.471	-0.883	0.005	0.25	0.03	0.26	19989	196	84	9.69	1*	i?
J094758-543619	T27	278.366	-0.731	0.070	9.19	1.30	0.27	1721	117	103	9.12	1*	J0947-54, H
J094800-545708	T27	278.592	-0.995	0.005	0.59	0.11	0.27	5390	168	130	8.92	1*	
J094816-550531	T27	278.710	-1.078	0.003	0.25	0.04	0.26	12057	308	291	9.25	1*	
J094833-541400	T28	278.194	-0.391	0.003	0.13	0.02	0.26	21237	166	60	9.45	2	
J094921-531819	T28	277.696	0.402	0.006	1.00	0.10	0.31	20037	491	442	10.30	1	w.comp
J094926-534126	T28	277.949	0.111	0.003	0.64	0.06	0.22	19816	460	287	10.10	1	i
J094927-542159	T27	278.380	-0.410	0.003	0.22	0.03	0.27	12162	80	65	9.20	1*	i
J094942-540825	T28	278.265	-0.212	0.001	0.11	0.02	0.28	19605	139	42	9.33	1*	
J094942-534215	T28	277.989	0.126	0.002	0.16	0.02	0.22	20501	134	99	9.53	1	
J094942-545225	T27	278.731	-0.778	0.003	0.18	0.03	0.26	12068	149	89	9.12	1*	
J094946-555155	T27	279.367	-1.539	0.005	0.38	0.05	0.30	14154	103	73	9.57	1	
J094947-544310	T27	278.641	-0.652	0.009	1.30	0.18	0.28	11806	249	208	9.95	1*	
J095002-541659	T27	278.394	-0.291	0.002	0.08	0.01	0.26	12164	110	69	8.75	1*	
J095047-535531	T27	278.253	0.056	0.016	2.36	0.44	0.28	2197	199	161	8.74	1*	
J095048-545426	T27	278.874	-0.704	0.005	0.80	0.11	0.27	11959	534	500	9.75	1	M, W
J095049-545250	T27	278.859	-0.682	0.004	0.37	0.05	0.27	13818	169	149	9.54	1	
J095050-560333	T27	279.606	-1.595	0.007	0.45	0.15	0.27	1753	95	39	7.83	1	
J095102-543737	T28	278.723	-0.466	0.004	0.34	0.05	0.29	20210	320	290	9.84	2	
J095142-551815	T27	279.223	-0.932	0.020	1.36	0.44	0.26	1071	103	66	7.88	1	
J095108-553804	T27	279.369	-1.240	0.002	0.18	0.02	0.26	16640	206	120	9.38	2	
J095130-532200	T28	277.984	0.557	0.055	6.44	0.91	0.37	2202	152	113	9.18	1	J0951-53, H
J095155-550644	T27	279.127	-0.764	0.009	1.47	0.15	0.27	13795	343	173	10.14	1	
J095200-543745	T27	278.833	-0.380	0.003	0.15	0.02	0.25	11819	80	80	9.02	1	
J095201-534207	T28	278.254	0.344	0.003	0.47	0.07	0.31	11055	248	204	9.44	2	
J095216-544802	T27	278.970	-0.490	0.005	0.32	0.06	0.27	5611	115	68	8.69	1	
J095233-543848	T27	278.906	-0.344	0.007	0.76	0.11	0.27	5602	189	139	9.06	1	
J095240-543556	T27	278.890	-0.295	0.015	0.91	0.13	0.26	5567	92	42	9.13	1	
J095241-543331	T27	278.866	-0.263	0.004	0.30	0.05	0.26	5543	219	202	8.64	1	
J095247-562217	T27	280.013	-1.667	0.004	0.29	0.40	0.40	11860	213	177	9.30	1	
J095254-553649	T27	279.551	-1.066	0.091	8.97	0.88	0.30	5464	133	67	10.11	1	J0952-55A, w.comps (J095258, J095307), H
J095256-551112	T27	279.287	-0.730	0.018	3.06	0.43	0.28	5501	244	196	9.65	1	J0952-55B, W, Z
J095258-553452	T27	279.537	-1.035	0.012	1.73	0.25	0.29	5598	205	176	9.42	1	w.comp (J095254-553649)
J095307-553227	T27	279.530	-0.990	0.015	1.63	0.23	0.29	5561	154	103	9.39	1	w.comp (J095254-553649)

* Detected by the overlapping region of the next mosaic as well.

Table C1 continued

Name	Mosaic	l	b	S_{peak}	S_{int}	ϵ_s	rms	V_{hel}	w_{20}	w_{50}	M_{HI}	Flag	Note
J2000	TXX	deg	deg	Jy	Jy km s ⁻¹	Jy km s ⁻¹	mJy beam ⁻¹	km s ⁻¹	km s ⁻¹	km s ⁻¹	log(M_{HI}/M_{\odot})	1/2	(14)
(1)	(2)	(3)	(4)	(5)	(6)	(7)	(8)	(9)	(10)	(11)	(12)	(13)	(14)
J095317-540633	T27	278.654	-0.143	0.003	0.08	0.02	0.27	23659	341	65	9.33	2	
J095320-550947	T27	279.317	-0.676	0.003	0.33	0.05	0.25	17946	227	180	9.72	1	W
J095328-564805	T27	280.354	-1.945	0.005	0.52	0.05	0.52	21744	281	217	10.09	2	
J095341-544803	T27	279.131	-0.361	0.004	0.52	0.07	0.26	13881	219	205	9.69	1	i
J095346-542745	T27	278.929	-0.090	0.005	0.85	0.12	0.25	11844	223	168	9.77	1	
J095348-534511	T27	278.492	0.469	0.005	0.49	0.09	0.33	4716	156	98	8.73	2*	
J095351-563944	T27	280.309	-1.803	0.006	0.86	0.12	0.43	8313	209	186	9.46	1	
J095400-535542	T27	278.623	0.349	0.009	0.56	0.08	0.30	16408	114	82	9.87	1*	
J095425-561750	T27	280.143	-1.469	0.007	0.75	0.11	0.32	5451	179	130	9.03	1	
J095431-562318	T27	280.210	-1.531	0.004	0.32	0.04	0.31	11743	113	71	9.33	1	
J095443-551509	T27	279.527	-0.623	0.006	1.02	0.15	0.26	11879	394	358	9.85	1	
J095452-543623	T27	279.143	-0.104	0.007	0.31	0.06	0.26	4879	97	61	8.55	1	
J095502-561603	T27	280.191	-1.393	0.004	0.53	0.07	0.29	11626	169	121	9.54	1	w.comp (J095513-561846)
J095511-555109	T27	279.951	-1.053	0.007	0.59	0.11	0.27	3029	89	58	8.42	1	
J095513-561846	T27	280.239	-1.412	0.018	6.50	0.64	0.32	11769	487	449	10.65	1	J0955-56, w.comp (J095502-561603), W, Z
J095519-535620	T28	278.781	0.461	0.003	0.10	0.02	0.31	14036	121	100	8.97	2	
J095520-534351	T27	278.655	0.627	0.007	0.45	0.08	0.37	5655	104	57	8.84	1*	
J095540-544810	T27	279.356	-0.186	0.004	0.36	0.05	0.25	18150	133	118	9.77	1	
J095546-560020	T27	280.110	-1.123	0.022	1.13	0.37	0.27	1183	68	24	7.88	1	
J095558-560854	T27	280.219	-1.219	0.004	0.30	0.04	0.28	9181	193	147	9.09	1	
J095632-555215	T27	280.111	-0.951	0.003	0.33	0.05	0.26	16975	302	242	9.67	1	
J095647-562819	T27	280.509	-1.403	0.005	0.54	0.05	0.29	22308	181	164	10.12	1	
J095701-561819	T27	280.432	-1.252	0.002	0.11	0.02	0.27	11683	216	202	8.88	1	
J095718-564556	T27	280.746	-1.591	0.005	0.26	0.05	0.36	22021	429	379	9.80	1	w.comp?
J095733-535738	T27	279.053	0.646	0.008	0.69	0.07	0.41	18521	179	142	10.07	1	
J095734-540641	T27	279.149	0.530	0.004	0.11	0.02	0.31	19996	77	51	9.34	1	
J095738-540724	T27	279.162	0.525	0.007	1.16	0.16	0.34	4872	237	180	9.13	1	
J095756-560827	T27	280.432	-1.044	0.004	0.37	0.05	0.28	10444	308	97	9.29	1	
J095800-562201	T27	280.577	-1.217	0.002	0.15	0.02	0.28	14353	144	106	9.19	1	
J095802-555940	T27	280.352	-0.920	0.010	3.29	0.32	0.30	9212	518	443	10.13	1	
J095816-562710	T27	280.659	-1.263	0.004	0.11	0.02	0.27	21252	131	113	9.40	1	
J095825-551952	T27	279.991	-0.362	0.027	4.15	0.59	0.28	3711	194	148	9.44	1	J0958-55, W, Z
J095844-555702	T27	280.404	-0.825	0.003	0.17	0.02	0.26	16326	124	108	9.36	1	
J095849-555928	T27	280.437	-0.851	0.002	0.24	0.05	0.27	9196	211	171	9.00	1	
J095850-565818	T27	281.036	-1.627	0.013	1.24	0.23	0.47	3719	170	99	8.92	1	
J095850-542635	T27	279.498	0.380	0.003	0.30	0.04	0.27	20097	352	200	9.78	2	
J095856-564038	T27	280.869	-1.384	0.004	0.15	0.05	0.34	11660	274	200	9.01	1	
J095906-553959	T27	280.273	-0.568	0.014	2.62	0.37	0.28	4270	220	220	9.36	1	I, M, W
J095907-544852	T27	279.756	0.109	0.004	0.31	0.04	0.27	11867	155	113	9.34	1	
J095914-570929	T27	281.193	-1.742	0.004	0.18	0.03	0.48	23242	240	186	9.68	2	\$w_{20}\$ unc.
J095921-560625	T27	280.566	-0.898	0.004	0.30	0.04	0.29	16359	227	169	9.59	1	
J095927-550949	T27	280.007	-0.138	0.008	1.02	0.14	0.26	5403	164	133	9.16	1	
J095934-555434	T27	280.471	-0.722	0.004	0.44	0.06	0.28	10299	124	108	9.36	1	
J095944-565252	T27	281.079	-1.480	0.018	1.63	0.44	0.46	8596	188	99	9.76	2	cont. nearby
J100041-555943	T27	280.649	-0.695	0.013	1.32	0.25	0.29	2463	123	106	8.59	1	
J100048-554827	T27	280.548	-0.536	0.002	0.26	0.04	0.26	14142	275	275	9.41	1	
J100051-560501	T27	280.720	-0.752	0.003	0.34	0.05	0.30	9857	157	79	9.21	2	
J100054-545924	T27	280.066	0.125	0.015	0.86	0.12	0.27	13797	95	39	9.91	1	
J100058-535753	T27	279.456	0.949	0.011	1.37	0.14	0.55	19883	380	258	10.43	1	
J100113-544302	T27	279.937	0.370	0.008	1.18	0.22	0.33	3698	267	213	8.89	1	
J100113-540934	T27	279.603	0.816	0.007	0.45	0.08	0.46	5797	122	106	8.87	1	
J100124-542756	T27	279.809	0.588	0.010	0.65	0.12	0.37	3007	105	63	8.45	1	
J100128-560759	T27	280.819	-0.739	0.005	0.32	0.06	0.29	4820	113	71	8.56	1	
J100154-560146	T27	280.804	-0.621	0.009	1.55	0.15	0.31	11703	373	315	10.02	1	
J100200-565847	T27	281.386	-1.372	0.009	1.01	0.20	0.40	11604	303	264	9.82	1	
J100210-544426	T27	280.062	0.434	0.013	0.87	0.16	0.34	3704	92	49	8.76	1	
J100214-573213	T26	281.745	-1.799	0.005	0.36	0.05	0.60	22323	358	238	9.95	2	
J100233-563659	T26	281.227	-1.037	0.008	0.72	0.10	0.35	9129	120	76	9.47	1*	
J100238-572656	T26	281.734	-1.697	0.110	16.23	2.30	0.62	2607	276	213	9.73	1*	J1002-57
J100246-550814	T27	280.368	0.167	0.009	0.84	0.12	0.29	11835	189	130	9.76	1	
J100247-543322	T27	280.022	0.635	0.008	1.25	0.12	0.41	14095	232	93	10.08	1	
J100300-572031	T26	281.712	-1.581	0.006	0.80	0.11	0.49	11587	178	157	9.72	1*	w.comp (J100310-571755)
J100303-552755	T27	280.597	-0.071	0.012	0.82	0.12	0.29	9044	108	71	9.51	1	
J100309-553414	T27	280.670	-0.148	0.005	0.70	0.10	0.28	10200	178	178	9.55	1	
J100310-571755	T26	281.703	-1.533	0.012	4.56	0.45	0.55	11542	432	303	10.47	1*	BL, w.comps (J100300-572031)
J100311-562939	T26	281.224	-0.887	0.058	4.00	0.75	0.31	1211	69	51	8.45	1*	J1003-56
J100406-555315	T27	280.966	-0.323	0.004	0.51	0.10	0.29	4776	163	130	8.75	1	
J100414-570922	T27	281.734	-1.333	0.003	0.13	0.02	0.42	14534	131	94	9.13	2	
J100423-563012	T26	281.363	-0.796	0.011	0.82	0.12	0.35	9192	103	62	9.53	1*	
J100428-553440	T27	280.824	-0.043	0.007	0.51	0.09	0.28	5810	146	93	8.92	1	
J100431-560922	T27	281.173	-0.504	0.006	1.29	0.18	0.33	4781	221	221	9.16	1	
J100437-565616	T27	281.646	-1.126	0.007	0.59	0.08	0.38	8641	272	216	9.33	1	
J100441-570213	T27	281.714	-1.200	0.004	0.11	0.04	0.39	23902	367	295	9.52	2	
J100450-561917	T26	281.305	-0.612	0.004	0.38	0.05	0.33	21426	118	80	9.94	2*	\$w_{20}\$ unc.
J100454-545308	T27	280.465	0.552	0.005	0.27	0.10	0.35	10428	328	176	9.16	1	
J100456-563115	T26	281.435	-0.765	0.007	1.65	0.16	0.40	11662	487	456	10.04	1*	NaN
J100458-554308	T27	280.964	-0.115	0.004	0.18	0.03	0.28	10121	126	93	8.94	1	
J100529-562752	T26	281.463	-0.674	0.006	0.40	0.06	0.37	21669	312	90	9.97	1*	

* Detected by the overlapping region of the next mosaic as well.

Table C1 continued

Name	Mosaic	l	b	S_{peak}	S_{int}	ε_s	rms	V_{hel}	w_{20}	w_{50}	M_{HI}	Flag	Note
J2000	TXX	deg	deg	Jy	Jy km s ⁻¹	Jy km s ⁻¹	mJy beam ⁻¹	km s ⁻¹	km s ⁻¹	km s ⁻¹	log(M_{HI}/M_{\odot})	1/2	(14)
(1)	(2)	(3)	(4)	(5)	(6)	(7)	(8)	(9)	(10)	(11)	(12)	(13)	(14)
J100544-564423	T26	281.653	-0.876	0.012	0.91	0.09	0.40	16497	127	90	10.09	1*	
J100604-545333	T27	280.605	0.646	0.005	0.25	0.04	0.37	21538	179	145	9.76	2	
J100628-545420	T27	280.658	0.668	0.004	0.15	0.05	0.37	21443	269	225	9.55	2	
J100633-574608	T26	282.347	-1.644	0.014	1.41	0.20	0.61	11519	262	238	9.96	1	
J100655-555346	T27	281.291	-0.096	0.017	0.90	0.09	0.29	21394	71	25	10.31	2*	
J100713-562115	T26	281.592	-0.444	0.004	0.21	0.03	0.34	14956	122	107	9.37	1*	
J100720-551405	T27	280.952	0.474	0.015	0.81	0.11	0.34	10116	95	36	9.61	1	w.comp (J100730-551027)
J100721-564409	T26	281.831	-0.742	0.009	1.61	0.16	0.42	11975	270	254	10.05	1	
J100723-551136	T27	280.934	0.512	0.005	0.26	0.04	0.34	12777	372	273	9.32	2	
J100725-562753	T27	281.679	-0.518	0.007	0.41	0.06	0.37	8805	388	277	9.19	2	w.comp
J100725-562755	T26	281.679	-0.518	0.006	0.20	0.04	0.36	8818	114	66	8.89	1	
J100730-551027	T27	280.935	0.537	0.014	2.62	0.26	0.39	10094	325	166	10.12	1	i, w.comp (J100720-551405)
J100736-545522	T27	280.801	0.750	0.022	3.66	0.36	0.53	9044	331	258	10.17	1	M, W
J100804-555400	T26	281.424	-0.006	0.005	0.32	0.04	0.29	20174	232	189	9.81	1*	NaN
J100829-553535	T27	281.293	0.278	0.001	0.04	0.02	0.28	20853	315	272	8.97	2	
J100829-554522	T26	281.387	0.145	0.016	1.23	0.23	0.29	2672	143	86	8.63	1*	
J100829-575415	T26	282.636	-1.604	0.007	0.77	0.11	0.68	10285	210	186	9.60	1	
J100905-560355	T26	281.635	-0.059	0.006	0.37	0.07	0.32	3108	78	72	8.23	1*	
J100905-563726	T26	281.958	-0.514	0.082	12.27	1.74	0.41	2641	220	160	9.62	1	J1009-56, H
J100923-544845	T27	280.946	0.989	0.009	0.40	0.40	0.88	4454	275	222	8.58	1	
J100924-563231	T26	281.948	-0.421	0.042	5.40	0.77	0.38	2732	127	120	9.29	1	
J100932-563718	T26	282.008	-0.476	0.005	0.22	0.03	0.35	15105	129	106	9.40	1	
J100937-562248	T26	281.878	-0.272	0.005	0.52	0.06	0.32	8145	370	343	9.23	1	w.comp
J101025-553850	T26	281.547	0.391	0.004	0.37	0.05	0.28	14286	266	218	9.57	1*	i? with a hole in the centre?
J101033-574438	T26	282.768	-1.313	0.018	1.76	0.33	0.54	2607	148	100	8.76	1	w.comp
J101056-552048	T27	281.435	0.680	0.002	0.07	0.01	0.31	18483	133	133	9.09	2	
J101100-552019	T26	281.437	0.691	0.006	0.33	0.05	0.33	10143	79	47	9.22	1*	
J101131-561931	T26	282.061	-0.076	0.004	0.16	0.03	0.29	7866	129	102	8.68	1	
J101131-561056	T26	281.980	0.041	0.007	1.51	0.21	0.31	9049	359	338	9.78	1	
J101208-551909	T26	281.558	0.799	0.016	1.28	0.24	0.38	2648	120	51	8.64	1*	
J101209-560712	T26	282.017	0.143	0.004	0.39	0.06	0.30	11847	226	200	9.43	1	
J101211-552311	T27	281.602	0.748	0.003	0.05	0.03	0.36	16314	424	237	8.83	2	
J101211-564237	T26	282.357	-0.339	0.011	0.50	0.07	0.34	16373	69	32	9.82	1	
J101242-573947	T26	282.957	-1.083	0.008	1.07	0.11	0.42	24072	185	179	10.49	1	
J101258-571946	T26	282.797	-0.788	0.008	1.02	0.14	0.45	11587	284	214	9.83	1	
J101301-561450	T26	282.188	0.107	0.004	0.17	0.02	0.29	16413	223	207	9.36	1	
J101317-565425	T26	282.594	-0.415	0.007	0.49	0.09	0.36	3128	120	87	8.37	1	
J101327-552239	T26	281.747	0.859	0.007	0.46	0.07	0.49	14239	169	96	9.66	1	
J101403-561711	T26	282.329	0.156	0.006	0.53	0.10	0.29	3138	108	67	8.40	1	
J101408-560003	T26	282.177	0.398	0.004	0.29	0.04	0.29	11860	130	63	9.31	1	
J101446-574032	T26	283.192	-0.937	0.007	1.33	0.19	0.50	7081	250	190	9.51	1	
J101551-555254	T26	282.309	0.631	0.004	0.30	0.04	0.31	11797	129	49	9.32	2	
J101553-583655	T26	283.841	-1.633	0.010	0.42	0.06	0.55	14242	125	67	9.62	2	
J101611-571957	T26	283.158	-0.546	0.029	1.47	0.27	0.45	2672	85	36	8.70	1	i
J101654-590156	T25	284.183	-1.905	0.003	0.23	0.03	0.64	22528	565	484	9.77	2*	
J101745-561805	T26	282.764	0.430	0.020	4.14	0.41	0.33	7544	269	253	10.06	1	
J101804-561022	T26	282.728	0.561	0.009	0.55	0.08	0.33	7316	73	54	9.15	1	
J101836-563331	T26	283.004	0.281	0.002	0.09	0.02	0.29	14575	123	107	8.96	2	
J101935-570636	T26	283.418	-0.107	0.019	2.93	0.54	0.50	2656	166	148	9.00	1	
J101939-560134	T26	282.833	0.806	0.013	1.51	0.21	0.55	8939	269	242	9.77	1	
J101949-562439	T26	283.062	0.496	0.004	0.16	0.03	0.34	7504	76	56	8.63	1	
J101958-570507	T26	283.448	-0.058	0.011	0.87	0.12	0.54	11865	123	65	9.78	1	
J102101-582352	T25	284.281	-1.081	0.003	0.09	0.01	0.47	22143	224	209	9.35	2	
J102142-563705	T26	283.394	0.464	0.025	2.50	0.47	0.38	2672	151	97	8.94	1	
J102201-585725	T25	284.694	-1.481	0.005	0.23	0.03	0.38	14561	112	77	9.39	1*	
J102240-563220	T26	283.462	0.602	0.005	0.34	0.05	0.37	11496	172	156	9.34	1	
J102244-591200	T25	284.901	-1.637	0.011	1.06	0.15	0.51	10794	130	130	9.78	1	
J102252-575753	T25	284.251	-0.586	0.012	0.64	0.09	0.62	14350	111	80	9.81	1*	
J102449-575624	T25	284.458	-0.426	0.014	0.77	0.11	0.64	7325	77	57	9.31	1*	
J102500-591447	T25	285.171	-1.521	0.006	0.59	0.08	0.39	11605	130	130	9.59	1	
J102505-592708	T25	285.290	-1.690	0.010	0.64	0.09	0.46	11578	119	103	9.63	1	w.comp
J102518-570330	T26	284.044	0.355	0.015	1.00	0.14	0.63	7267	134	64	9.41	1	
J102534-562759	T26	283.763	0.877	0.006	0.47	0.07	0.68	11685	208	182	9.50	1	
J102719-594756	T25	285.713	-1.835	0.010	0.68	0.10	0.65	6115	268	253	9.09	1	
J102724-585810	T25	285.288	-1.123	0.006	1.28	0.18	0.39	6164	261	246	9.37	1	
J102733-593751	T25	285.650	-1.677	0.003	0.15	0.02	0.46	22736	323	282	9.58	2	
J102946-594348	T25	285.940	-1.616	0.015	1.76	0.25	0.62	5725	201	134	9.45	1	i?
J102959-584555	T25	285.467	-0.775	0.005	0.18	0.02	0.42	11434	80	80	9.05	1	
J103054-582318	T25	285.376	-0.390	0.004	0.26	0.02	0.40	14917	413	236	9.46	1	
J103118-593619	T25	286.043	-1.410	0.004	0.23	0.03	0.54	11496	272	272	9.17	1	
J103218-574611	T25	285.220	0.236	0.005	0.24	0.03	0.40	11264	130	125	9.17	1	
J103243-592040	T25	286.065	-1.094	0.005	0.61	0.09	0.45	16758	341	276	9.93	1	i?
J103418-584521	T25	285.944	-0.483	0.014	2.02	0.29	0.42	5762	175	174	9.51	1	
J103552-584106	T25	286.086	-0.319	0.013	0.75	0.11	0.41	5436	93	51	9.03	1	
J103607-580202	T25	285.790	0.261	0.039	2.14	0.30	0.38	5751	86	35	9.54	1	J1036-58
J103659-591113	T25	286.458	-0.685	0.061	15.24	2.07	0.54	3257	333	297	9.89	1	J1036-59, M, Z
J103723-595048	T25	286.826	-1.235	0.015	1.35	0.25	0.56	3276	136	87	8.85	1	
J103801-582850	T25	286.228	-0.004	0.005	0.22	0.03	0.41	15194	132	115	9.41	1	

* Detected by the overlapping region of the next mosaic as well.

Table C1 continued

Name	Mosaic	l	b	S_{peak}	S_{int}	ε_S	rms	V_{hel}	w_{20}	w_{50}	M_{HI}	Flag	Note
J2000	TXX	deg	deg	Jy	Jy km s^{-1}	Jy km s^{-1}	mJy beam^{-1}	km s^{-1}	km s^{-1}	km s^{-1}	$\log(M_{\text{HI}}/M_{\odot})$	1/2	(14)
(1)	(2)	(3)	(4)	(5)	(6)	(7)	(8)	(9)	(10)	(11)	(12)	(13)	(14)
J103809-573204	T25	285.780	0.830	0.013	0.61	0.09	0.62	5968	156	34	9.03	2	
J103844-584312	T25	286.426	-0.167	0.007	0.77	0.11	0.42	14684	369	333	9.91	1	i
J103903-573926	T25	285.945	0.781	0.010	0.49	0.09	0.58	5350	263	248	8.84	2	
J104007-601914	T24	287.356	-1.482	0.013	1.36	0.19	0.58	5690	165	151	9.33	1*	
J104010-583801	T25	286.547	-0.002	0.034	2.43	0.45	0.40	1301	92	37	8.30	1	
J104104-592140	T25	286.998	-0.584	0.011	1.47	0.21	0.70	9084	393	322	9.77	1	w.comp
J104104-582725	T25	286.566	0.210	0.003	0.07	0.01	0.36	15572	311	177	8.92	2	
J104133-583131	T25	286.653	0.180	0.013	1.01	0.14	0.44	5668	111	83	9.20	1	i
J104143-593109	T24	287.147	-0.683	0.007	0.54	0.10	0.79	3261	117	87	8.44	1*	
J104253-585109	T25	286.961	-0.025	0.007	0.83	0.12	0.49	15322	276	165	9.98	1	
J104447-611148	T24	288.273	-1.983	0.007	0.37	0.05	0.76	9531	187	76	9.21	2	
J104505-610513	T24	288.255	-1.868	0.011	1.48	0.21	0.61	4380	209	180	9.14	1	
J104549-575442	T25	286.861	0.986	0.010	0.27	0.05	0.94	6628	78	78	8.76	2	
J104729-591531	T24	287.673	-0.110	0.008	0.92	0.13	0.59	6765	141	67	9.31	1	
J104820-583730	T24	287.482	0.504	0.005	0.93	0.13	0.37	14052	225	208	9.96	1*	
J104821-605352	T24	288.519	-1.518	0.017	1.90	0.27	0.41	4461	144	110	9.26	1	
J104842-590858	T24	287.762	0.058	0.020	3.72	0.37	0.57	11594	330	285	10.39	1	
J104905-611626	T24	288.769	-1.813	0.007	0.10	0.02	0.66	6450	78	78	8.30	2	
J104915-604343	T24	288.539	-1.318	0.011	0.66	0.09	0.41	13694	104	56	9.78	1	
J104923-583835	T24	287.612	0.550	0.004	0.17	0.02	0.37	16570	76	56	9.36	1*	
J105040-590738	T24	287.977	0.192	0.010	2.11	0.21	0.49	13920	321	305	10.30	1	
J105100-603433	T24	288.663	-1.085	0.004	0.60	0.09	0.36	11505	196	148	9.59	1	
J105202-601726	T24	288.651	-0.772	0.003	0.13	0.02	0.38	5648	116	80	8.31	1	
J105211-603832	T24	288.823	-1.079	0.004	0.11	0.02	0.32	11237	130	112	8.83	1	
J105230-605431	T24	288.974	-1.302	0.003	0.16	0.02	0.33	13779	131	131	9.17	1	
J105251-604027	T24	288.909	-1.072	0.003	0.14	0.03	0.29	5512	301	91	8.31	1	
J105328-591538	T24	288.358	0.232	0.007	0.54	0.08	0.36	11569	174	158	9.55	1	
J105333-602739	T24	288.893	-0.843	0.002	0.16	0.02	0.32	14492	178	156	9.23	2	
J105342-594417	T24	288.594	-0.185	0.007	0.90	0.09	0.37	21776	409	382	10.33	1	
J105349-603457	T24	288.976	-0.938	0.013	0.91	0.13	0.31	5515	68	51	9.13	1	
J105401-601037	T24	288.821	-0.562	0.004	1.15	0.11	0.37	19334	500	386	10.33	2	
J105408-604654	T24	289.097	-1.100	0.004	1.20	0.17	0.31	9136	560	521	9.69	2	
J105506-584313	T24	288.313	0.810	0.005	0.68	0.10	0.37	15429	213	182	9.90	1	
J105543-591510	T24	288.614	0.364	0.006	0.79	0.11	0.29	11505	178	157	9.71	1	
J105601-590956	T24	288.612	0.459	0.003	0.16	0.02	0.27	11562	130	103	9.02	1	
J105629-590449	T24	288.629	0.562	0.004	0.18	0.03	0.31	5705	78	65	8.45	2	
J105809-613714	T24	289.896	-1.650	0.003	0.25	0.06	0.41	21484	202	170	9.76	2	BL
J105823-595219	T24	289.182	-0.053	0.018	3.24	0.46	0.31	3410	253	234	9.26	1	
J105827-595011	T24	289.175	-0.017	0.005	0.59	0.06	0.28	20648	230	178	10.10	1	
J105827-610353	T24	289.694	-1.131	0.002	0.14	0.02	0.43	15961	294	243	9.24	2	
J105853-602745	T24	289.487	-0.562	0.004	0.64	0.06	0.31	21463	473	444	10.17	1	
J105913-603021	T24	289.543	-0.584	0.004	0.24	0.04	0.33	6695	128	114	8.72	1	
J105928-610452	T24	289.811	-1.094	0.028	4.89	0.69	0.44	5808	236	172	9.90	1	
J105940-593005	T24	289.174	0.351	0.003	0.26	0.04	0.27	11487	282	186	9.23	2	
J110000-593619	T24	289.256	0.274	0.008	0.82	0.12	0.27	11523	248	183	9.73	1	Faint double horn? i?
J110022-604242	T24	289.757	-0.713	0.005	0.19	0.02	0.35	5442	95	46	8.44	1	
J110035-610058	T24	289.907	-0.979	0.024	5.31	0.75	0.38	3572	302	288	9.52	1	
J110057-603559	T24	289.777	-0.581	0.003	0.17	0.02	0.31	24136	332	118	9.69	1	
J110113-601148	T24	289.639	-0.201	0.004	0.34	0.06	0.31	4467	181	94	8.51	1	
J110204-594121	T24	289.528	0.306	0.002	0.12	0.02	0.27	5540	174	124	8.24	2	
J110223-620954	T24	290.576	-1.938	0.005	0.20	0.22	0.62	20903	483	397	9.63	2	
J110239-603157	T24	289.938	-0.435	0.007	0.63	0.09	0.39	11450	129	107	9.61	1	
J110302-613311	T24	290.397	-1.348	0.011	1.01	0.19	0.33	4509	143	111	9.00	1	
J110325-595036	T24	289.747	0.234	0.003	0.23	0.03	0.28	21664	363	326	9.73	1	
J110359-594426	T24	289.771	0.357	0.007	0.43	0.08	0.30	3516	82	24	8.41	2	
J110419-603412	T24	290.141	-0.386	0.008	0.66	0.09	0.40	7480	176	169	9.26	1	
J110459-605022	T24	290.324	-0.600	0.015	1.58	0.22	0.42	5440	159	125	9.36	1	
J110506-594013	T24	289.871	0.478	0.011	1.56	0.22	0.34	11530	267	249	10.01	1	
J110516-611219	T24	290.502	-0.922	0.004	0.28	0.05	0.41	5784	128	128	8.65	1	
J110700-593047	T24	290.030	0.717	0.012	0.75	0.11	0.42	6708	66	46	9.21	1	
J110730-604836	T24	290.595	-0.452	0.017	1.57	0.22	0.44	5482	193	158	9.36	1	
J110734-594045	T24	290.162	0.592	0.004	0.21	0.04	0.34	9062	128	77	8.93	1	
J110827-601412	T24	290.480	0.121	0.006	0.67	0.09	0.41	5677	165	126	9.02	1	

This paper has been typeset from a $\text{\TeX}/\text{\LaTeX}$ file prepared by the author.